**Università degli Studi di Genova**

DIPARTIMENTO DI FISICA
SCUOLA DI DOTTORATO DI RICERCA IN FISICA

# SQUEEZED LIGHT FOR ADVANCED GRAVITATIONAL WAVE INTERFEROMETER

Supervisors:
**Dr. F. Sorrentino**
**Dr. M. Canepa**

**Candidate**:
**Barbara Garaventa**

**April 2023**

*"Remember to look up at the stars and not down at your feet. Try to make sense of what you see and wonder about what makes the universe exist. Be curious. And however difficult life may seem, there is always something you can do and succeed at. It matters that you don't just give up."*

*S. Hawking*

**Abstract**

The sensitivity of gravitational wave interferometric detectors is ultimately limited by the quantum noise, which arises from the quantum nature of light and it is driven by vacuum fluctuations of the optical field entering from the dark port of the interferometer. Quantum optics methods, in particular the injection of squeezed states of light in the interferometer, are applied to reduce quantum noise.
Vacuum fluctuations determine two complementary effects: the shot-noise and the radiation-pressure noise. The former depends on phase fluctuations of the optical field and dominates at high frequencies. The latter depends on amplitude fluctuation of the optical field and dominates at low frequencies.
Injecting Frequency-Independent Squeezed vacuum (FIS) into the dark port, a reduction of phase fluctuations is achieved, but at the same time, due to the Heisenberg's uncertainty principle, the amplitude fluctuations are larger, therefore we need to produce Frequency-Dependent Squeezing (FDS) in order to achieve a broadband mitigation of quantum noise.
During the last observing run (O3), FIS up to 3.2 dB was injected into the interferometer, improving the sensitivity curve at high frequencies. For the next observing run (O4), it is necessary to mitigate quantum noise in the entire sensitive bandwidth. The simplest method to produce FDS, which was installed for the ongoing upgrades in Virgo and LIGO detectors, is to reflect the frequency-independent squeezed vacuum though an optical filter cavity.
Another technique to achieve quantum noise reduction over the entire sensitivity band exploits the Einstein-Podolsky-Rosen (EPR) entanglement. With this technique two entangled beams, at different frequencies, would be injected into the dark port of the interferometer, which would then be used both as a filter cavity and as a GW detector.
I contributed to both FDS experiment for Advanced Virgo Plus and an EPR experiment for possible application in future gravitational wave detectors.

**Keywords**: gravitational wave, interferometer, squeezing, quantum noise, optics, quantum optics, astrophysics

# Contents

# Chapter 1

# Introduction

Gravitational waves (GW) are ripples in spacetime due to violent astrophysics events and predicted in 1916 by Albert Einstein with the theory of General Relativity. Gravitation becomes a spacetime property and the relation between it and the masses can be summarized by these famous words from John Wheeler: "Spacetime tells matter how to move; matter tells spacetime how to curve."
The first direct observation was in September 2015 (GW150914 [1]) from the merger of two black holes and confirmed in 2016 by LIGO and Virgo gravitational wave interferometers. This event ushered in the era of GW astronomy providing a new messenger for astrophysics.
An important event that marked the beginning of the era of multi-messenger astronomy was GW170817, a gravitatinal wave caused by the merger of two neutron stars [2]. This signal was detected by the LIGO and Virgo detectors network, in quasi-coincidence with a gamma-ray burst, detected by the Fermi and Integral satellites [3].
Laser interferometry is necessary to detect the very small perturbations ($\Delta$L $\sim 10^{-18}$ m) given by the passage of a gravitational wave on the optical path of the light that is moving back and forth between test masses. In fact, the GW detectors are Michelson interferometers with Fabry-Perot cavity in each arm to artificially increase the length of the arms in order to detect a tiny displacement.
The current GW detectors network is composed by the two LIGO detectors (Handford and Livingston) in the USA, Virgo in Italy and KAGRA in Japan. In order to improve the sensitivity of the GW detectors, many sources of noise need to be mitigated and several technological improvements and challenges have been made over the years. In particular, during the last observation run O3, squeezing injection techniques were introduced to mitigate the quantum noise at high frequencies, increasing the number of detections [4] [5]. Thanks to it too, other two important events were detected in January 2020, the first signals from the merger of a black hole and a neutron

star (GW200105 and GW200115), by the LIGO, Virgo and KAGRA detectors [6]. For the next observation run (O4), one important improvement will be the frequency-dependent squeezing injection into the interferometer, in order to reduce quantum noise also at low frequencies.
This PhD thesis will focuses on the activities for quantum noise mitigation, which is a fundamental limitation of GW detectors, by injecting squeezed states of light into the GW interferometers, in particular frequency-dependent squeezing (FDS) techniques. My work is done both at the quantum optics laboratory in the Physics Department of Genoa, at the gravitational waves detector Virgo (Advanced Virgo Plus for O4 run), located in Cascina (Pi) and at the R&D 1500 W laboratory at EGO-Virgo site. The structure of the thesis is as follows, in particular I mainly dedicated on the sperimental activities (from chapter 4 to 8) and on their results (chapter 9):

**Chapter 2** will focus on the theoretical background, in particular with a quick explanation of the theory of gravitational wave and the detection, the main noises that limit the sensitivity curve, more in detail quantum noise.

**Chapter 3** will describe the frequency-dependent-squeezing experiments, in particular filter cavity technique in Advanced Virgo Plus and EPR technique for next generation GW interferometers.

**Chapter 4** will focus on the low-losses Faraday isolators, which were developed, tested and installed for Advanced Virgo Plus squeezing system.

**Chapter 5** will describe the acousto-optical-modulator test performed at Genoa laboratory and installed for Advanced Virgo Plus squeezing system.

**Chapter 6** will explain the coherent control loop development for squeezing measurement in Advanced Virgo Plus system.

**Chapter 7** will describe a technique to automatically align using dither lines, performed in Advanced Virgo Plus squeezing system.

**Chapter 8** will focus on the EPR activities, in particular on optical cavity tests necessary for this FDS technique. The activities explains were performed both at Genoa laboratory and at R&D laboratory at EGO-Virgo site.

**Chapter 9** finally, the important results achieved also thanks to the activities described in chapters 4,5,6,7 will be shown.

# Chapter 2

# Gravitational Waves: Theory and Detection

In 1916, Albert Enstein predicted gravitational waves (GWs) with his theory of *General Relativity*, defining the relation between spacetime geometry and gravitational energy, as follows [7]:

$$G_{\mu\nu} \equiv R_{\mu\nu} - \frac{1}{2} g_{\mu\nu} R = \frac{8\pi G}{c^4} T_{\mu\nu} \tag{2.1}$$

where $G_{\mu\nu}$, $R_{\mu\nu}$, R, $g_{\mu\nu}$ and $T_{\mu\nu}$ are, respectively, the Einstein tensor, the Ricci tensor, the Ricci scalar, the metric tensor and the energy-momentum tensor.
Gravitational waves propagate at the speed of light, have two states of polarization and interact with matter allowing us to reveal them directly using special Michelson interferometers.

## 2.1 Linearized General Relativity

From the theory of General Relativity, GWs emerge by linearizing the metric around the Minkowski flat space-time metric $\eta_{\mu\nu}$ (perturbative approach), as follows:

$$g_{\mu\nu} = \eta_{\mu\nu} + h_{\mu\nu} \qquad |h_{\mu\nu}| \ll 1 \tag{2.2}$$

where $h_{\mu\nu}$ is a small perturbation of the metric tensor and it is a symmetric tensor. The Riemann tensor is defined by:

$$R_{\mu\nu\rho\delta} = \frac{1}{2}(\partial_\nu \partial_\rho h_{\mu\delta} - \partial_\nu \partial_\delta h_{\mu\rho} - \partial_\nu \partial_\rho h_{\mu\delta} - \partial_\mu \partial_\rho h_{\nu\delta} + \partial_\mu \partial_\delta h_{\nu\rho}) \tag{2.3}$$

which is invariant under slowly varying diffeomorphism and we can define, respectively, the Ricci tensor, the Ricci scalar and the Einstein tensor as

follows

$$R_{\mu\nu} = -\frac{1}{2}(\Box h_{\mu\nu} - \partial_\mu\partial_\nu h - \partial_\mu\partial_\alpha h^\alpha_\nu - \partial_\nu\partial_\alpha h^\alpha_\mu) \tag{2.4}$$

$$R = -\Box h + \partial_\mu\partial_\nu h^{\mu\nu} \tag{2.5}$$

$$G_{\mu\nu} = -\frac{1}{2}(\Box\bar{h}_{\mu\nu} - \partial_\mu\partial^\alpha\bar{h}_{\alpha\nu} - \partial_\nu\partial^\alpha\bar{h}_{\alpha\mu} + \eta_{\mu\nu}\partial^\alpha\partial^\beta\bar{h}_{\alpha\beta}). \tag{2.6}$$

So, by solving eq.(2.1) it is possible to demostrate that we can obtain the gravitational wave equation, as follows:

$$\Box\bar{h}_{\mu\nu} = -\frac{16\pi G}{c^4}T_{\mu\nu}, \tag{2.7}$$

which describes the propagation of the metric perturbation that travel at the speed of light. In vacuum, i.e. imposing $T_{\mu\nu} = 0$, we obtain:

$$\Box\bar{h}_{\mu\nu} = 0, \tag{2.8}$$

where $\Box = \nabla^2 - \frac{\partial_t^2}{c^2}$ is the flat space d'Alembertian and $\bar{h}_{\mu\nu}$ is the tensor defined as:

$$\bar{h}_{\mu\nu} \equiv h_{\mu\nu} - \frac{1}{2}\eta_{\mu\nu}h. \tag{2.9}$$

We studied the solutions of the vacuum field equations since we are interested in the propagation of GWs and in their interaction with a detector. Moreover, we can simplify eq. (2.3) with four more conditions which reduce the number of independent components of $\bar{h}_{\mu\nu}$, from six to two, imposing the Lorentz Gauge and the TT (Tranverse and Traceless) frame as follows:

$$\partial^\nu\bar{h}_{\mu\nu} = 0 \tag{2.10}$$

$$h^{0\mu} = 0 \qquad h^\sigma_\sigma = 0. \tag{2.11}$$

Since from the conditions in (2.11) the trace $\bar{h} = 0$, we have $\bar{h}_{\mu\nu}$=$h_{\mu\nu}$. So, the symmetric tensor $h_{\mu\nu}$ has only two independent degrees of freedom which correspond to the amplitude of the so-called plus $h_+$ and cross $h_\times$ polarizations of the wave. Indeed, we can write the gravitational waves, which are the solutions of the eq. (2.1), with the conditions of symmetric and traceless along the z-direction, as follows:

$$h^{TT}_{\mu\nu}(t,z) = \begin{pmatrix} 0 & 0 & 0 & 0 \\ 0 & h_+ & h_\times & 0 \\ 0 & h_\times & -h_+ & 0 \\ 0 & 0 & 0 & 0 \end{pmatrix} cos(2\pi f(t - \frac{z}{c})). \tag{2.12}$$

So, combining the (2.2) and (2.7), we obtain the metric in the TT frame, which is the response of a detector to the GW, negleting terms $\mathcal{O}(h^2)$:

$$g_{\mu\nu}^{TT} = \eta_{\mu\nu}^{TT} + h_{\mu\nu}^{TT} = \begin{pmatrix} -1 & 0 & 0 & 0 \\ 0 & 1+h_+(t,z) & h_\times(t,z) & 0 \\ 0 & h_\times(t,z) & 1-h_+(t,z) & 0 \\ 0 & 0 & 0 & 1 \end{pmatrix} \tag{2.13}$$

with the interval $ds^2 = g_{\mu\nu}^{TT} dx^\mu dx^\nu$.
Therefore, in the approximation of the linearized theory, the sources of gravitational waves are considered to move in space-time along trajectories, due to their mutual influence. For example, if we consider a binary system as the background space-time metric, it means that we are describing its dynamics using Newtonian gravity, rather than General Relativity.

### 2.1.1 Gravitational waves interaction with matter

In this section, the gravitational waves interaction with a detector, as a set of test masses, will be described.
First of all, since the GWs in TT gauge have a simple form, we have to understand which reference frame corresponds to the TT gauge, writing the *geodesic equation* in the frame of interest.
In General Relativity, the geodesic equation of a test mass in the curved background described by the metric $g_{\mu\nu}$ is given by

$$\frac{d^2x^\mu}{d\tau^2} + \Gamma^\mu_{\nu\rho}(x)\frac{dx^\nu}{d\tau}\frac{dx^\rho}{d\tau} = 0 \tag{2.14}$$

for a curve $x^\mu(\tau)$ in some reference frame, parametrized by the proper time $\tau$, with $\Gamma^\mu_{\nu\rho} = \frac{1}{2}(\partial_\nu h^\mu_\rho + \partial_\rho h^\mu_\nu - \partial^\mu h_{\nu\rho})$ the Christoffel symbol to linear order in $h_{\mu\nu}$.
If we expand the geodesic equation at time $\tau = 0$ and to first order in $h_{\mu\nu}$ according to the TT gauge conditions, we can say that the particles which were at rest before the arrival of the wave, remain at rest even after the arrival of the wave and their coordinate distance must remain constant. Thus, in General Relativity, physical effects can be seen not on the coordinates but by looking invariant quantities, i.e. proper distance and proper time.
Let us consider, for instance, the spatial separation L between two events; so, the proper distance to linear order will be given by:

$$s \simeq L + \frac{1}{2}h_{ij}\frac{L_i L_j}{L} \tag{2.15}$$

with $s = s_i\frac{Li}{L}$. So, we can write the geodesic equation in terms of proper distance as follows:

$$\ddot{s} \simeq \frac{1}{2}\ddot{h_{ij}}s_j \tag{2.16}$$

where we assume that to lowest order in h, we have $L_j = s_j$.
Considering the test masses as two mirrors between which light travels back and forth, the proper distance indicates the time in which light make a round trip. Although the GW has a very simple form in the TT gauge, it is not the one used because by choosing an origin, the coordinates are defined with a rigid ruler and the passage of a GW determines the displacement of the test masses, which does not occur in the TT gauge, since by definition the positions of the test masses are unchanged upon passage of a GW.
So, we have to define the so-called *proper detector frame*. Indeed, for an Earth-based detector, we have to write the metric with coordinates transformation from the free falling frame to the rotating and accelerating frame, as follows:

$$ds^2 \simeq -c^2dt^2[1 + \frac{2}{c^2}a \cdot x + \frac{1}{c^4}(a \cdot x)^2 - \frac{1}{c^2}(\Omega \times x)^2 + R_{0i0j}x^i x^j] \quad (2.17)$$

$$+ 2cdtdx^i[\frac{1}{c}\epsilon_{ijk}\Omega^j x^k - \frac{2}{3}R_{0jik}x^j x^k] \quad (2.18)$$

$$+ dx^i dx^j[\delta_{ij} - \frac{1}{3}R_{ijkl}x^k x^l] \quad (2.19)$$

with angular velocity $\Omega$ and where the terms proportional to the Riemann tensor containing both the effects of slowly varying gravitational background and of GWs. So, if we consider r$\sim |x^i|$ and $L_B$ the variation metric scale, we can conclude that:

- at zero order in $r/L_B$, the metric reduces to the flat metric ($g_{\mu\nu} = \eta_{\mu\nu}$);
- at first order in $r/L_B$, the corrections can be described in terms of Newtonian forces;
- at quadratic order in $r/L_B$, the terms proportional to the Riemann tensor appear, therefore the effect of the GWs is entirely in the term $\mathcal{O}(r^2)$.

Note that, comparing to the typical variation time scales of all other effects, GWs can have high frequencies, therefore we shall focus on the response of a detector in the high frequency window (from 10 Hz) and in particular on the Degree of Freedom (DoF) sensitive to the GWs. We can derive the geodesic equation in the TT frame, assuming that only the GWs contribute to the Riemann tensor, and remembering that in the linearized theory the Riemann tensor is invariant, as follows:

$$\ddot{\xi}^i = \frac{1}{2}\ddot{h}^{TT}_{ij}\xi^j. \quad (2.20)$$

So, we can say that the effect of GWs on a point particle of mass m can be described in terms of a Newtonian force, in the proper detection frame, as follows:

$$F_i = \frac{m}{2}\ddot{h}^{TT}_{ij}\xi^j. \quad (2.21)$$

Let's study the effect of a GW on test masses. Considering a ring of test masses in the proper detector frame initially at rest, with origin in the center of the ring, we can describe the distance of a test mass with respect to this origin by $\xi^i$. If a GW propagates along the z-direction and the ring is located in the (x; y) plane, the displacement will be in the (x; y) plane. In fact, the components of $h_{ij}^{TT}$ with i = 3 or j = 3 are zero, as a test particle initially at z=0 will remain at z=0: GWs displace the test masses transversely with respect to their direction of propagation. So, for instance, considering the + polarization (similarly for the cross polarization) and choosing $h_{ij}^{TT} = 0$ at t=0, we write at z = 0:

$$h_{ab}^{TT} = h_+ sin\omega t \begin{pmatrix} 1 & 0 \\ 0 & -1 \end{pmatrix}. \tag{2.22}$$

Moreover, we can write $\xi_a(t)$ with the displacements induced by GWs as $(\delta x(t), \delta y(t))$, and the unperturbed positions as $(x_0, y_0)$, as follows:

$$\xi_a(t) = (x_0 + \delta x(t), y_0 + \delta y(t)) \tag{2.23}$$

with a,b the indices in the transverse plane. For more details see [7].
Fig. 2.1 shows the effects of GWs on matter for both polarizations, where the waves enter perpendicular to the interferometer plane: the length of each arm is alternatively increased/decreased with opposite phase between them.
Finally, it's important to introduce also the energy and momentum carried

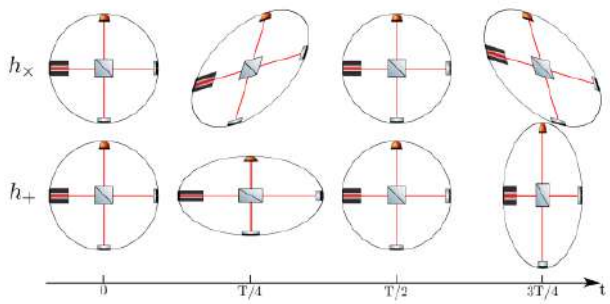


Figure 2.1: Effects of GW passing through a Michelson Interferometer with different polarizations (T is the period of the wave) [8].

by GWs. It is possible to demonstrate, through some calculations [7], the energy flux and the momentum flux respectively, defining the surface element dA as $r^2 d\Omega$, with $d\Omega$ the infinitesimal solid angle element and r widely distance from the GW source, as follows:

$$\frac{dE}{dt} = \frac{c^3 r^2}{32\pi G} \int d\Omega \left\langle \dot{h}_{ij}^{TT} \dot{h}_{ij}^{TT} \right\rangle \tag{2.24}$$

$$\frac{dP^k}{dt} = -\frac{c^3 r^2}{32\pi G} \int d\Omega \left\langle \dot{h}_{ij}^{TT} \partial^k h_{ij}^{TT} \right\rangle. \tag{2.25}$$

## 2.2 Sources of gravitational waves

Since the interaction of GWs with matter is very weak, we are able to detect only gravitational waves emitted by astrophysical sources with large masses and relativistic speeds. We can distinguish astrophysical sources according to the temporal behavior of the signal they generate, as follows [9]:

- *Periodic sources*, which have a periodic or quasi-periodic signal (pulsar, inspiralling neutron stars or black holes binaries);
- *Transient and impulsive sources*, which have a transient or impulsive signal characterized by a time duration shorter than the typical time of observation (supernovae explosion and merging coalescent binaries);
- *Stochastic background*, i.e. signals which have statistical fluctuations with a time duration longer than the typical observation time. We can distinguish between the random background of GWs generated in the first instants after the Big Bang (evolution of the Universe) and the astrophysical background of GWs, i.e. superposition of radiation emitted by sources in the Universe (history of the formation and evolution of astrophysical sources).

Even if the pulsar amplitude is slower than the amplitude of other sources, being a periodic source, can be observed for a longer time.
On the other hand, the most detectable GW signals are those emitted by a binary system composed by compact objects (two black holes, two neutron stars or a black hole and a neutron star), since their frequency, for a certain interval of masses, belong to the more sensitive ground-based detectors frequency band (10-10000 Hz).
Concerning the impulsive GW sources, such as supernovae, a good amount of gravitational radiation is emitted with a very little emission time, the bigger expected signal, but very rare.
Other GW sources are magnetars, isolated neutron stars with a very strong magnetic field able to produce GWs by their mechanical vibration modes. Depending on the type of vibrational modes, the emitted GW signal will have a frequency comes from 10 to 2000 Hz.
Therefore, given the nature of gravitational wave signals emitted by astrophysical sources, it is essential to improve the sensitivity of GW detectors, especially at medium-low frequencies.

## 2.3 Gravitational wave detector

In 1974, Taylor and Hulse proved the existence of gravitational waves by the discovery of the binary system PSR1913+16, observing a pulsar with an anomalous behavior of its period due to the presence of a neutron star,

forming a binary system [10].
Thanks to terrestrial's network of gravitational wave detectors, 90 events have been detected up to now, including a Binary Neutron Star (BNS) merger (GW170817 [2]), two Neutron Star–Black Hole (NSBH) events (GW200105 and GW200115 [6]) and all the others Binary Black Hole (BBH) system (the first direct observation of GWs from GW150914 [1]).

### 2.3.1 Network of terrestrial GW detectors

Gravitational wave detectors use laser interferometry [11] to detect the very small perturbations ($\Delta L \sim 10^{-18} m$) given by the passage of a GW on the optical path of the light that is moving back and forth between test masses (see section 2.3.2).
In Figure 2.2 the localization of LIGO [12], VIRGO, GEO600 and KAGRA

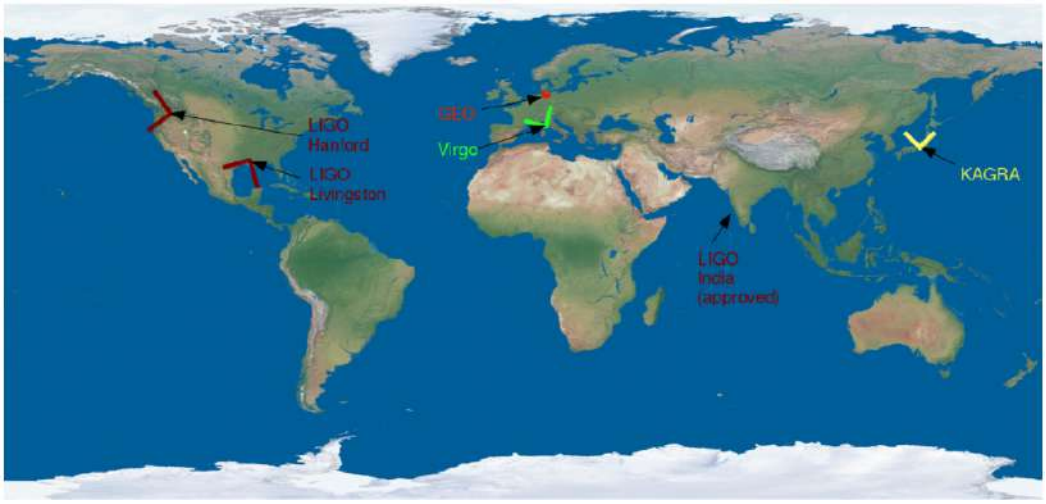


Figure 2.2: Localization of the present and future terrestrial GW interferometers in the world.

interferometers is shown. To localize a source of GWs, a triangulation process is necessary, so we need at least three detectors placed at different positions on Earth. The terrestrial network of operating GWs interferometers (ITFs) is composed by:

- the two 4-km long interferometers of the Laser Interferometer Gravitational Observatory (LIGO) located in the United States near Livingston, Louisiana and Hanford, Washington State;
- the 3-km long interferometer of VIRGO located in Italy near Pisa;
- the 3-km long interferometer of KAGRA [13], a GW detector with cryogenic mirrors to minimize the thermal noise on test masses and

located underground in Kamioka mine (Japan) to provide seismic isolation for the detector operation. KAGRA has joined the network in 2019, during the last observation run (O3) and will partecipate with ALIGO+ (Advanced LIGO Plus) and AdV+ (Advanced Virgo Plus) in the next observing period O4, starting from 2023;

- the 600-m long interferometer of GEO600, which operates in Germany near Hannover, is designed to test for many technological developments used in long arm gravitational.

Gravitational wave detectors operating with greater sensitivity are the two LIGOs and VIRGO detectors. For the next observative run O4, the expected binary neutron star (BNS) detection range, that is the distances at which the merger of a BNS system gives a matched filter signal-to-noise ratio (SNR) of 8, for ALIGO+ will be between 160-190 Mpc and for AdV+ 80-115 Mpc. The distances are averaged over all the possible sky localisations and binary orientations.

### 2.3.2 Laser interferometry

GWs detectors are based on the principle of laser interferometry: a continuous wave light from a laser is divided into two beams with a beamsplitter (BS); the beams then travel along the two perpendicular arms of the ITF and are reflected back to the BS where they interfere and are directed to the photodetector, which converts the intensity into an electric signal. Any change in the optical path difference between the arms results in a change in the interference signal, like the one due to GWs pass. GW interferometers use Fabry-Perot (FP) cavity in each arm to artificially increase the length of the arms [14] (Fig. 2.3). Moreover, in addition:

- a Power Recycling cavity (PRC) is used to increase the circulating laser power inside the arm cavities;

- a Signal Recycling cavity (SRC) to boost the GW signal;

- mirrors are suspended to filter seismic noise;

- whole the system is in vacuum ($10^{-8} mbar$) to avoid the gases refractive index variation;

- Input and Output Mode Cleaner cavities (IMC and OMC) are used to filter the laser beam;

- Faraday Isolators are used to attenuate back-reflected and back-scattered light.

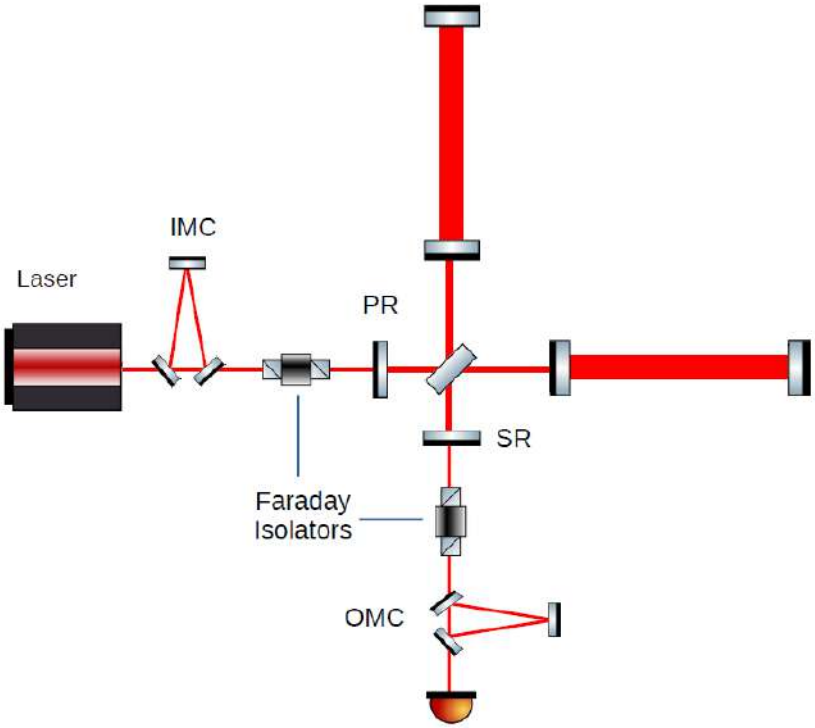


Figure 2.3: The schematic layout of a terrestrial Gravitational Wave detector.

### Interaction of a GW with a FP cavity

Let's summarize the interaction of a GW with a FP cavity [7].
It is demonstrated that, through some calculations, the effective mean time of the photons $\tau_s$ in the FP cavity becomes $\frac{LF}{c\pi}$ and the phase shift sensitivity is improved by the factor $\frac{2F}{\pi}$, where F is the finesse defined as the ratio of the free spectral range to the width at mid-height of a resonant FP cavity. Since in a GW detector we measure a phase shift, the same response to the GWs is obtained by replacing the hypothetical arms with a length of hundreds of km by FP cavities with a length of a few km and finesse $\mathcal{O}(10^2)$.
Let us consider a FP cavity oriented along the x-axis (as shown in Fig. 2.4) and a GW with only plus-polarization propagating along the z-axis given by:

$$h_+(t) = h_0 cos(\omega_{GW} t). \tag{2.26}$$

We want to calculate how the field reflected from a cavity FP is affected by the arrival of GWs.
In the Proper Detector Frame, the light propagates along the geodesics of a flat spacetime, while the mirrors are shaken by a force exerted by the GWs

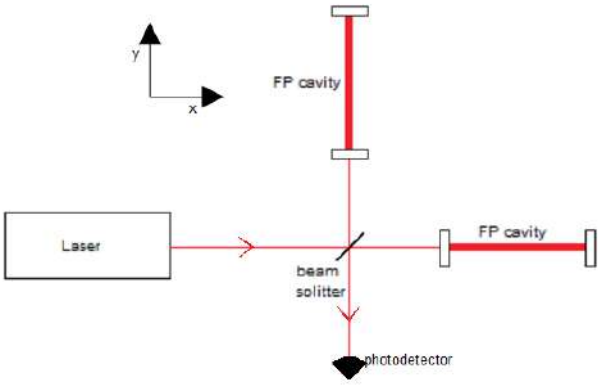


Figure 2.4: The schematic layout of a realistic Gravitational Wave interfermeter.

whose motion is given by:

$$\xi_x(t) = L_x + \frac{h_0 L_x}{2} cos(\omega_{GW} t); \tag{2.27}$$

therefore the length L of the cavity changes as

$$\Delta L_x(t) = \frac{h_0 L_x}{2} cos(\omega_{GW} t). \tag{2.28}$$

This induces a change $\Delta\phi_x$ in the phase of the field reflected from the cavity along the arm x, given by:

$$\Delta\phi_x = \frac{4F}{\pi} k_L \Delta L_x. \tag{2.29}$$

Similarly, by inverting the sign of $h_0$, we can obtain the phase shift of an FP cavity along the y-arm, thus the total phase shift in the FP interferometer is as follows:

$$\Delta\phi_{FP}(t) = \Delta\phi_x - \Delta\phi_y = 2\Delta\phi_x = |\Delta\phi_{FP}| cos(\omega_{GW} t) \tag{2.30}$$

with $|\Delta\phi_{FP}| = \frac{4F}{\pi} k_L L h_0$. This would be the change of phase in a Michelson interferometer with arm-legth $\frac{2FL}{\pi}$.
So, if a GW induces a phase shift in the reflected field from a cavity along the x-axis, this produces reflected field sidebands of frequencies $\omega_L \pm \omega_{GW}$ and amplitude for each sideband of $|\Delta\phi_x|/2$. If we want the result of $|\Delta\phi_x|$ for $g_{GW}\tau_s$ generic, we have to work with the TT gauge description [7]. It is demonstrated that we can find the phase shift in a FP interferometer as follows:

$$|\Delta\phi_{FP}| \simeq \frac{h_0 4FLk_L}{\pi\sqrt{1 + (f_{GW}/f_p)^2}} \tag{2.31}$$

with the pole frequency $f_p \equiv \frac{1}{4\pi\tau_s} \simeq \frac{c}{4FL}$.
We can conclude that:

- for $g_{GW} \ll f_p$, we can
  find the result of the proper detector frame;
- at $g_{GW} \gg f_p$ the sensitivity degrades linearly with $f_{GW}$;
- equation (2.31) holds as long as $\omega_{GW} L/c \ll 1$, i.e.

$$f_{GW} \ll \frac{c}{2\pi L} \simeq 12kHz\frac{4km}{L}. \tag{2.32}$$

  Above this frequency, the response is cut indicating the fact that in each round-trip the GW changes sign.

### 2.3.3 Sources of noise

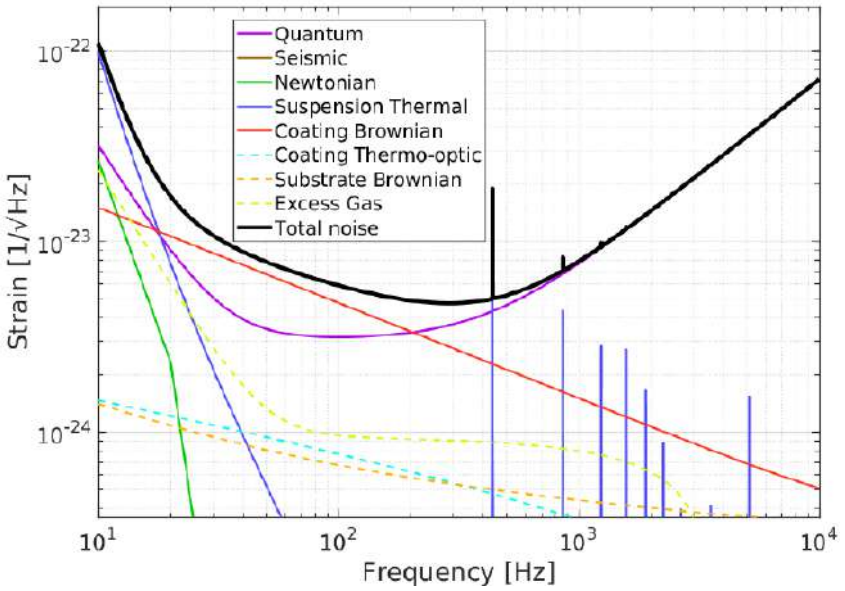


Figure 2.5: The main sources of noise that limit the sensitivity curve of a GW detector.

Many sources of noise affect the sensitivity of GW interferometers and the effect of GWs is so tiny and hidden behind a multitude of noise signals that it takes very smart data analysis techniques to detect them: essentially we try to identify their pattern by comparing the experimentally observed ripples with those calculated according to the Einstein theory.
So, noises are phenomena that can simulate or hide GW signals and they can be divided into:

- fundamental noises, which depend on fundamental physical phenomena or they cannot be eliminated if not changed the configuration completely of the ITF or the infrastructure (quantum noise, seismic noise, newtonian noise and suspension thermal noise);

- technical noises, that can be checked if recognized and reduced (electronic noise, control noise..).

As shown in Figure 2.5, the measured output of each interferometer, or the sensitivity curve, is calibrated in units of gravitational wave strain as a function of frequency range of 10-10000 Hz. The black curve is the envelope of all noise contributions.
At high frequency band, the detector is mainly limited by quantum noise shown as purple curve. *Quantum noise* will be widely discussed in the next section 2.3.4 [15].

*Thermal noise* appears in the medium frequency band, which is also the

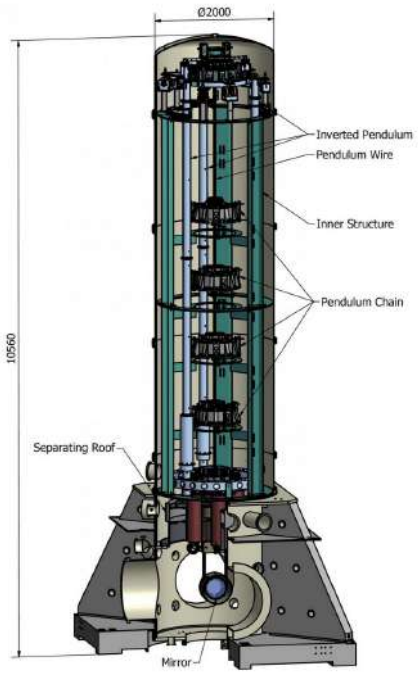


Figure 2.6: Super Attenuator in Virgo detector. Each mirror is suspended, under vacuum, from a mechanical structure that greatly reduces seismic vibrations and consists of a chain of pendulums suspended from a platform, supported by three long flexible legs, fixed to the base: technically a reversed pendulum. In this way the seismic vibrations at frequencies higher than 10 Hz are reduced by over $10^{12}$ times and the position of the mirror is very carefully controlled.

most sensitive frequency band for many astrophysical sources. This noise arises due to the random thermal motion in test masses and their suspensions [16]. It can be minimized to improve the sensitivity of the GW detectors choosing a material with high strength and low mechanical loss for test masses, like silica and tantala multilayer for the coatings, and the suspension fibers, such as fused silica [17]. Also, the coating is made to have reflective mirrors at the operational wavelength (1064 nm) and so that less than 0.0001 % of the laser light is lost when it is reflected by the mirror (due to the absorption, residual transmission, or scattering).
*Seismic noise* limits the low frequency band below 10 Hz (off the graph of Fig. 2.5) and it is due to the environmental disturbances such as ocean tides, seismic/volcanic activity, wind, that couple to the test of the GW interferometers. The interferometer optics needs to be isolated well from the ground seismic vibrations: in Virgo detector, a seven stage Super Attenuator (SA) is used to allow the interferometer's operation (Fig. 2.6).
A relevant noise at frequency band below ∼20 Hz is so-called *Newtonian Noise* (shown as green curve in Figure 2.5), which is due to terrestrial gravity fluctuations produced by density fluctuations of Earth around the test masses of the interferometer. To reduce Gravity Gradient noise, a set of seismometers will be installed around the test masses to record the ground motion that can provide information about the mass density fluctuations around the test masses. Such information is then used to calculate the corresponding gravitational force fluctuations on the test mass, and so to correct the strain data from the interferometer.

### 2.3.4 Quantum noise

Gravitational wave effects on the test masses can be confused with the effect of vacuum fluctuations of the optical fields that enter the dark port of the detector.
*Quantum noise* affects the entire bandwidth of the GW interferometers (10-10000 Hz) with its complementary features: the shot-noise (SN), which depends on phase fluctuations of the optical field disturbing the detector at high frequencies, and radiation-pressure noise (RPN), which depends on amplitude fluctuations of the optical field perturbing the position of suspended mirrors at low frequencies (below 100 Hz). Let's see them in detail.
A light field consists of photons that arrive at the photodetector at random times [18]: this leads to the *photon shot-noise*. In the absence of correlations, photons follow Poisson distribution with probability to find n photons as follows:

$$p_n = \frac{\langle n \rangle^2}{n!} e^{\langle n \rangle}, \tag{2.33}$$

where $\langle n \rangle$ is the average number of photons that is also the variance of the distribution. Moreover, the light field pushes against the end mirror and

moves them: this creates the so-called *radiation-pressure noise*.
In interferometric gravitational wave detectors, quantum noise can be seen as arising from zero-point fluctuations of the vacuum electromagnetic field entering the output port of the interferometer [19]. The quantum fluctuations of the vacuum field produce SN and RPN respectively with the single-side power spectral densities (position-noise):

$$S_x^{SN} = \frac{c^2\hbar}{2\omega_0 P}, \tag{2.34}$$

$$S_x^{RPN}(\omega) = \frac{\hbar\omega_0 P}{c^2 m^2 \omega^4}, \tag{2.35}$$

where P is the power of laser, m the mass of the mirror, $\hbar$ is the reduced Planck's constant, c is speed of light and $\omega$ the sideband frequency (above the resonance frequency of the mirror suspension). So, shot noise is inversely proportional to the power laser and radiation pressure is proportional to P. From equations (2.34) and (2.35) is clear that RPN is dominant at low frequencies, while SN dominates at high frequencies. Indicating by h($\omega$) the noise spectral density of the strain $\frac{\Delta x}{L}$ of an interferometer, we obtain:

$$h^{SN}(\omega) = \frac{1}{L}\sqrt{S_x^{SN}} = \frac{c}{L}\sqrt{\frac{\hbar}{2\omega_0 P}}, \tag{2.36}$$

$$h^{RPN}(\omega) = \frac{1}{L}\sqrt{S_x^{RPN}(\omega)} = \frac{2}{L}\frac{1}{mc\omega^2}\sqrt{\hbar\omega_0 P}, \tag{2.37}$$

where L is the arm lenght of the interferometer and in eq. (2.37) we have taken into account RPN twice (contributions of the two end mirrors). From eq. (2.34) we notice that shot-noise is a white noise because it doesn't depend on wave frequency to be detected. Moreover, increasing the laser power, shot-noise is reduced, but radiation-pressure noise is increased and vice versa.

The *total quantum noise* is given by the sum of shot noise and radiation pressure noise as follows:

$$h^{QN} = \sqrt{(h^{SN})^2 + (h^{RPN}(\omega))^2}. \tag{2.38}$$

The locus of the lowest possible points of the family of spectra is the *standard quantum limit* (Fig. 2.7) that is mathematically written as:

$$h^{SQL}(\omega) = \frac{1}{\pi\omega L}\sqrt{\frac{\hbar}{m}}. \tag{2.39}$$

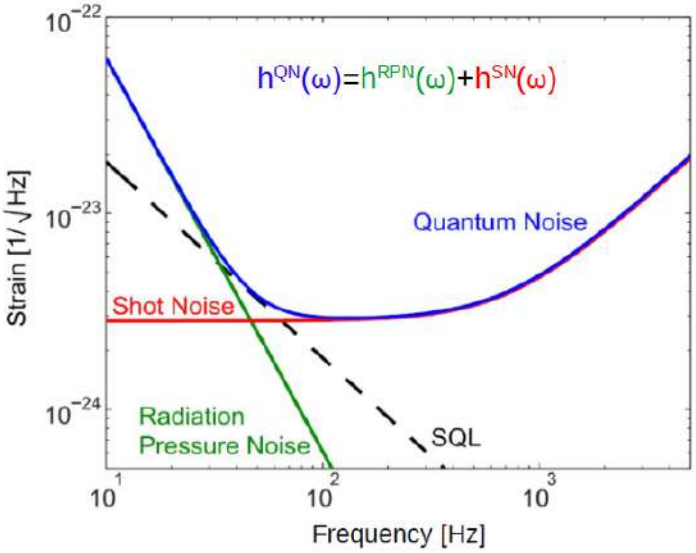


Figure 2.7: The plots represents the combined effect of shot-noise (red) and radiation-pressure noise (green), obtaining the corresponding Standard Quantum Limit, SQL, with the black dotted line, i.e. the minimum value that can be achieved by the spectral density at that value of frequency and it is a manifestation of the Heisenberg uncertainty principle.

### Quantum mechanical description of light

In this section we will provide fundamentals of quantum mechanics to describe light [20].
Light can be described as quantum harmonic oscillator by its Hamiltonian:

$$\hat{H} = \frac{1}{2}(\hat{p}^2 + \omega^2 \hat{q}^2), \tag{2.40}$$

where $\hat{p}$ and $\hat{q}$ are the position and momentum operators and $\omega$ the angular frequency. We can introduce the annihilation and creation operators $\hat{a}$, $\hat{a}^\dagger$ to replace $\hat{p}$ and $\hat{q}$ as follows:

$$\hat{a} = \frac{1}{\sqrt{2\hbar\omega}}(\omega\hat{q} + i\hat{p}) \tag{2.41}$$

$$\hat{a}^\dagger = \frac{1}{\sqrt{2\hbar\omega}}(\omega\hat{q} - i\hat{p}) \tag{2.42}$$

which obey the commutation relation $[\hat{a}, \hat{a}^\dagger] = 1$. Since the annihilation and creation operators are not observable, we introduce the amplitude and phase quadratures starting from them:

$$\hat{X} = \hat{a}^\dagger + \hat{a} \tag{2.43}$$

$$\hat{Y} = i(\hat{a}^\dagger - \hat{a}) \tag{2.44}$$

that obey the commutation relation $[\hat{X}, \hat{P}] = 2i$. The amplitude and phase quadratures are dimensionless, Hermitian and proportional to electric fields. Then, the Hamiltonian can be rewritten in the new form:

$$\hat{H} = \hbar\omega(\hat{X}^2 + \hat{Y}^2), \tag{2.45}$$

where the variance of an operator $\hat{X}$ is given by:

$$\Delta^2\hat{X} = \left\langle \hat{X_1}^2 \right\rangle - \left\langle \hat{X_1} \right\rangle^2. \tag{2.46}$$

So, eq. (2.46) provides the quantum noise of the observable.
Now, we define the number operator:

$$\hat{n} = \hat{a}^\dagger\hat{a} \tag{2.47}$$

that expresses the number of photons in a given state. For the ground state of the oscillator we have $\langle\hat{n}\rangle = 0$ with a variance of $\Delta^2\hat{X} = \Delta^2\hat{Y} = 1$. This is referred to as vacuum noise and the state in which there are no photons $|0\rangle$ is called *vacuum state*. Vacuum state is the ground state of the harmonic oscillator that is the state with the lowest energy.
Quantum noise results from the zero-point energy of the ground state that is given by:

$$\langle 0|\,\hat{H}\,|0\rangle = \frac{\hbar\omega}{2}. \tag{2.48}$$

The quantum-mechanical equivalent of a classical monochromatic electromagnetic wave is called *coherent state*. Laser light can be described by coherent states in Dirac notation $|\alpha\rangle$ with a Poissonian distribution photon number, where $\alpha$ is a complex number. Coherent states are defined as eigenstates of the annihilation and creation operators $\hat{a}$, $\hat{a}^\dagger$. Mathematically, they can be described applying the displacement operator to the vacuum state:

$$|\alpha\rangle = e^{(\alpha\hat{a}^\dagger - \alpha^*\hat{a})}\,|0\rangle\,. \tag{2.49}$$

Every state has to obey *Heisenberg uncertainty principle*:

$$\Delta^2\hat{X} \cdot \Delta^2\hat{Y} \geq 1, \tag{2.50}$$

in which we used $[\hat{X}, \hat{P}] = 2i$. Relation (2.50) is true for all other orthogonal quadrature operators. We define the generalized quadrature operator with an arbitrary angle $\theta$ between the amplitude and the phase quadrature applying a rotation:

$$\hat{X}_\theta = \hat{X}cos\theta + \hat{Y}sen\theta. \tag{2.51}$$

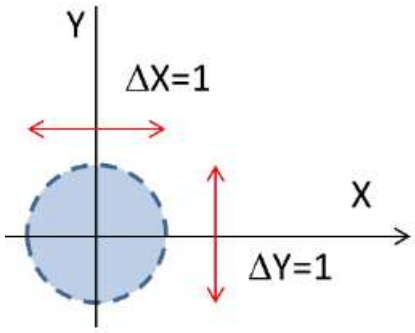


Figure 2.8: Representation of a vacuum state.

Moreover, state of light can be visualized in a *phase space* with "phase quadrature operator" in the ordinate axis and "amplitude quadrature operator" in the abscissa axis as shown in the Figure 2.8. For coherent states, the quantum uncertainty is depicted with a circle around its amplitudes. Fig. 2.8 represents the quantum fluctuations which have a gaussian distribution around the mean value. Also, coherent states have Poissonian photon number fluctuations

$$\Delta n = |\alpha| = \sqrt{\langle n \rangle} \tag{2.52}$$

and therefore generate shot-noise.

### Quantum noise reduction strategy

Quantum noise can be reduced by injecting squeezed vacuum states from the dark port of the GW detector. In fact, *squeezed states* have a reduced variance for at least one angle $\theta$ (below the vacuum variance), called *squeeze angle*, i.e. with $\Delta^2 \hat{X}_\theta$ the lowest of all quadratures [21] and their quantum uncertainty is depicted with an ellipse around their amplitude [22]. We define the squeeze operator $\hat{S}(\xi)$:

$$\hat{S}(\xi) = e^{\frac{1}{2}(\xi^*(\hat{a})^2 - \xi(\hat{a}^\dagger)^2)}, \tag{2.53}$$

where $\xi = re^{i\theta}$ and r and $\theta$ are respectively squeeze parameter and angle.

The use of phase-squeezed light allows interferometric measurements with greater precision than that obtained with a coherent state. Similarly, the use of amplitude-squeezed light gives smaller amplitude noise than that of a coherent state. Hence, amplitude-squeezed light has sub-Poissonian photon statistics, i.e. $\Delta n < \sqrt{\langle n \rangle}$, and produces a smaller noise level in optical detection than the SN limit. The observation of photodetection noise below the shot-noise limit is thus one of the ways that squeezed states are detected

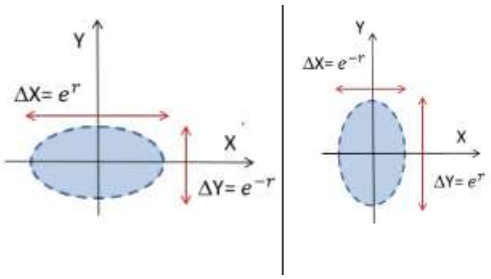


Figure 2.9: Representations of a phase-squeezed vacuum state (on the left) and amplitude-squeezed vacuum state (on the right) of light in a phase space. The quantum uncertainty is depicted with an ellipse.

in the laboratory.
Squeezed beams are generated by nonlinear optics and are detected by the homodyne detector technique [23].

**Squeezed light generation and detection**

To generate nonclassical states like squeezed states, we need higher-order polarization effects in media. Consider the polarization *P(E(t))* due to an electro-magnetic wave traveling through a nonlinear medium [24]:

$$P(E(t)) = \epsilon_0(\chi^{(1)}E(t) + \chi^{(2)}E(t)^{(2)} + \chi^{(3)}E(t)^{(3)} + ..), \tag{2.54}$$

where $\chi$ is the susceptibility and $E(t) = E_0 cos\omega_p$. We are interested in those materials that manifest a second-order nonlinearity. The second-order nonlinear response generates an oscillating polarization at the sum and difference frequencies of the input fields according to:

$$\omega_{sum} = \omega_1 + \omega_2, \tag{2.55}$$

$$\omega_{diff} = |\omega_1 - \omega_2|\,. \tag{2.56}$$

The generation of these new frequencies by nonlinear processes is called *sum frequency generation* and *difference frequency generation*, respectively [25].

If $\omega_1 = \omega_2$, the sum frequency is at twice the input frequency, and the effect is called *frequency doubling* or *second harmonic generation* as shown in Figure 2.10.
The core of the squeezing light generation involves a degenerate parametric amplifier (OPA), consisting of a second-order nonlinear crystal pumped by an intense laser beam at angular frequency $\omega_p = 2\omega_s$. A weak signal beam at angular frequency $\omega_s$ is also introduced. The nonlinear crystal mixes the signal with the pump and produces an idler beam at angular frequency $\omega_i$ by difference frequency mixing, where

$$\omega_i = \omega_p - \omega_s = 2\omega_s - \omega_s = \omega_s. \tag{2.57}$$

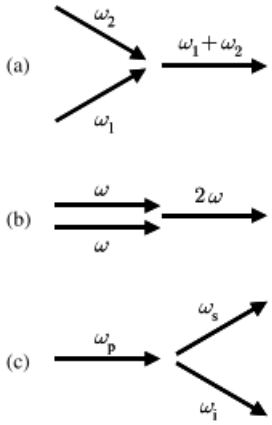


Figure 2.10: Diagrams for second-order nonlinear processes. (a) In sum-frequency generation, two input photons at frequencies $\omega_1$ and $\omega_2$ are annihilated and a third one at frequency $\omega_1 + \omega_2$ is created. (b) In frequency doubling the two input photons are at the same frequency, and the output photon is at double of the input frequency. (c) In down-conversion an input photon at the pump frequency $\omega_p$ is annihilated and two new photons at the signal and idler frequencies $\omega_s$ and $\omega_i$, respectively, are created [18].

These idler photons then mix again with the pump to produce more signal

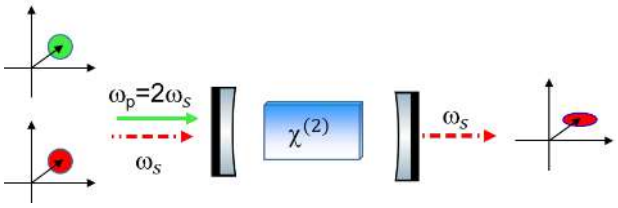


Figure 2.11: The mechanism of a non-linear optic, in this case an Optical Parametric Oscillator (OPO), to generate squeezed vacuum is shown.

photons, and so on. In the special case that we are considering here where the signal and idler photons are degenerate, the nonlinear process produces amplification or de-amplification of the signal depending on its phase relative to the pump field.
An OPO (Optical Parametric Oscillator), shown in Fig. 2.11, converts an input laser wave at frequency $\omega_p$ into two output beams at lower frequency, preserving the energy conservation principle. If the two output beams have the same frequency $\omega_s$, we have a degenerate OPO. If the down-conversion process produces two output waves at frequencies $\omega_s \pm \Delta\omega_s$, we have a non-degenerate OPO, where $\Delta\omega_s$ is the frequency of the sidebands with respect to the carrier at frequency $\omega_p$.

Second-harmonic generation is a parametric up-conversion process, in fact from two photons at the frequency $\omega$ creates one photon at the frequency $2\omega$, as shown in Figure 2.10.
Nonlinear processes such as second-harmonic generation or OPO are sensitive to the fluctuations in the instantaneous photon flux.
Moreover, as we said, squeezed beams can be detected by the homodyne detector technique [26]. A balanced homodyne detector is based on the interference between the squeezed vacuum beam (SQZ beam in Fig. 2.12) and a strong local oscillator (LO) on a 50:50 beam splitter at the same frequency, same spatial mode and same polarization [27]. The difference between the two generated photocurrents give us information about the squeezing level of the SQZ beam. Each outputs of the BS is detected by a photodiode and the degradation of the interference is quantified by the fringe visibility $\mathcal{V}is$, as follows:

$$\mathcal{V}is = \frac{V_{max} - V_{min}}{V_{max} + V_{min}} \tag{2.58}$$

with V the voltage of one photodiode while the phase between the two fields is modulated.
As shown in Fig. 2.12, starting from the output beams $\hat{c}$ and $\hat{d}$:

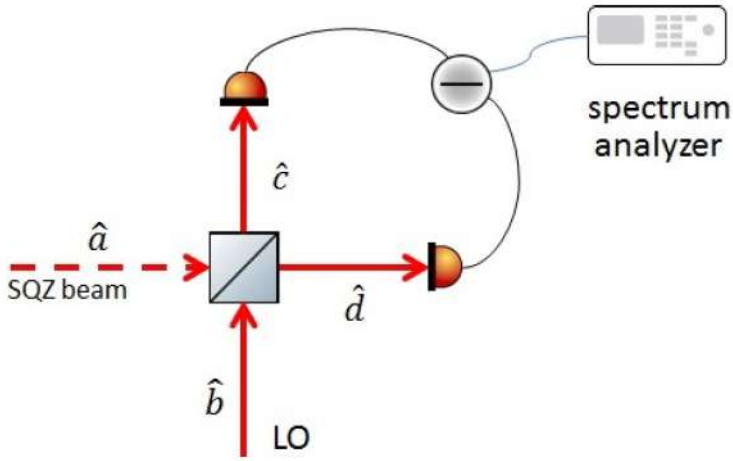


Figure 2.12: The schematic layout of a balanced homodyne detector [9].

$$\hat{c} = \frac{1}{\sqrt{2}}(\hat{a} + \hat{b}) \tag{2.59}$$

$$\hat{d} = \frac{1}{\sqrt{2}}(\hat{a} - \hat{b}) \tag{2.60}$$

the detected quantity can be written as follows:

$$P_1 - P_2 = \hat{c}^\dagger \hat{c} - \hat{d}^\dagger \hat{d} = 2\mathcal{R}(\hat{a} \cdot \hat{b}). \tag{2.61}$$

Also, two mechanisms degradate squeezing level which must be controlled and minimized: optical losses, that can be described as a recombination of the squeezed state with a vacuum state inside a beam splitter; phase noise, that mixes the fluctuations in the two quadratures.

# Chapter 3

# Background: FDS experiments

In this chapter, two different techniques relevant to the reduction of quantum noise, via frequency-dependent squeezing, are described: a detuned filter cavity installation [28] for Advanced Virgo Plus detector and Einstein-Podolsky-Rosen (EPR) entangled beams experiment for next generation GW interferometers.
During the last observing run, Frequency-Independent Squeezing (FIS) injection technique was implemented by Advanced Virgo and Advanced LIGO [29]. Since interferometric measurements were limited only by shot-noise, a quantum noise reduction at high frequencies was achieved injecting phase-squeezed light in the dark port of the interferometer. A simplified experimental setup of FIS is shown in Fig. 3.1.

Due to Heisenberg Uncertainty Principle, reducing the uncertainty of the

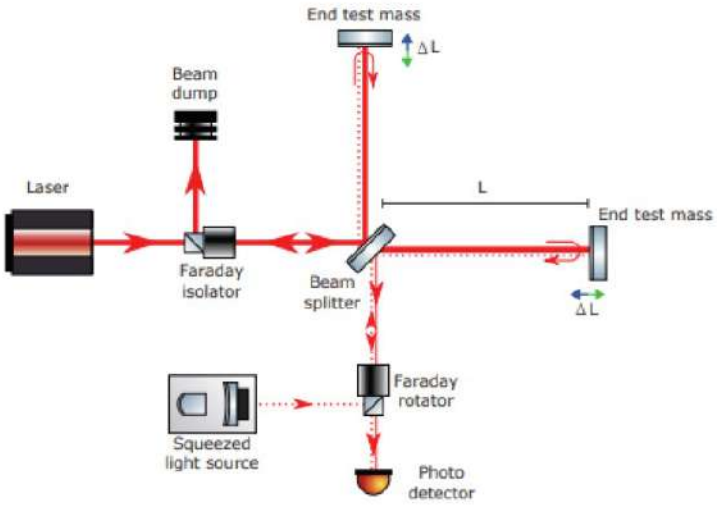


Figure 3.1: A simplified experimental setup of a squeezed light injection in a GW interferometer to reduce vacuum noise in one fixed quadrature [30].

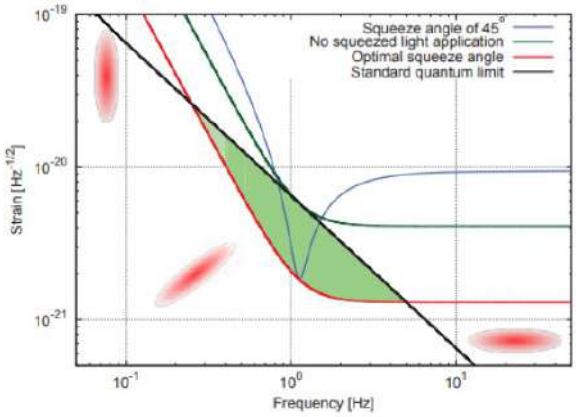


Figure 3.2: The strain sensitivity of Michelson Interferometer below the standard quantum limit with the 45° rotated squeezed angle application (green area) in the frequency range of 0.05 Hz to 50 Hz [30].

phase quadrature implies an increase of the amplitude uncertainty quadrature and vice-versa. Since, for the next observation run O4, quantum noise at low frequencies will be relevant for the detector sensitivity, a Frequency-Dependent Squeezing (FDS) injection is needed. So, in FDS experiments, the squeezing ellipse changes its orientation depending on the frequency. Moreover, as shown in Fig. 3.2, by using such as 45° of squeeze angle, correlations of the amplitude and phase quadratures in the output ports are introduced. So, within a small frequency band it is possible go below the standard quantum limit.

## 3.1 The Advanced Virgo Plus Filter Cavity

Since for the next observation run it is necessary to mitigate quantum noise in the entire bandwidth, Advanced Virgo Plus (the upgrade of Advanced Virgo) and Advanced LIGO Plus (the upgrade of Advanced LIGO [31]) installed a detuned cavity to achieve a frequency-dependent squeezing (see Fig. 3.3). In this section, the FDS system of AdV+ will be described.

AdV+ quantum noise reduction system is composed by three main systems: the squeezer, the filter cavity and the injection system. As shown in Fig. 3.4, the conceptual design is constitued by:

- the External sQueezing in-air Bench (EQB1, Fig. 3.5), which holds the squeezed source inside the AEI (Albert Einstein Institute) squeezer box, via a degenerate OPO (Optical-Parametric-Oscillator) to produce FIS. On EQB1 bench we have the single low-losses Faraday Isolator

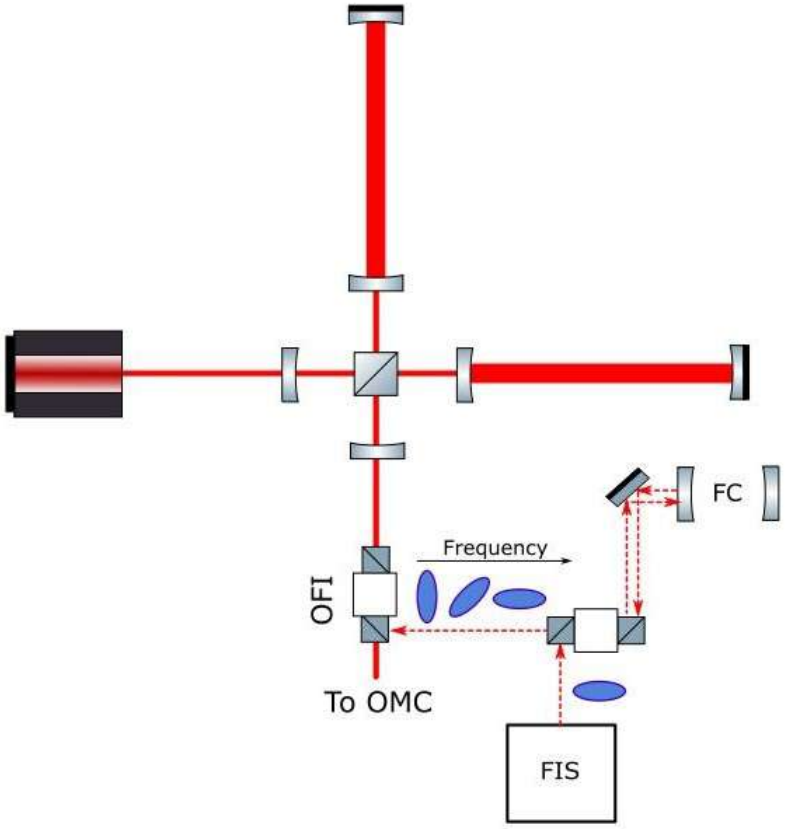


Figure 3.3: A simplified experimental setup of a frequency-dependent-squeezing injection achieved by a filter cavity detuned.

(see chapter 4) to preserve from spurious backscattered light to travel back along the SQZ beam path till the AEI squeezing vacuum source; we have also the homodyne detector for diagnostic measurements;

- two Suspended sQueezing in-vacuum Benches (SQB1 and SQB2, Fig. 3.6 and 3.7), which are used to align beams inside the filter cavity. In particular, on SQB1 bench we have the double low-losses Faraday Isolators (see chapter 4) which allow the SQZ beam to be sent back to the EQB1 or to be sent to the interferometer, via an Half-Wave-Plate (HWP);

- a 285 m-long Filter Cavity (FC, see Fig. 3.8), that is detuned w.r.t. the resonance frequency of the GW interferometer to achieve the rotation of the squeezing ellipse and then reflected from detuned optical cavities into the interferometer. However, since squeezed states strongly

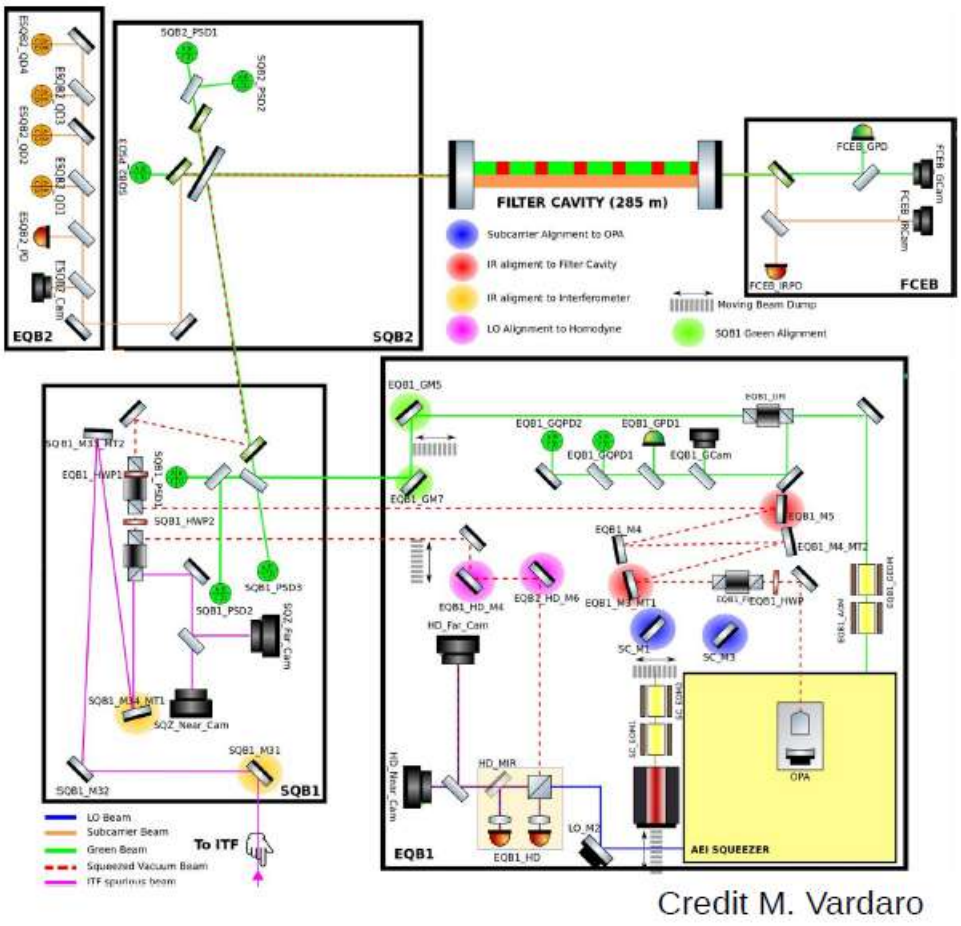


Figure 3.4: Conceptual design of Advanced Virgo Plus squeezing system [32].

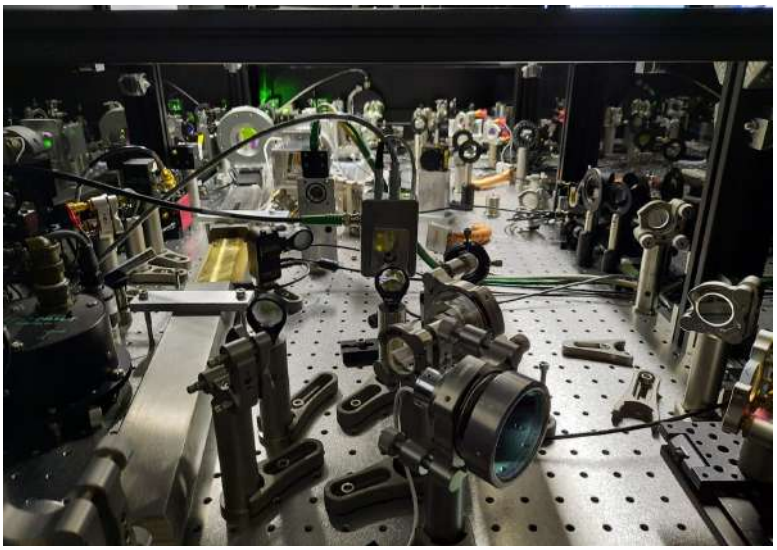

Figure 3.5: A picture of the external in-air squeezing bench (EQB1).

suffer from optical losses, the round trips inside filter cavity has to be minimized, so the cavity bandwidth is of the order of the detection bandwidth;

- two other external in-air benches (EQB2 and FCEB), which are used for the control loops.

In the following table, the filter cavity parameters are shown.

| | |
|---|---|
| Cavity length | 285 m |
| Free spectral range | 526 kHz |
| Mirror velocity | 1.4 um/s |
| Mirror mass | 3.5 kg |
| Finesse for GR | 117 |
| Finesse for IR | 11114 |
| IR FCIM transmissivity | 562 ppm |
| GR FCIM transmissivity | 2.6 % |
| IR FCEM transmissivity | 3.16 ppm |
| GR FCEM transmissivity | 2.7 % |
| IR cavity pole | 23.6 Hz |
| GR cavity pole | 2.25 kHz |

### 3.1.1 Filter cavity and squeezing benches control strategy

To have an efficient FDS injection on the interferometer, we have to minimize squeezing ellipse angle errors and also the optical losses on FC and on the interferometer (ITF). So, to ensure this, we need longitudinal and angular

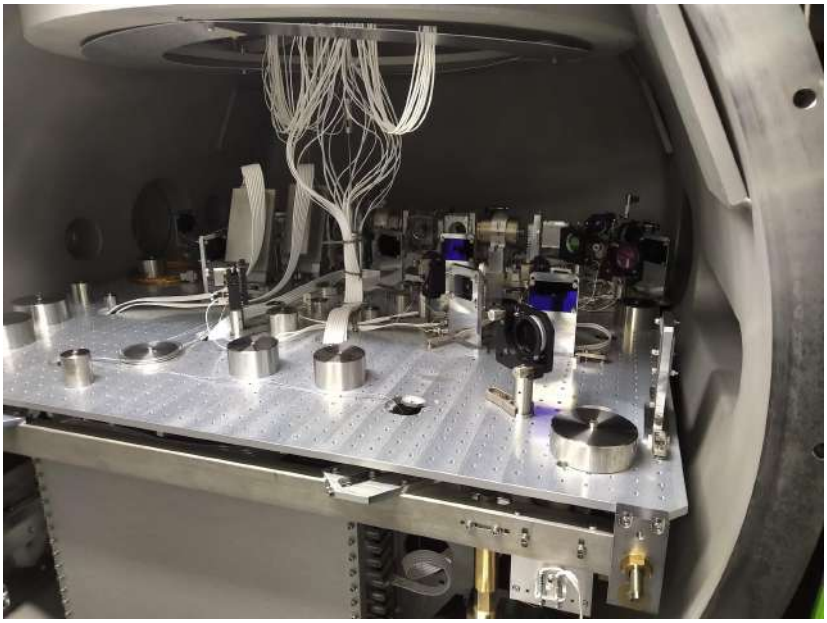

Figure 3.6: A picture of the suspended in-vacuum squeezing bench (SQB1).

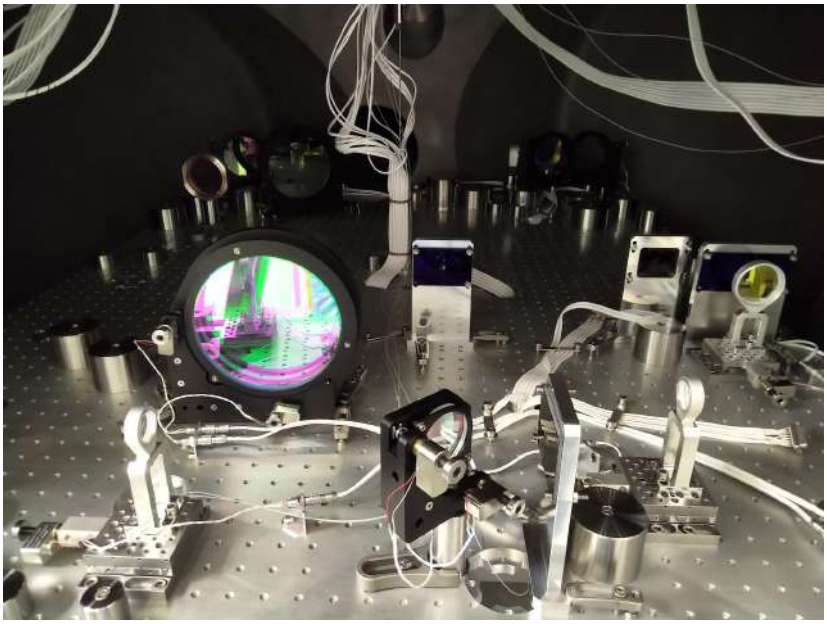

Figure 3.7: A picture of the suspended in-vacuum squeezing bench (SQB2).

Figure 3.8: A picture of the filter cavity (on the right), which is parallel to the North Arm of AdV+ (on the left).

controls on Filter Cavity, suspended benches control, automatic alignment and mode-matching of squeezed vacuum field on FC and ITF. Moreover, for AdV+ squeezing system, the required FDS injection is at 25-30 Hz of FC detuning, because the squeezing ellipse must be rotated where the shot-noise and radiation-pressure noise power densities are equal [33].
In order to keep the alignment between the three main systems, auxiliary beams are used in AdV+ squeezing system. In fact, in addition to the squeezed vacuum beam generated by the OPA inside the AEI squeezer box on EQB1 bench, we have (see Fig. 3.9):

- the sub-carrier beam, which is an IR field detuned w.r.t. the squeezed field by 1.26 GHz, used to align and control the filter cavity on IR. With this frequency shift, subcarrier beam is resonant inside the FC, makes ensure that the squeezed vacuum field is detuned from the FC resonance by 25-30 Hz (target for AdV+ FDS system), it not interferes with coherent control beam (which is 4 MHz shifted w.r.t. squeezer main laser), it is completely reflected by the interferometer Output Mode Cleaner and it has a negligible impact with the interferometer controls. This beam propagates towards the OPA, across the single low-losses Faraday Isolator, to ensure a perfect spatial mode-matching and overlapping with the squeezed beam, in order to guide the SQZ field from the AEI squeezer Box to the filter cavity;

- the local oscillator beam, used to perform squeezing measurements on the homodyne detector, is provided from the AEI squeezer box, it has the same frequency of squeezed beam and it is mode-matching to the squeezed vacuum field coming from the FC;

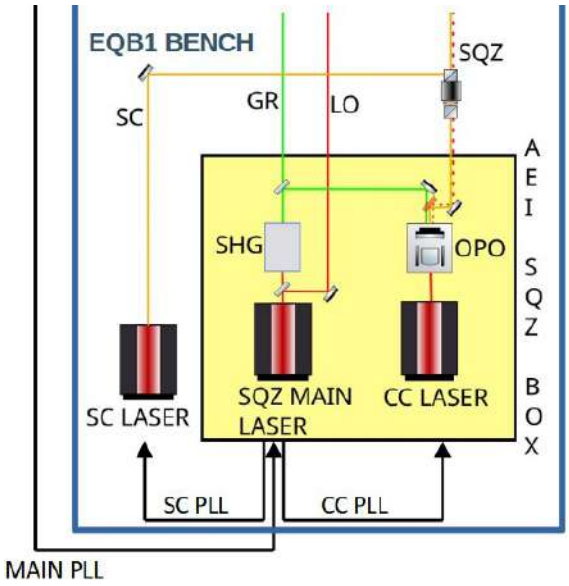


Figure 3.9: A schematic layout of the AEI Squeezer Box with all the beams for AdV+ squeezing system.

- the green beam, which comes from the AEI squeezer box, is used to control and automatic align the FC and also to control the suspended benches;
- the coherent control beam, from an auxiliary laser inside the AEI squeezer box (CC laser in Fig. 3.9), which has an offset of 4 MHz from the SQZ main laser, and it is transmitted through the OPA to generate the signal for the phase-control of the SQZ ellipse angle;
- interferometer spurious beam, used to overlap the SQZ beam with the interferometer beam, both for alignment and for mode-matching.

Moreover, in Fig. 3.9 are also shown the phase-locking systems (PLL) between the Virgo Main Laser and the squeezer main laser (MAIN PLL), the squeezer main laser and the subcarrier laser (SC PLL) and the squeezer main laser and the CC laser (CC PLL).

For the QNR system, we can operate in three different modes: injecting FDS in the interferometer, FIS in the interferometer or performing squeezing measurements on homodyne detector.
Let us briefly outline the global control strategy for squeezing measurements on homodyne detector.

- The FC longitudinal control procedure includes two Pound-Drever-Hall (PDH) techniques using the RF photodiodes in reflection of the

FC to generate the error signals (see Fig. 3.10 and Fig. 3.11): since the Finesse of the cavity for the IR is very high, the direct lock on IR beam is difficult, so at first the cavity is controlled using the green beam and then is switched on the IR subcarrier beam, in order to optimize the cavity length and to fine tune the cavity detuning. Two more photodiodes in transmission of FC (for green and IR beams) are installed to trigger the PDH loops.

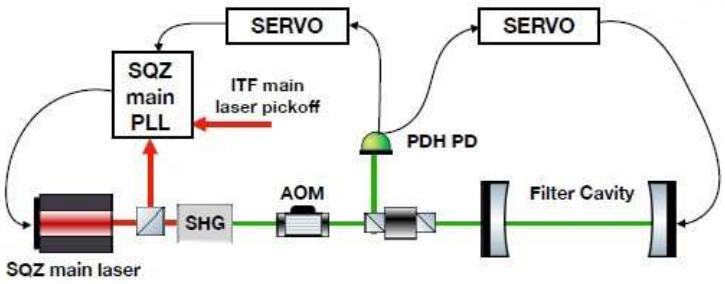


Figure 3.10: Filter cavity longitudinal control with green beam using Pound Drever Hall Technique [34]. Moreover, a feedback to laser frequency up to $\sim$ 900 Hz is added to suppress noise in the $\sim$ 100 Hz region [35].

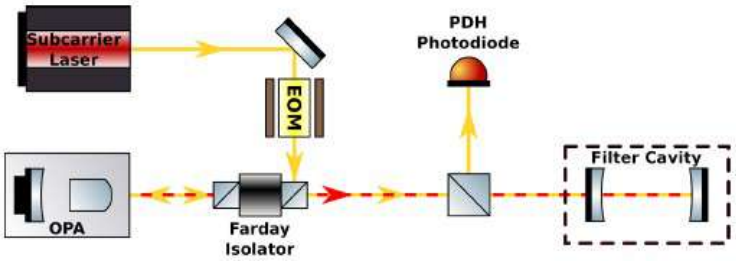


Figure 3.11: A schematic optical layout of the FC lock on IR sub-carrier beam, in which the red beam is the squeezed vacuum beam, and the yellow beam is the SC beam [33].

- Concerning the angular control, the filter cavity is aligned on green beam through an auto-alignment loop with standard Differential Wavefront Sensing (DWS) by a pair of quadrant photodiodes (QPDs) on EQB1 bench, which sense green beam reflected from the filter cavity (see Fig. 3.12). The two QPDs have a Gouy phase difference close to 90 deg and, demodulating the QPDs signals at the RF green beam sidebands (sidebands generate by an EOM on EQB1 bench), we can detect angular error signals arising from the beatnote between the carrier fundamental TEM00 of FC and the RF sideband of TEM01 or TEM10. The error signals are then fed to the angular actuators of

FC mirrors. In addition, in order to control the centering of the green beam on the filter cavity mirrors, we have developed a beam pointing control loop.

- Concerning the IR angular control, SC with SQZ vacuum fields are aligned on FC using the same kind of sensing of the green, but in this case the two QPDs are on EQB2 bench, detecting a small pick-off of the subcarrier field reflected from FC. The IR AA loop is closed on two actuators on EQB1 bench. Moreover, since SC beam is our reference for IR AA loop, another SC AA loop perfectly aligns SC in OPA, using dither lines technique (see chapter 7 for more details). However, on homodyne detector, we have to switch-off SC beam and consequently the IR AA loop, therefore there could be some drifts between green and IR beams during measurements with homodyne detector.

- Via an acousto-optic modulator on EQB1 bench, we can slightly detune the green beam resonance inside the filter cavity, allowing the simultaneous resonance of the infrared beam (see chapter 5 for more details).

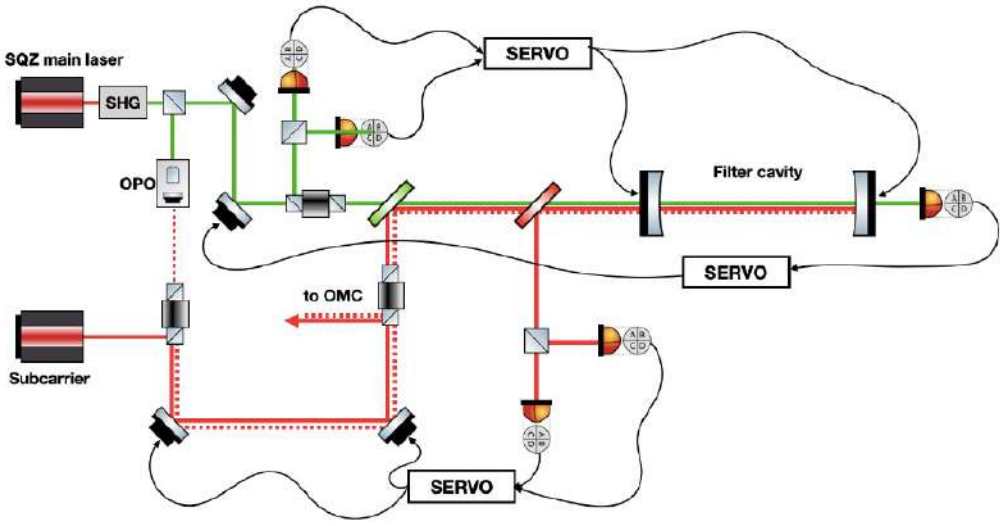


Figure 3.12: Optical scheme of filter cavity angular controls [35].

- Concerning the control of suspended benches, on each suspended bench three DC QPDs are installed to sense the near-field and far-field of green beam to provide error signals in order to stabilize the position of laser spots on the optics.

- Since the homodyne detector is on EQB1 bench and the IR beams travel the suspended benches to reach filter cavity and back, causing

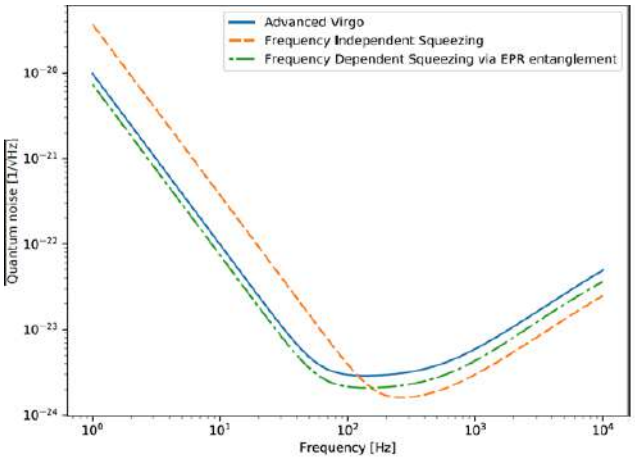


Figure 3.13: Comparison between simulation of Advanced Virgo configuration (solid blue), 12 dB of frequency-independent squeezing injection (dashed orange) and in case of 12 dB of FDS injection via EPR entanglement (dot-dashed green) [37].

long-term drifts, we developed a homodyne AA loop using dither lines technique to hold constant level of squeezing on HD (see chapter 7 for more details) and also a coherent control loop (see chapter 6 for more details) for squeezing measurements on homodyne detector, i.e. a phase-control loop with respect to a local oscillator.

- Finally, we have to implement the automatic-alignment of squeezed vacuum field on interferometer, starting from the misalignment of CC field on Output Mode Cleaner and the relative misalignment between CC field and the ITF detection photodiode beam.

## 3.2 The EPR technique for next generation GW interferometers

An alternative method for the future gravitational wave detectors to achieve a broadband noise reduction below the standard quantum limit is to use a pair of squeezed EPR entangled beams to produce frequency-dependent squeezing by a non-degenerate OPO [36].
Simulated sensitivity curve of Advanced Virgo with 12 dB of FDS injection via EPR technique is shown in Fig. 3.13.

Fig. 3.14 shows a non-degenerate OPO which produces two quantum entangled beams (signal and idler beams) at frequencies $\omega_s = \omega_0$ and $w_i = \omega_s + \Delta = \omega_0 + \Delta$.

A schematic optical configuration of FDS injection via EPR quantistic en-

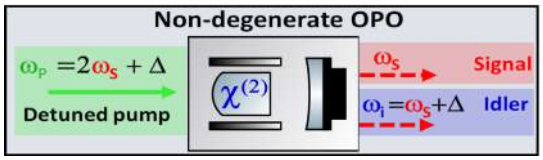


Figure 3.14: A detuned pump in a non-degenerate OPO, which produces signal and idler beams, i.e. two entangled beams (EPR induced squeezing ellipse rotation angle).

tanglement is shown in Fig. 3.15. So, by the parametric down conversion process, squeezed stated are generated, pumping at the pump frequency shifted to $\omega_p = 2\omega_0 + \Delta$, where $\Delta$ is the free spectral range of the interferometer cavity and $\omega_0$ is the carrier frequency of the ITF. Sideband at frequencies $\omega_0$ (lower sideband) and $\omega_0 + \Delta$ (upper sideband) are created and fed into the dark port of the interferometer. Signal and idler beams are separated and filtered by the output mode cleaners (OMC) and each detected via homodyne detector [38]. The two entangled beams are detuned with respect to each other: one has the frequency of the interferometer (signal) and the other (idler) perceives the interferometer like a detuned filter cavity.
Since these beams are entangled, i.e. their noise sidebands are correlated to each other, once one beam is detected, information about the other is obtained as well and vice-versa. Therefore, the interferometer is both the GW detector and the filter cavity, eliminating the need for external cavity. This method, respect to the FC installation, is less expensive, more compact setup and avoids the 1ppm/m round trip losses for the filter cavity, but on the other side two squeezed beams imply double losses and the need for two homodyne detectors [39]. The homodyne measurement conditionally squeezes the input signal in a frequency-dependent way.
The table-top EPR experiment at EGO-Virgo site, that we have developed, will be described in chapter 8.

### 3.2.1 The theory behind quantum noise reduction via EPR entangled beams

Quantum entanglement is a physical phenomenon of a system described in a Hilbert space H consisting of subsystems [40]. If a system is separable, it can be described by the tensor product of the subsystems; if a system is not separable it is called *entangled state*. According to Einstein-Podolsky-Rosen, in the case of perfect entanglement in the quadrature operators of

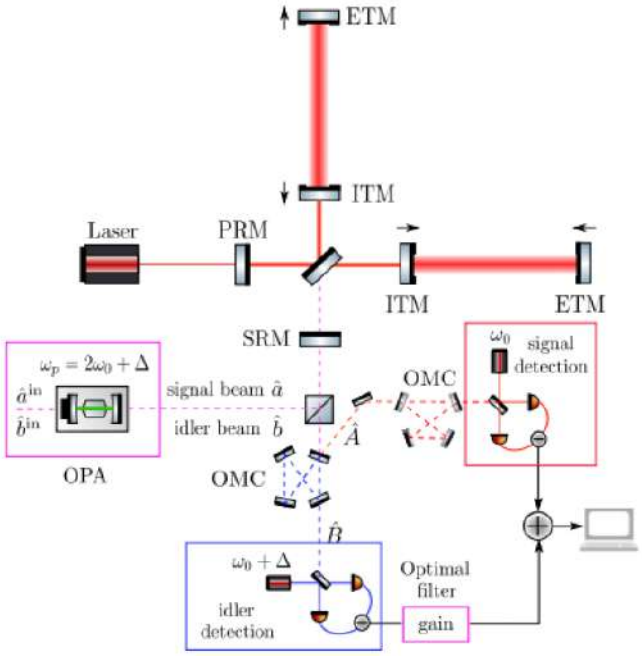


Figure 3.15: Optical configuration of frequency-dependent-squeezing via EPR entangled beams proposed by Ma et al. [38].

two subsystems, there are states such that:

$$\Delta^2(\hat{X}_1 - \hat{X}_2) = 0 \tag{3.1}$$

$$\Delta^2(\hat{Y}_1 + \hat{Y}_2) = 0. \tag{3.2}$$

Consider squeezed states of light at the upper and the lower frequency $\omega_p \pm \Delta\omega$, the variances of the sum of the amplitude operators and the difference of the phase operators depend on the squeeze parameter and they are below the vacuum variance due to their vacuum correlations:

$$\Delta^2(\hat{X}(\omega_p + \Delta\omega) + \hat{X}(\omega_p - \Delta\omega)) = e^{-2r} \leq 1 \tag{3.3}$$

$$\Delta^2(\hat{Y}(\omega_p + \Delta\omega) - \hat{Y}(\omega_p - \Delta\omega)) = e^{-2r} \leq 1. \tag{3.4}$$

Using the two photon-formalism [41], we can derive the EPR entanglement by detuning the OPA [38].
Consider an OPA pumped at $\omega_p$, we can write the linear combination of the upper and the lower sideband fields at $\omega_p/2 \pm \Omega$ respect the quadrature fields $\xi$ around $\omega/2$:

$$\hat{c}_\xi(\Omega) = (e^{-i\xi}\hat{c}_{\omega_p/2+\Omega} + e^{+i\xi}\hat{c}^\dagger_{\omega_p/2-\Omega})/\sqrt{2} \tag{3.5}$$

with $\hat{c}$ and $\hat{c}^\dagger$ the annihilation and creation operators for the optical field at $\omega$, respectively. In addition, we use $\hat{c}_{1,2}$ for $\hat{c}_{0,\pi/2}$ and $\hat{c}_\xi = \hat{c}_1 cos\xi + \hat{c}_2 sin\xi$. Orthogonal quadratures $\hat{c}_\theta$ and $\hat{c}_{\theta+\pi/2}$ have uncorrelated fluctuations and the following spectra (r is the squeeze factor and $\theta$ is the squeeze angle):

$$S_{\hat{c}_\theta \hat{c}_\theta} = e^{-2r} \tag{3.6}$$

$$S_{\hat{c}_{\theta+\pi/2}\hat{c}_{\theta+\pi/2}} = e^{+2r} \tag{3.7}$$

in which the first spectra is suppresed and the second is amplified. Thus, non-linear optics generate entanglement between the upper and the lower sidebands ($\omega_p/2 \pm \Omega$).
Any pair of sideband fields with frequencies $\omega_1$ and $\omega_2$ within the squeeze bandwidth from $\omega_p/2$ satisfying $\omega_1 + \omega_2 = \omega_p$ are entangled. As shown in Fig. 3.16, denoting $\hat{a}_\xi(\Omega)$ the sidebands $\omega_0 \pm \Omega$ and $\hat{b}_\xi(\Omega)$ those around $\omega_0 + \Delta$, in terms of the four fields

$$(\hat{a}_1 \pm \hat{b}_1)/\sqrt{2} \qquad (\hat{a}_2 \pm \hat{b}_2)/\sqrt{2} \tag{3.8}$$

we can write their spectra, which are mutually uncorrelated:

$$S_{\hat{a}_1 \pm \hat{b}_1/\sqrt{2}} = e^{\pm 2r} \tag{3.9}$$

$$S_{\hat{a}_2 \pm \hat{b}_2/\sqrt{2}} = e^{\mp 2r}. \tag{3.10}$$

So, detecting $\hat{b}_\theta = \hat{b}_1 cos\theta + \hat{b}_2 sin\theta$, we can predict $\hat{a}_{-\theta} = \hat{a}_1 cos\theta - \hat{a}_2 sin\theta$, but we don't have informations about $\hat{a}_{\pi/2-\theta}$. In particular, with measurement of the idler quadrature $\hat{b}_\theta$, the signal field will be conditionally squeezed.

Fig. 3.17 shows the dual use of the interferoemetr seen by the signal and idler beams: one resonates and the other is detuned w.r.t the carrier frequency of the interferometer $\omega_0$.
As shown in the conceptual configuration in Fig. 3.14, signal and idler beams go into the interferometer, and then we detect phase quadrature of the out-going beams, named $\hat{A}$ and $\hat{B}$.

1. The out-going signal beam can be written as follows:

$$\hat{A}_2 = e^{2i\beta}(\hat{a}_2 - \mathcal{K}\hat{a}_1) + \sqrt{2\mathcal{K}}e^{i\beta} h/h_{SQL} \tag{3.11}$$

   which consists of shot-noise, radiation-pressure noise and signal, where we denoted $\beta = arctan(\Omega/\gamma)$, with $\gamma$ the bandwidth of the ITF seen by the signal beam and

$$h^2_{SQL} = 8\hbar/(m\Omega^2 L^2), \qquad \mathcal{K} = 2\Theta^3\gamma/[\Omega^2(\Omega^2+\gamma^2)], \qquad \Theta = [8\omega_0 I_c/(mLc)]^{1/3}. \tag{3.12}$$

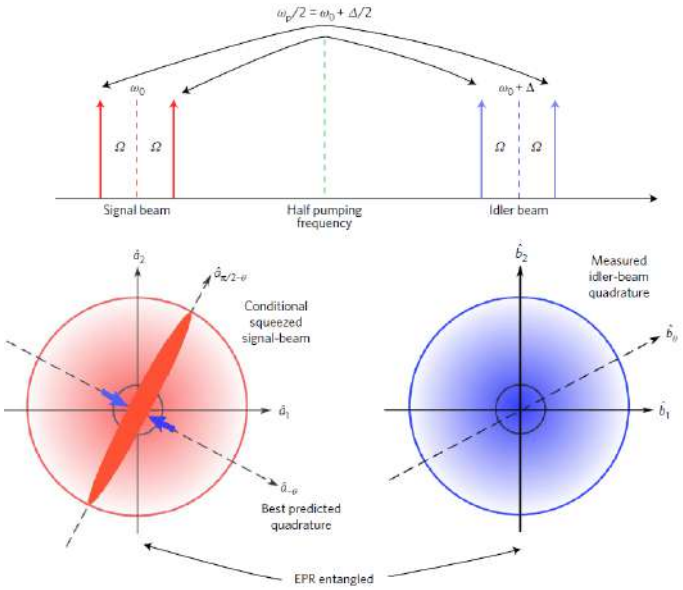


Figure 3.16: EPR-entangled beams from a spectral decomposition point of view (upper panel) and the quantum fluctuations of the signal and idler beams (lower panel) [38].

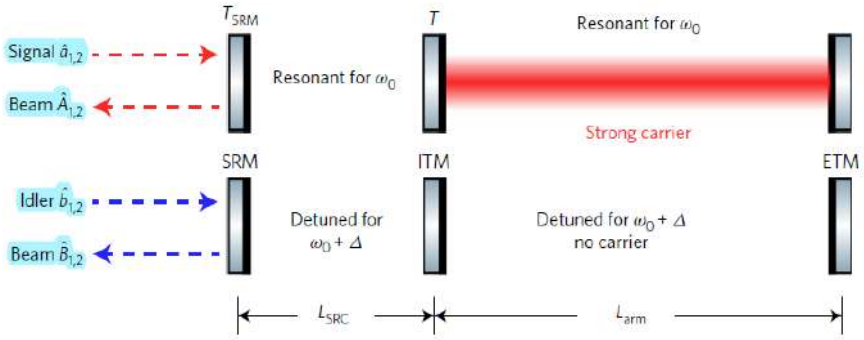


Figure 3.17: The dual use of the interferometer seen by the signal (upper panel) and idler (lower panel) beams [38].

2. Detecting $\hat{B}_2$, the interferometer applies a rotation of $\phi_{rot} = arctan\mathcal{K}$ to the idler beam, so

$$\hat{B}_2 = \hat{b}_{arctan(1/\mathcal{K})} \tag{3.13}$$

that can be realized by adjusting the detuning $\Delta$ and the length of the signal recycling cavity and arm cavity, if $\Theta \ll \gamma$. If a rotation by $\phi_{rot}$ is realized, we will have a noise spectrum of

$$S_h = \frac{h^2_{SQL}}{2cosh(2r)}(\mathcal{K} + \frac{1}{\mathcal{K}}) \tag{3.14}$$

in which conditional squeezing provides a cosh(2r) suppression!

# Chapter 4

# Low-losses Faraday Isolators for frequency-dependent squeezing in AdV+

In this chapter, the low-losses Faraday isolators (FIs) used in the Frequency-Dependent Squeezing (FDS) injection for the Quantum Noise Reduction (QNR) in Advanced Virgo Plus (AdV+) are described.
A low optical losses Faraday Isolator (FI) is fundamental for an efficient squeezed vacuum states injection into the interferometer, since any mismatch with the Interferometer (ITF) mode is equivalent to additional losses.
In general, a Faraday Isolator is used to reduce or eliminate the optical effects of reflections back to the laser to protect it from backscattered light and it consists of an input linear polarizer, a Faraday rotator and another output polarizer.
The low losses FIs that are employed for the Frequency-Dependent-Squeezing (FDS) in AdV+ are those already used for the Frequency-Independent-Squeezing (FIS) injection in 2017, but with some changes in the design, which are fundamental to cope with the requirements of the frequency-dependent squeezing injection.
In the new FIs a great improvement comes from the use of Brewster angle polarizers with the bulk made of Fused Silica (55.4°) and produced by LMA (Laboratoire des Matériaux Avancés), which have smaller absorption and high performing coatings. Other improvements come from the possibility of fine-tuning the position of the TGG (Terbium Gallium Garnet) crystal in the magnetic field to set the correct rotation angle of the polarization to 45° and the possibility to control the temperature of the TGG crystal. Moreover, in order to extract the beam from the FI, an half wave plate (HWP) between the Faraday rotator and the output polarizer has been added.
The single in-air low losses Faraday isolator was installed on the External sQueezing Bench (EQB1) and the double in-vacuum FI were installed on the

Suspended sQueezing Bench (SQB1).
It was necessary to add new FIs because the attenuation factor provided by a single FI was not sufficient.

## 4.1 Single in-air low losses Faraday Isolator

The single in-air low losses Faraday Isolator has an input and output Brewster polarizers (POL11 and POL12) and a TGG crystal (TGG1) inside the Faraday Rotator (FR1). Moreover, as shown in the CAD drawing in Fig. 4.1, it has a zero order HWP placed between the input polarizer and the TGG crystal, in order to keep at the exit of POL12 the same polarization that enters POL11. The squeezing beam coming from the AEI squeezer box (see Fig. 3.4 for the optical design) travels along the EQB1 bench, enters from the POL11 with S-polarization (polarization normal to the optical bench) and exits from POL12 keeping the S-polarization after being rotated twice of 45° by the half-wave plate and the Faraday rotator with TGG1. This con-

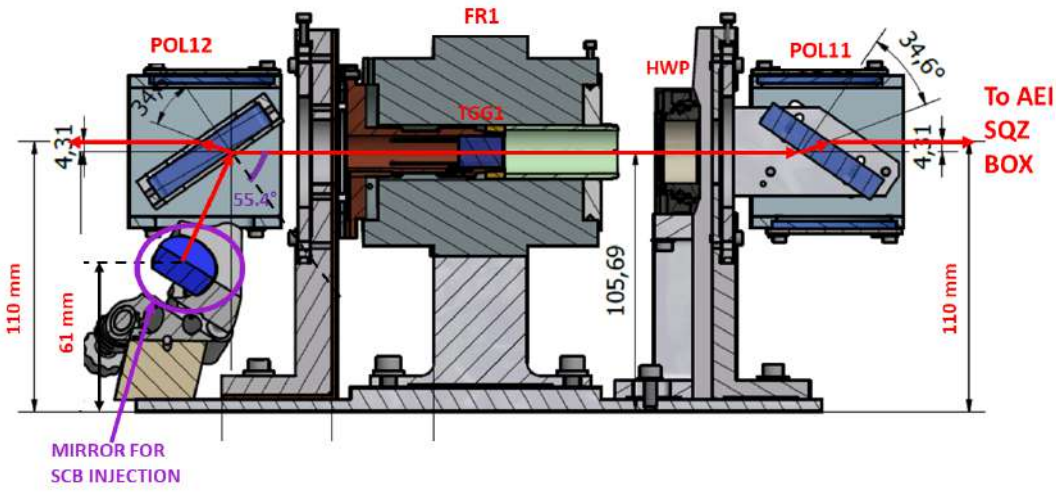


Figure 4.1: CAD drawing: side view of the single in-air low losses FI. The squeezed beam travels from right to left. The Sub-Carrier Beam (SCB) is injected from the mirror at the bottom left and goes towards the AEI squeezer box, then it travels back following the same path of SQZ beam. Credits T. Zelenova

figuration preserves from spurious backscattered light to travel back into the Faraday Isolator along the SQZ beam path till the AEI squeezing vacuum source. Absorption optics, placed on the box around the polarizers supports, allow to damp spurious beams reflected by the Brewster plates surfaces.
The single Faraday isolator have also the function of sending the sub-carrier beam into the AEI squeezer box. In fact, from the polarization point of

view shown in Fig. 4.2, the SCB, that travels at a different height with respect to the squeezing beam, is injected into FI from the bottom of POL12 with a fused silica mirror with P-polarization, and exits from POL11 with S-polarization, in order to enters the OPA in the AEI squeezer box with the correct polarizations. After having travelled inside the AEI box, it goes back into the single FI following the same path of the SQZ beam, so entering from POL11 and exiting S-polarized from POL12, as for the SQZ beam. In fact, the squeezing beam coming from the AEI squeezer box enters from POL11 S-polarized and exits from POL12 of FI with the same polarization. From the CAD drawing, the TGG crystal together with the Faraday rotator (FR1) are slightly tilted of a 1.1° on the horizontal plane, in order to reduce the effect of back reflections inside the TGG1.

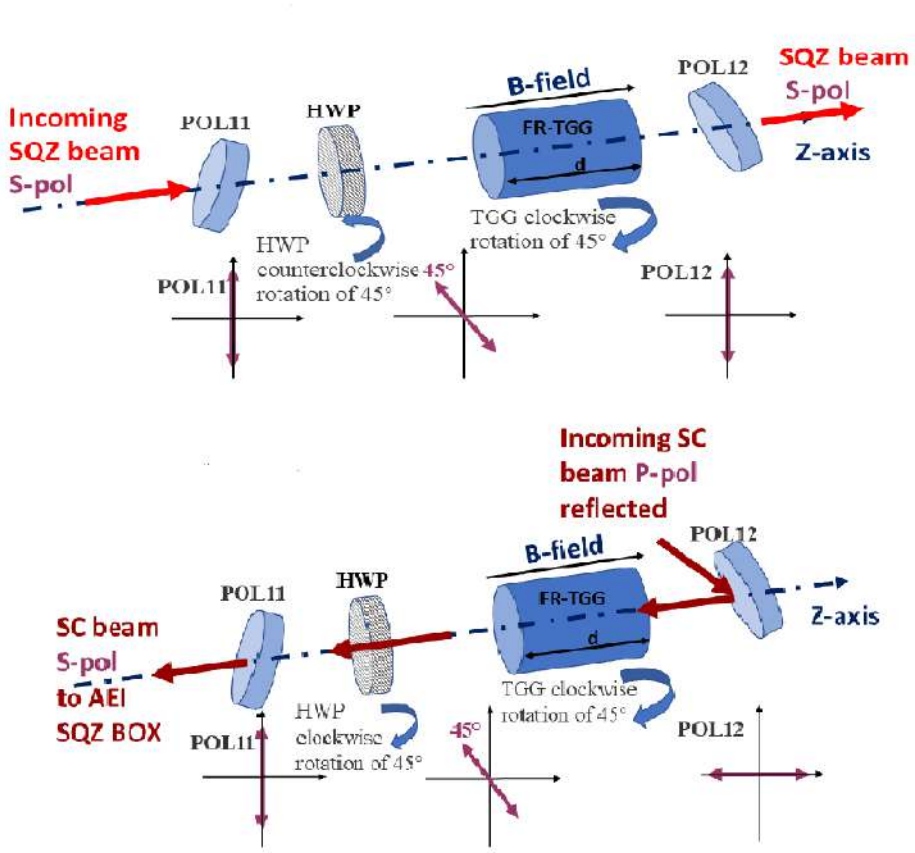


Figure 4.2: Beam polarizations inside the single FI: on the top figure, squeezing beam coming from the AEI squeezer BOX (from the left to the right), while on the bottom, the sub-carrier beam coming from the bottom mirror below POL12 (from the right to the left).

## 4.2 Double in-vacuum low losses Faraday Isolator

The double Faraday isolator is composed by two low-losses Faraday Isolators with a zero order half wave plate (HWP3) between them, installed on the suspended in vacuum squeezing bench. As shown in Fig. 4.3, FI2 has

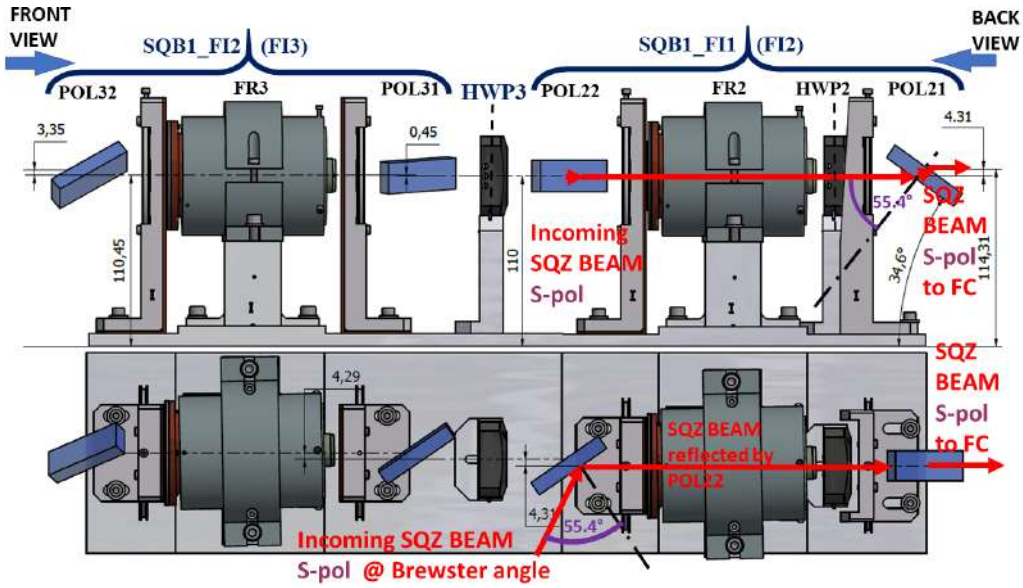


Figure 4.3: CAD drawing: side view (upper figure) and top view (lower figure) of the double FI on suspended in vacuum squeezing bench. Squeezing beam arrives from right side of the output polarizer (POL22) of FI2 and hits the coated surface of POL22 with angle of incidence equal to the Brewster angle of the fused silica (55.4°). The beam is then reflected by POL22, travels inside FI2, and goes towards the filter cavity (FC) with the correct S-polarization. Credits T. Zelenova

the half wave plate (HWP2) inside between the TGG crystal and the input polarizer. The squeezing beam, coming from EQB1 bench, enters the double FI from the right side of the output polarizer (POL22) of FI2, and, travelling inside TGG, HWP2, is transmitted by the input polarizer POL21 and then goes towards the filter cavity (FC).
Once having travelled inside the filter cavity, the SQZ beam travels back towards suspended squeezing bench, meets again the input polarizer POL21 which transmits it, travels inside FI2 and reaches HWP3 (see Fig. 4.3). HWP3 is motorized in order to tune the polarization of the incoming squeezing beam, and it has the main function of selecting between injecting the squeezing beam into the interferometer dark port or sending it towards the homodyne detector on EQB1 bench for diagnostic measurements.
From polarization point of view, squeezing beam enters from POL22 with S-polarization and then, it must go towards the filter cavity with S-polarization.

To maximize the transmitted or reflected beam, the angle of incidence always corresponds to the Brewster angle of fused silica 55.4°.
On the other hand, squeezed beam transmitted by POL32 must have a polarization oriented at 39° to the vertical axis. Another important point to take into account is the beam shifts produced by the optics of the two low-losses Faraday Isolators (see Fig. 4.4).

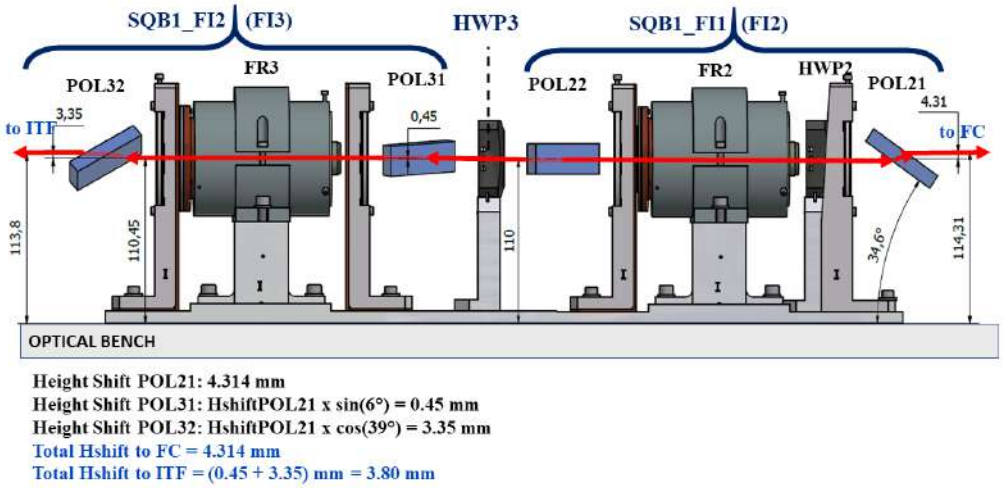


Figure 4.4: CAD drawing of the double FIs from the side: beam height shifts. Credits T. Zelenova

## 4.3 Losses and extiction results

### 4.3.1 Single in-air Faraday Isolators

This section shows the losses and extinction results obtained for the single low-losses Faraday Isolator on EQB1 bench.
Concerning the test and assembly, we aligned the incident beam on single FI for both P and S-polarization through a birefringent crystal of calcite.
Following the same nomenclature shown in Fig. 4.1, the beam hits the POL11 (top coating) at Brewster's angle (55.4 ° for Fused Silica at 1064 nm). With P-polarization, POL11 had losses of less than 0.1 %; with S-polarization, we measured an extinction as follow

$$\epsilon_{dB} = 10log\frac{T_p}{T_s} \tag{4.1}$$

of about 48 dB, where $T_p$ and $T_s$ are the P-polarization and the S-polarizazion transmitted powers, respectively. Then, we have positioned and optimized the position of the TGG crystal (theoretical absorption of TGG = 2400 ppm) inside the rotator until we measured an extinction of about 44 dB (the

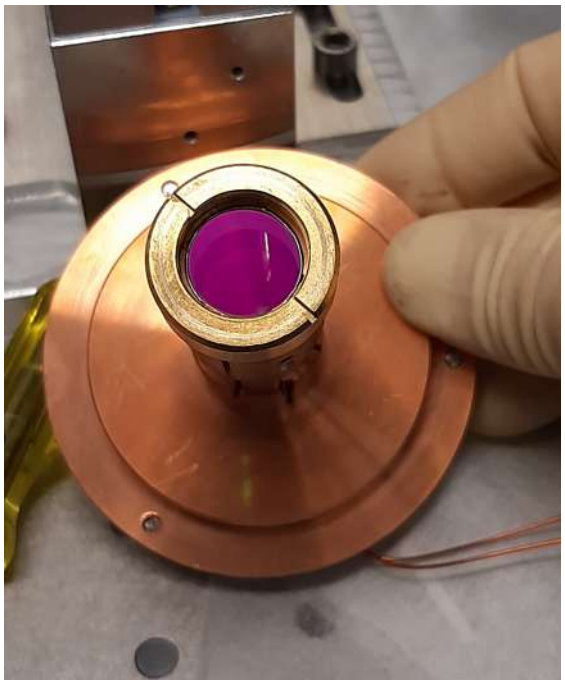

Figure 4.5: TGG crystal and its coating inside the rotator of the single Faraday Isolator.

position of the crystal was fixed through the support of the output polarizer POL12).

Similarly to the polarizer at the input of the rotator, we initially tested only the POL12, obtaining losses of less than 0.1%, and an extinction of about 46 dB. Then, we placed POL12 at the output of the rotator at Brewster's angle (bottom coating) and we positioned the motorized HWP, minimizing its reflections, tuning it so that the POL12 reflections were minimized.
It is important that the Faraday Isolator is well aligned with the incident beam in order to obtain good losses and good extinction.
Overall, FI for EQB1 bench has an extinction of about 40.5 dB and losses due to each optic that makes up the FI around 0.7 %.

### 4.3.2 Double in-vacuum Faraday Isolators

This section shows the losses and extinction results obtained for the double low-losses Faraday Isolator on SQB1 bench.
Following the same procedure used for the assembly of the single FI, we have assembled and tested each component starting from POL21 (the same nomenclature as shown in Fig. 4.3 or 4.4).
First of all, each component was ultrasonically cleaned to then be installed in a vacuum. For each polarizer mounted we measured the losses and ex-

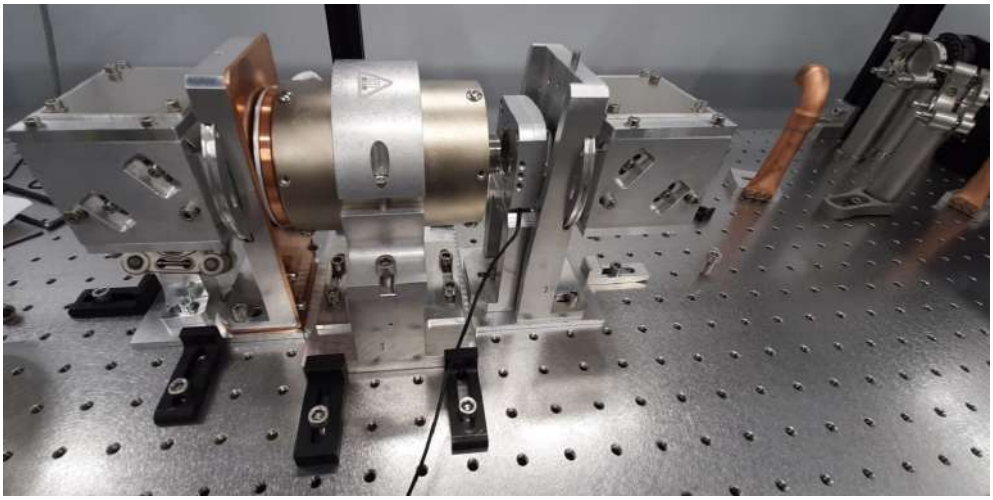

Figure 4.6: Single low-losses Faraday Isolator view from the side on EQB1 bench.

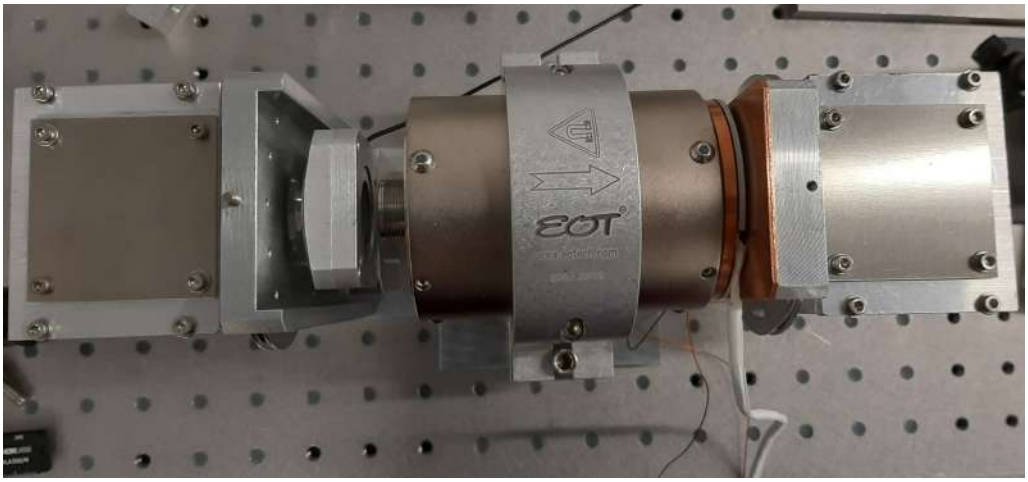


Figure 4.7: Single low-losses Faraday Isolator view from the top on EQB1 bench.

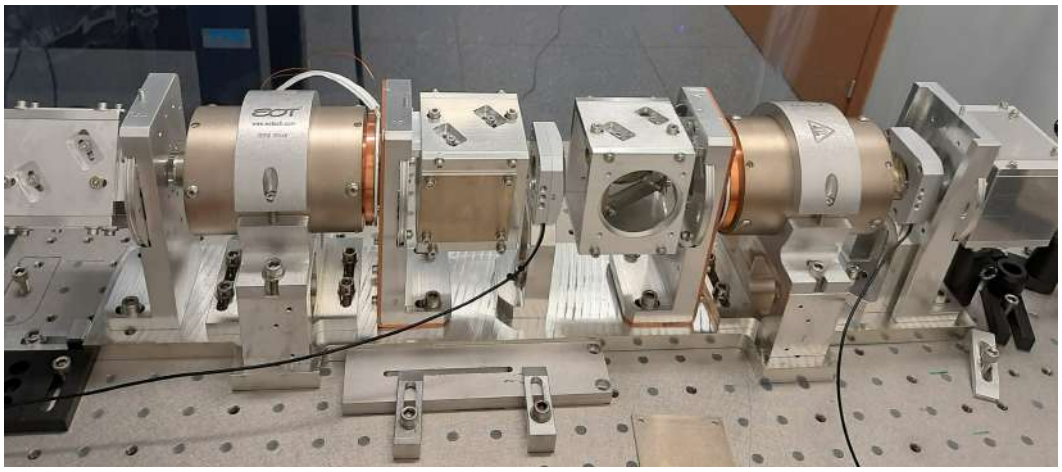

Figure 4.8: Double low-losses FI view from the side.

tinction.
The beam hits the POL21 (bottom coating) and POL22 at Brewster's angle (55.4 ° for Fused Silica at 1064 nm). Then, we placed POL32 with P-polarization at 39° and POL31 with P-polarization at 6°. So, we aligned the incident beam with double FI for both P and S-polarizations through a birefringent crystal of calcite, obtaining losses shown in the following table.

| Double FI polarizers | Losses [%] |
|---|---|
| POL21 | 0.06 |
| POL22 | 0.07 |
| POL31 | 0.04 |
| POL32 | 0.04 |

Table 4.1: Measurements of losses for each double Faraday Isolator polarizers.

In addition, we were also able to optimize the position of the TGGs inside the rotators by using 6 screws in the support of POL22 and POL31, which allow to uniformly compress the copper support to the TGGs. It is also important to minimize the reflection of the TGGs.
The HWPs allow to extinguish their reflection by tilting them, in this way we have optimized the losses induced by them. HWP3 discriminate to send the beam either to the interferometer at 53° or to the homodyne detector on the external bench at 7°.

Moreover, fine-tuning the orientation of POL32 and POL31 by reducing losses and to check their orientation, we measured the angles of the beam reflected by POL31 towards the homodyne detector. So, we obtained a 90°+20.67° = 110.67° for the side reflection and 6.14° for the vertical inclination. These results are in agreement with expectation, which are

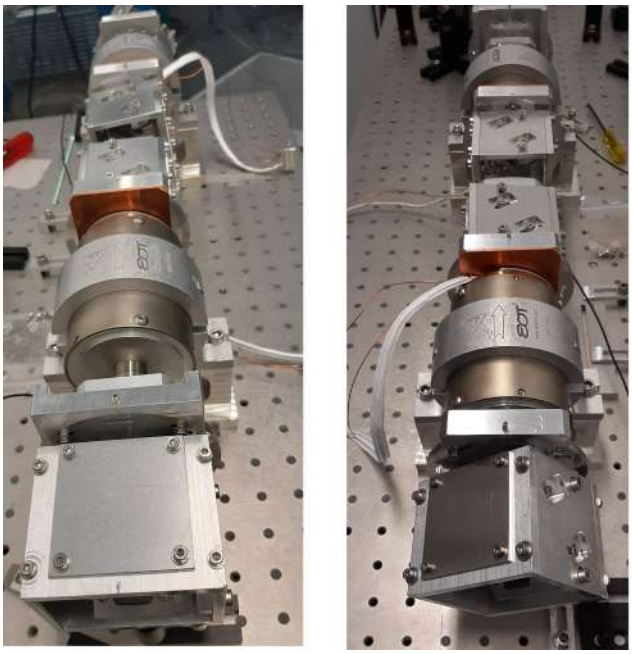

Figure 4.9: Double low-losses FI view from the top side from POL21 (on the left) and from POL31 (on the right).

2*Brewster's angle (55.4°) = 110.8° for the side reflection and 6° for the vertical inclination.
Finally, we placed a mirror at the output of the double FI in order to measure the extinction reflecting the beam back, obtaining about 45.3 dB (the returning beam is extinguished mainly by the reflection of POL31).
As a further verification of the losses induced by the double Faraday isolator, we fixed the power meter in a remote position and we measured the power with and without the double FI obtaining losses of about 1%.

# Chapter 5

# Acousto-optical-modulator test

An Acousto-Optic-Modulator (AOM) is an optical component based on the phonon-photon interaction, that allows to modulate the frequency and direction of a laser beam, i.e. spatially and spectrally shifting the beam [42]. In this chapter, the AOM test in double-pass configuration performed in Genoa Laboratory and the AOM installation for Advanced Virgo Plus squeezing system are described.

## 5.1 AOM double-pass configuration test in Genoa Laboratory

The single-pass configuration, in which the laser beam crosses the AOM only once, was previously tested in Genoa Laboratory (for more details see my Master's Thesis [43]).
In order to test the AOM in double-pass configuration [44], in which the AOM is crossed twice, we have previously characterized the laser beam (a 50 mW fiber optic laser diode DBR1064P at central wavelength of 1064 nm) to get the gaussian waist position in which to place the AOM device. In Fig. 5.1 the fit of the Gaussian beam waist as function of the position is shown, using the following formula:

$$w(z) = w_0 \sqrt{1 + (\frac{\lambda(z - z_0)}{\pi \omega_0^2})^2} \tag{5.1}$$

with $\lambda = 1064$ nm the laser wavelength. From this analysis, we obtained the waist size $\omega_0 = (0.081 \pm 0.001)$ mm and the waist position $z0 = (126.7 \pm 2)$ mm.

Once placed the AOM in $z_0$, we sent different RF frequencies signals to maximize the power of the diffracted beam, as shown in Fig. 5.2. In fact, when a RF signal at frequency $\Omega$ is fed into the AOM crystal, it causes a travelling density wave to form, which propagates at the speed of sound $v_s$

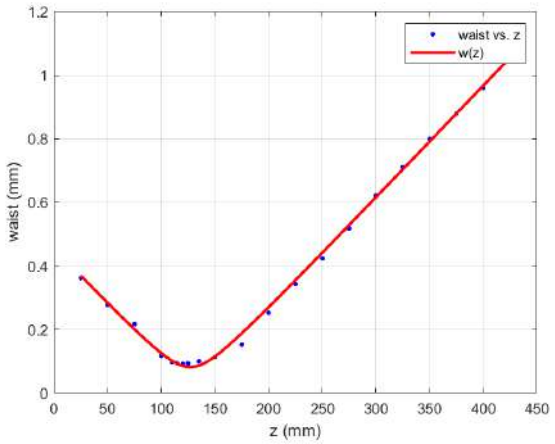


Figure 5.1: Fit waist of the Gaussian beam as function of position z along the beam propagation direction using a laser beam profiler.

at frequency $\Omega$, thus the crystal acts like a diffraction grating (like a Bragg cell) [45]. As shown in Fig. 5.4, defining the diffraction angle as $\Theta = 2\theta$, the light will scatter into an angle of m$\Theta$, which, in terms of phonons, means to absorb or destroy m phonons. In particular, the incident light will change as follows:

$$f \rightarrow f + mf_{RF} \tag{5.2}$$

where m is the order of diffraction and if it is less than 0, m phonons are created.
In our configuration, an acoustic wave is generated via ADF4351 integrated voltage controlled oscillator (VCO) that interacts with incident light generating diffracted laser beams (AOM model 3200-1113 from Gooch and Housego [42]).
The first-order and the second-order of the diffracted beam on a infrared card are shown in Fig. 5.3. The results obtained will be related to the first-order.

Fig. 5.5 and 5.6 show the double-pass configuration setup in Genoa laboratory.
Since AOM device is responsive only to S-polarized light, a Polarizing Beam Splitter (PBS) is added to divide the laser beam into its P and S-polarization contributions.
Following the reflection beam path from the PBS, a focal lenses is added to make the beam width smaller than the AOM input window (2.54 mm).
Installing a Quarter-Wave Plate (QWP) to rotate into circular the polarization before the AOM, we have lower diffraction efficiency, higher frequency shift compared to placing QWP after the AOM which would produce an higher diffraction efficiency but lower frequency shift. To verify that we have circular and non-elliptic polarization after QWP, we have equalized the

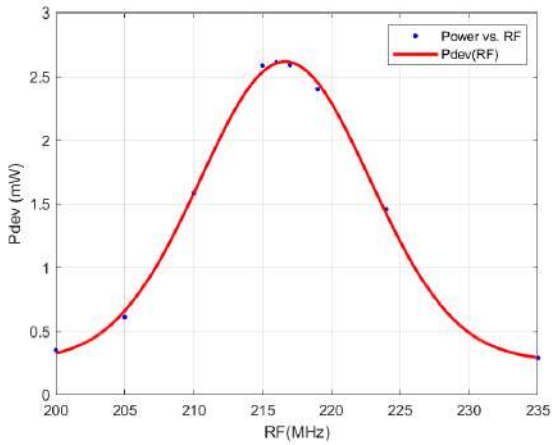


Figure 5.2: Powers of diffracted beam ($P_{dev}$) measured with a power meter vs RF signals sent to the AOM device.

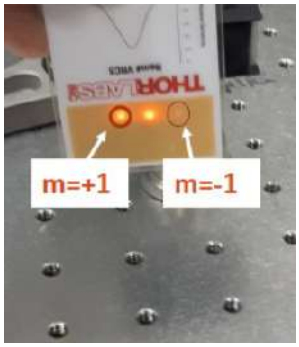


Figure 5.3: On the left of the IR card, the first-order of the diffracted beam (m=+1), on the center the main beam (m=0) and on the right the second-order (m=-1).

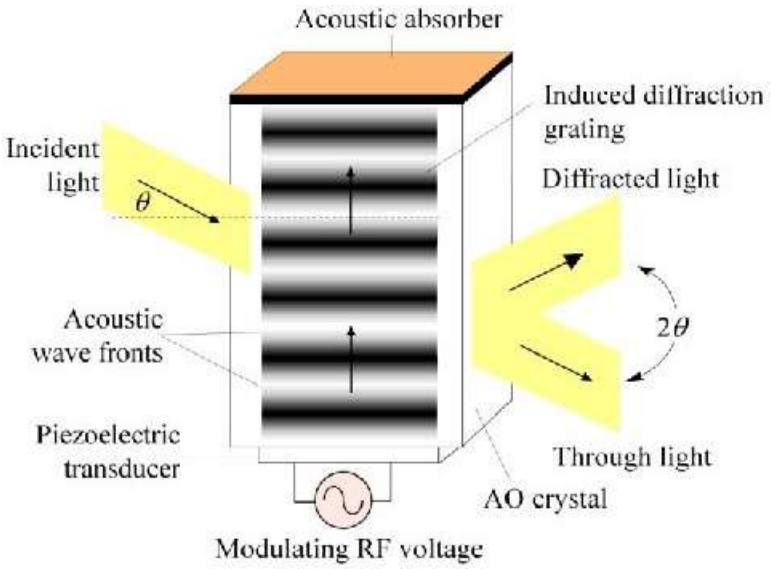


Figure 5.4: Schematic operation of an AOM, which has to be tilted about $\theta$ with respect to the input laser beam.

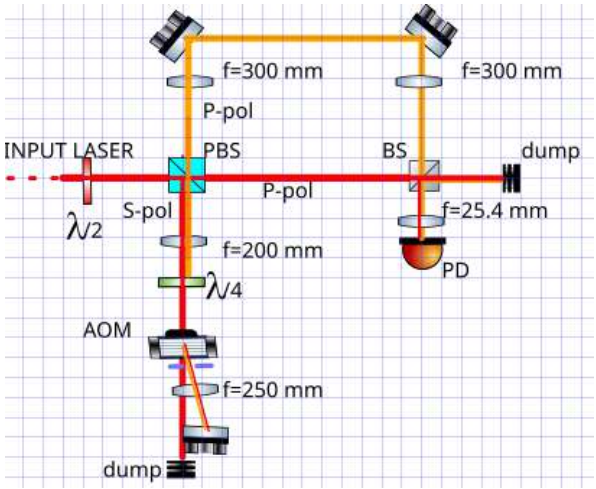


Figure 5.5: Double-pass setup of AOM test in Genoa laboratory (not the real distances). Red beam is the main beam, orange beam is the diffracted beam.

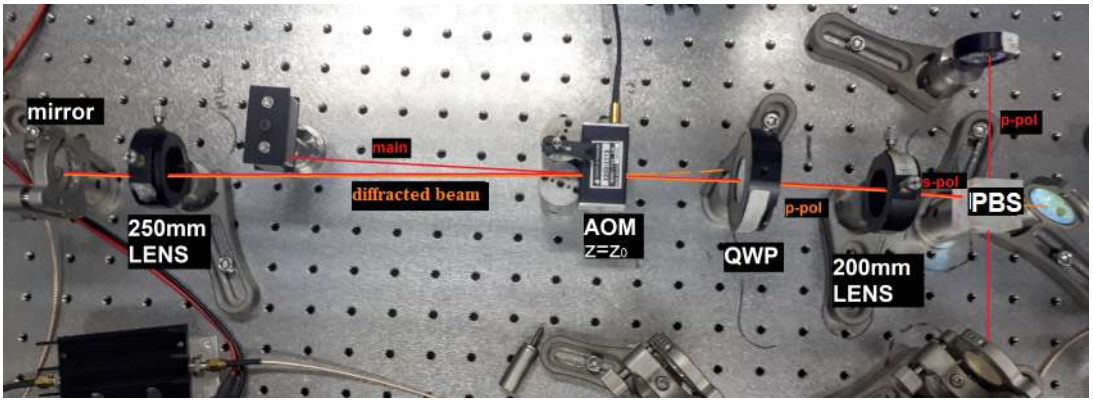


Figure 5.6: Optical setup for the beating in the double-pass configuration at Genoa laboratory.

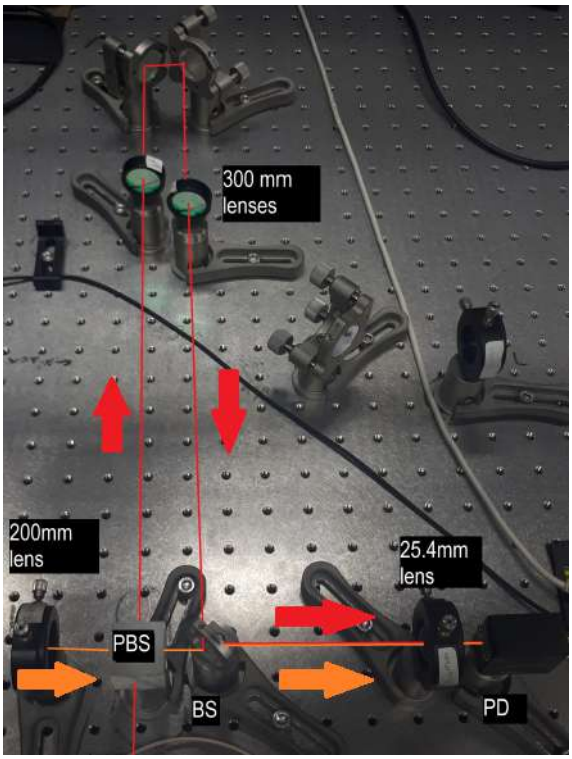


Figure 5.7: Double-pass setup of AOM test in Genoa laboratory. Red beam is the main beam, orange beam is the diffracted beam.

power of the S and P-polarization contributions by means of a HWP.
Since for a typical acousto-optic diffraction the small-angle approximation holds, i.e. $\sin\theta \sim \theta$, the diffraction angle (also called Bragg angle) for a single-pass through the AOM is calculated as follows:

$$\theta = \frac{\lambda f_{RF}}{2v_s} = 27.4 \quad mrad, \tag{5.3}$$

with $f_{RF} = 216.4$ MHz the frequency of the RF signal that maximizes the diffraction efficiency, as shown in Fig. 5.2, and $v_s = 4.2 * 10^6$ mm/s the acoustic sound in the material.
Then, following the beam path in Fig. 5.5, the S-polarized beam enters the AOM which causes diffraction and the diffracted beam (the orange beam in figure) is sent back into the AOM, therefore another diffraction occurs (the twice frequency-shifted beam). When the diffracted beam passes the QWP again, it is turned into P-polarization in order to record the beatnote with a Photodiode (PD) using a spectrum analyzer. In order to do that, we superposed the main and the diffracted beam on the PD, maximizing the beatnote signal at $2f_{RF} = 432$ MHz.

### 5.1.1 Diffraction efficiency results

In order to compute the AOM diffraction efficiency, we measured the power before it entered the AOM $P_{main}$ and the power of the diffracted beam $P_{single}$ (see Fig. 5.6) with a power meter and we calculated the single efficiency as follows:

$$\epsilon_{single} = \frac{P_{single}}{P_{main}} * 100 = 37\%. \tag{5.4}$$

The double efficiency can be estimate measuring the power of the diffracted beam after being reflected by the mirror $P_{double}$, passed back into the AOM (twice) and transmitted by the PBS:

$$\epsilon_{double} = \frac{P_{double}}{P_{main}} * 100 = 7\%. \tag{5.5}$$

It is important to emphasize that these diffraction efficiency estimates depend on the transmission efficiency of the AOM, in which we lost about 1.5% in power transmission (measuring the power beam before and after the AOM without the RF signal), due to the small aperture of the AOM and also consider the losses due to the PBS (S-polarized beam residual). To solve the problem of losses in the AOM test, it would be better to place it on a micrometric slide, so as to tilt the AOM and not cut the beam and also to use super-polished optics, as was done for AdV+ squeezing system.

## 5.2 AOM installation for Advanced Virgo Plus

The Acousto-Optic Modulator (AOM) is needed in AdV+ squeezing system to slightly shift the green beam resonance inside the filter cavity, allowing the simultaneous resonance of the infrared beams, and to slightly detune the IR resonance allowing the rotation of the squeezed light (FDS). For more details on it, see section 3.1.1.
Thus, in Advanced Virgo Plus, an AOM was installed in the double-pass configuration with the 80 MHz RF generator.

The procedure to test and installed the AOM is the same used in Genoa

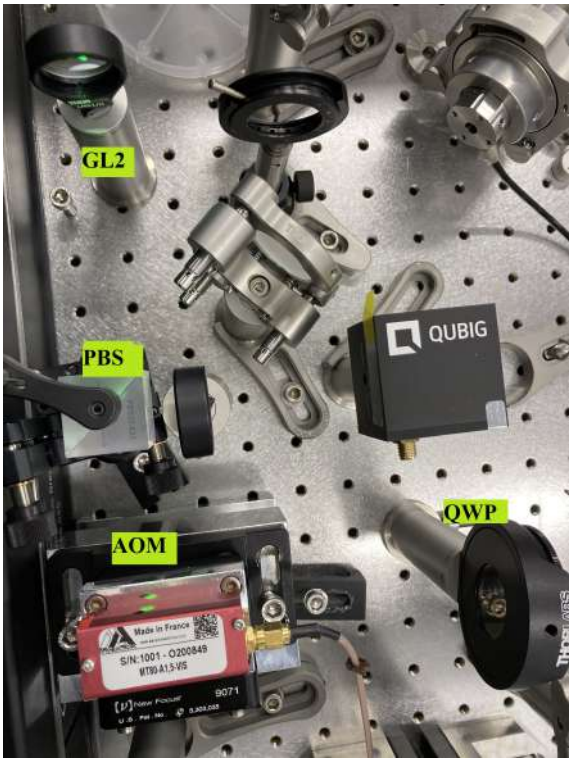


Figure 5.8: The Acousto-Optic Modulator installed on EQB1 bench for AdV+ squeezing system.

Laboratory. As shown in Fig. 5.8, a telescope (GL) with super-polished lenses is installed before the AOM in order to reduce beam size at AOM input. Before entering the AOM, the beam passes through, again, an HWP and a PBS and then it is diffracted with more then five higher orders and frequency shifted beams emerge with the main (zero order) not deviated. An iris selects again the first diffracted order. After a QWP, it is retroreflected into the AOM with orthogonal polarizaton, so that is then reflected by the PBS towards the filter cavity.

### 5.2.1 Diffraction efficiency results

First of all, we maximized the power of the diffracted beam, so the single-pass diffraction efficiency vs driving DC voltage, as shown in Fig. 5.9. In fact, the AOM driver has a trimmer to change the RF power level.

Then, in order to estimate the diffraction efficiency, we measured the power

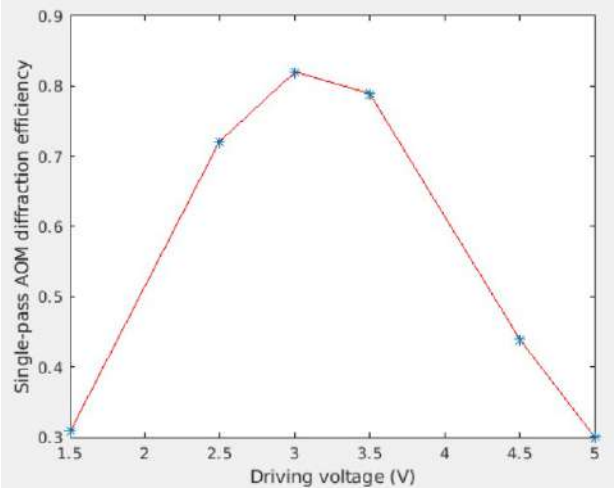


Figure 5.9: The measured single-pass diffraction efficiency vs driving DC voltage.

beam $P_{inc}$ before entering the AOM, the power beam $P_{single}$ after the single-pass (first-order) and then the power beam $P_{double}$ retroreflected into the AOM after the reflection by the PBS. The estimate of the diffraction efficiency in the two cases is as follows:

$$\epsilon_{single} = \frac{P_{single}}{P_{inc}} * 100 = 85\% \tag{5.6}$$

$$\epsilon_{double} = \frac{P_{double}}{P_{inc}} * 100 = 34\%. \tag{5.7}$$

Note that we obtained better results than the test in the Genoa lab, because we used super-polished optics for the AdV+ experiment and we placed the AOM device on a micrometric slide.

# Chapter 6

# Controls development for AdV+

For audio-band squeezed vacuum field measurements is required a phase-control loop with respect to a reference beam (local oscillator) [46]. The coherent control (CC) loop is a two-actuators loop: the first is in the optical path of the green beam and stabilizes the phase of the squeezing ellipse that is generated by the OPO; the second is at detector level (interferometer or homodyne detector) and is used to fix the phase with the local oscillator (LO).
In this chapter, the implementation of coherent control loop at homodyne detector level in Quantum Noise Reduction system for Advanced Virgo Plus is described.

## 6.1 Elements of Control Systems and Transfer Function definition

In this section, a general control system scheme will be explained in order to understand better the development of the CC loop in Advanced Virgo Plus detector [47].
A Control System is an ensemble of interconnected components designed to achieve a desired purpose.
Let's define all the elements of a control system following the scheme shown in Fig. 6.2:

- setpoint is the desired value of your system;
- input filter is a transducer from physical quantity to electrical signal;
- summation point allows you to compare between setpoint and measurement;
- error signal is a quantity that must be kept to zero;

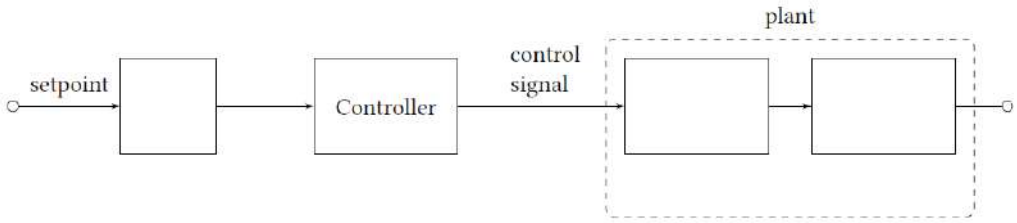


Figure 6.1: Open loop control system.

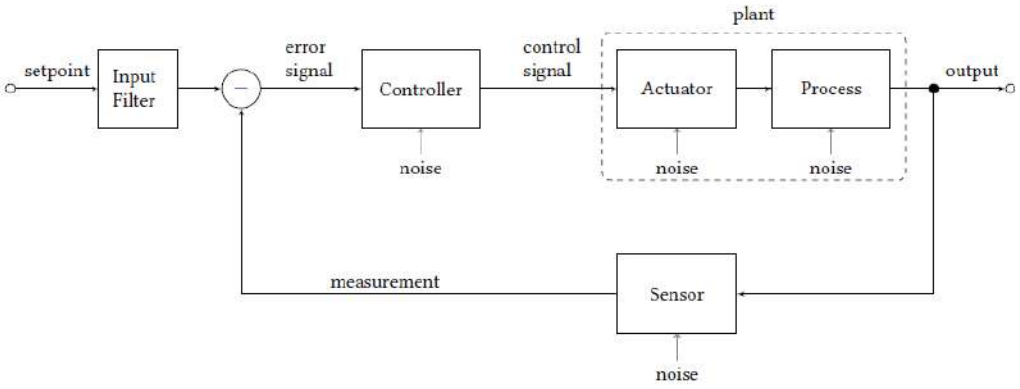


Figure 6.2: Closed loop control system.

- controller is a physical/software equipment which determines how to achieve the setpoint;
- control signal is the output of controller which is sent to the machinery which actually drives the system;
- plant is the physical system of interest, composed by actuators, i.e. the equipment which changes the Plant's behaviour according to the designer's desire, and the physical process one is interested in;
- then we have the output, i.e. the outcome of the control chain;
- sensor is the equipment which reads the physical variable to be controlled;
- measurement, i.e. the physical variable to be controlled, after a possible conversion to electrical signal;
- moreover, we have the presence of noises, i.e. the cause of disturbances in the system. In particular, following the scheme, we have:
    - the control noise which is an imperfect output of the controller (digital/numerical noise, mistuned gain, badly placed poles/zeros, etc..);

- the actuator noise, which is an imperfect conversion from signal to real output (DAC noise, etc..);
- the process noises, i.e. all kind of disturbances in the physical process (fabrication defects, mechanical faults, external environment, etc..);
- the sensor noises, which is an imperfect reading of the physical variable (sensor calibration, working conditions, environmental couplings, shot noise, ADC noise, electronic/dark noise, etc..).

Let's consider the most common kind of system, because most of the dynamic systems of interest are described by constant-coefficient linear differential equations: SISO LTI Systems, i.e. Single Input Single Output Linear Time Invariant Systems. From the properties of LTI systems, a linear system response obeys the principle of superposition (i.e. if a system has an input which is expressed as a sum of signals, then the response of the system is the sum of the individual responses to the respective signals) and the response of a LTI system can be expressed as the convolution of the input with the unit impulse response of the system.
Paul Dirac's impulse response is a very intense but very short forces that can be described by the mathematical impulse, as follows:

$$\delta(t) = 0, t \neq 0 \tag{6.1}$$

$$\int_{-\infty}^{+\infty} \delta(t)dt = 1 \tag{6.2}$$

and for the principle of superposition, the response y(t) of a continuous input u(t) can be described as the sum of the responses of impulses h($\tau_i$), i.e. the convolution integral:

$$y(t) = \int_{-\infty}^{+\infty} h(\tau)u(t-\tau)d\tau. \tag{6.3}$$

Assuming the input as $u(t) = e^{st}$, where $s = \sigma + i\omega$ complex, the output will be the Laplace Transform of the unit impulse response h (t), as follows:

$$H(s) = \int_{0}^{+\infty} h(\tau)e^{-s\tau}d\tau. \tag{6.4}$$

So, the ratio between the Laplace Transforms of the output and the input is the Transfer Function of the system, i.e. the transfer gain from input to output:

$$H(s) = \frac{Y(s)}{U(s)} \tag{6.5}$$

and for the LTI systems is better to find their frequency response $H(j\omega)$, which is a complex number that can be represented with a Bode Diagram, which shows as a function of the frequency both the magnitude M and the phase $\varphi$

$$M = |H(j\omega)| \tag{6.6}$$

$$\varphi = \angle H(j\omega). \tag{6.7}$$

Since differentiation and integration in time domain become multiplication and division in Laplace's domain, we can describe a controller or a component as a rational function, which is much easier to handle:

$$F(s) = K\frac{\prod_{i=1}^{m}(s - z_i)}{\prod_{i=1}^{n}(s - p_i)}, \tag{6.8}$$

where $z_i$ are the zeros of the system and $p_i$ are the poles of the system.
So, designing a controller, i.e. a loop filter, means designing the controller's transfer function in order to have the global transfer function of the system (the Closed Loop Transfer Function) with the requirement of stability, tracking, regulation, robustness. In order to do so, the loop filter's transfer function must compensate the structures which are present in the actual system, depicted as poles and zeros, with its own poles and zeros, which have to be placed in a sensible way.
Finally, we can define the Closed Loop Transfer Function (CLTF) as the overall transfer function from output to input

$$CLTF = \frac{G(s)}{1 + G(s) * H(s)} \tag{6.9}$$

and the Open-Loop Transfer Function (OLTF) as the transfer function without the feedback path

$$OLTF = G(s) * H(s) \tag{6.10}$$

where G(s) is the plant in a simplified loop diagram. The OLTF is important for the stability of the loop.

## 6.2 Coherent control loop for AdV+

In AdV+'s squeezing system the CC loop is needed to stabilize the relative phase between LO and CC beams.
In this section, coherent control loop on the homodyne detector will be explained (see section 3.1 for more details on AdV+ squeezing system).
As shown in Fig. 6.3, with a delay line on a removable optical sled, we can

choose whether to send the squeezing and CC beams on suspended benches or directly on homodyne detector. In fact, we have three ways to measure squeezing on the homodyne detector: with the delay line (the beam never leaves EQB1 bench); with the retroreflector (the beam arrives on SQB1 bench and goes back towards EQB1 bench); with the filter cavity input mirror. In the second and third configuration we can choose whether to use homodyne or to go towards interferometer using a HWP on SQB1 bench. The delay line is used to mimic the distance between the last mirror of EQB1 bench and the retroreflector on SQB1 bench (round trip) in order to superimposed SQZ and CC beams with the LO beam. Moreover, the delay line allowed us to do the pre-commissioning of EQB1 bench in stand alone with respect to the rest of QNR (Quantum Noise Reduction) system and to decouple the losses and phase noise present only on EQB1.

Concerning the sensor of the CC loop, we used the homodyne photodiodes

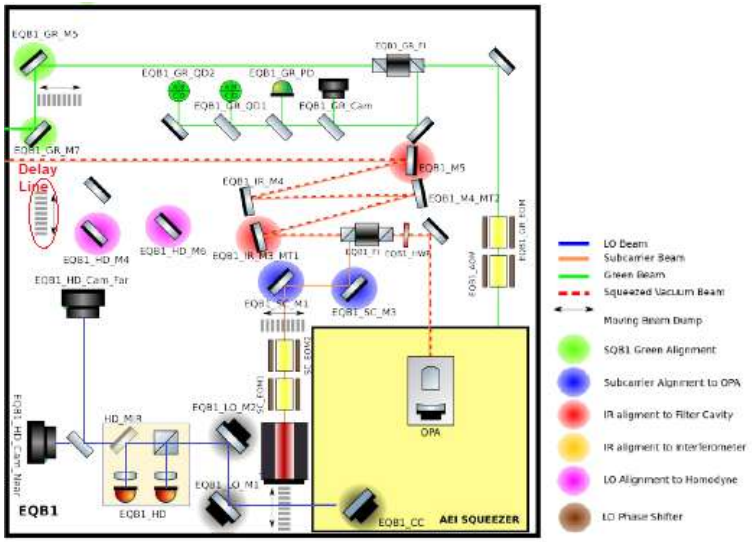


Figure 6.3: Optical setup of the External sQueezing Bench (EQB1) in Advanced Virgo Plus squeezing system. A motorized delay line allows the squeezing beam (red dotted line) to be sent to the homodyne and not to the suspended benches, so as to superimpose it on the local oscillator (blue line) for diagnostic measurements.

(PDs) because they contain the information of the phase difference between the two fields that we want to fix. These two PDs are demodulated at the frequency difference between LO and CC beams, i.e. 4.006 MHz (digital demodulation).

Our squeezing system consists of one in-air external bench and two suspended benches, this implies that the relative fluctuations between the benches are very large. For this reason, we need a loop with a large bandwidth and a

large range and to do that we decided to use a fast loop with little range nested with a loop with a large range and little bandwidth. So, as actuators of the CC loop, we initially used the two actuators on the LO path shown in Fig. 6.3, i.e. LO_M2 (in front of the homodyne detector) that is a tri-axial actuator with 30um of travel range, and LO_M1 (in front of the AEI squeezer) that is a phase shifter with 3um of travel range.

### 6.2.1 Mathematical point of view: Coherent control field at homodyne detector

In this section, the magnitude of the beatnote calculation between LO and CC fields at homodyne detector level is derived [48].
In the AEI squeezer box (see section 3.1.1), the CC laser provides the CC field that is sent to the OPA. So, we can write the CC field, the pump field inside the OPA and the local oscillator field as follows:

$$E_{CC}(t) = \alpha cos(\omega_0 t + \gamma + \Omega) \tag{6.11}$$

$$E_p(t) = \beta cos(2\omega_0 t + \phi) \tag{6.12}$$

$$E_{LO}(t) = \Gamma cos(\omega_0 t) \tag{6.13}$$

in which $\omega_0$ is the carrier frequency, $\gamma$ the relative phase between CC and LO fields, $\phi$ is controlled by the pump phase CC loop. The nonlinear interaction inside the OPA generates a second sideband at frequency $-\Omega$. The control of the quadrature angle of the squeezed vacuum with respect to a local oscillator is achieved by the quadrature control field, that is frequency shifted against the vacuum squeezed mode. According to simplification explained in [49], the quadrature control field, i.e. the coherent control field, at the OPA output becomes:

$$E_{CC}(t) \propto \frac{1+g}{\sqrt{2g}} cos(\omega_0 t + \gamma + \Omega t) - \frac{1-g}{\sqrt{2g}} cos(\omega_0 t + \gamma - \Omega t - 2\phi) \tag{6.14}$$

where g is the OPA parametric gain. This expression represents the parametrically amplified coherent control field. This field produces a beatnote B(t) at frequency $\Omega$ with the local oscillator field at the homodyne detector, as follows:

$$B(t) \propto (1+g)cos(\Omega t + \gamma) - (1-g)cos(-\Omega t + \gamma - 2\phi). \tag{6.15}$$

Moreover, we can write the beatnote as the sum of an in-phase term $B_i$ and a quadrature term $B_q$:

$$B(t) \propto B_i sin(\Omega t) + B_q cos(\Omega t) \tag{6.16}$$

in which the in-phase term and the quadrature term can be written as follows

$$B_i = -(1+g)sin(\gamma) - (1-g)sin(\gamma - 2\phi) \tag{6.17}$$
$$B_q = (1+g)cos(\gamma) - (1-g)cos(\gamma - 2\phi). \tag{6.18}$$

Concerning the CC phase after demodulation at $\Omega$, $\phi_{meas}$ is given by the arctan of the ratio of the in-phase and the quadrature terms, as follows:

$$\phi_{meas} = arctan(\frac{-(1+g)sin(\gamma) - (1-g)sin(\gamma - 2\phi)}{(1+g)cos(\gamma) - (1-g)cos(\gamma - 2\phi)}) \tag{6.19}$$

in which the relation between the relative phase $\gamma$ and the measured phase $\phi_{meas}$ is not linear, unless the OPA non-linear interaction is negligible, i.e. g=1.
Instead, the magnitude of the beatnote is given by the quadrature sum of the in-phase and quadrature terms, as follows:

$$mag = \sqrt{B_i^2 + B_q^2} \propto \sqrt{2[1 + g^2 - (1-g^2)cos(2\gamma - 2\phi)]} \tag{6.20}$$

in which it oscillates with the phase difference $(2\gamma - 2\phi)$. Moreover, the parametric gain g can be obtained by the ratio of maximum and minimum magnitude.

### 6.2.2 Scheme of CC loop

The idea of the CC loop is to stabilize the relative phase between LO and CC beams and, knowing their phase difference via the demodulated RF difference of the two HD photodiodes, it actuates on the PZT to actively change the optical path length of LO beam so that the phase difference with CC beam is constant.
The CC loop with a single actuator works well if we close it only on EQB1 bench (put the delay line). However when we remove the delay line and send the beam towards the suspended benches, the optical path differences between LO and SQZ beams oscillate much more and the range of only one actuator is no longer sufficient. So, we need a second actuator that allows us to make a second loop with lower bandwidth but greater range. The purpose of this second loop is to keep the actuator of the first loop in the middle of its dynamic range.
In fact, we have developed two loops, one using the phase shifter to close the loop with high UGF (Unity Gain Frequency, which supplies the bandwidth of the loop), named "fast CC Loop" and the other using the triaxial actuator to have a long term stability, named "coarse CC loop".
The scheme of the fast CC loop is shown in Fig. 6.4. The error signal is the demodulated signal from HD I quadrature, in which we have the possibility to add noises (line, colored, white noise..) to make for example transfer

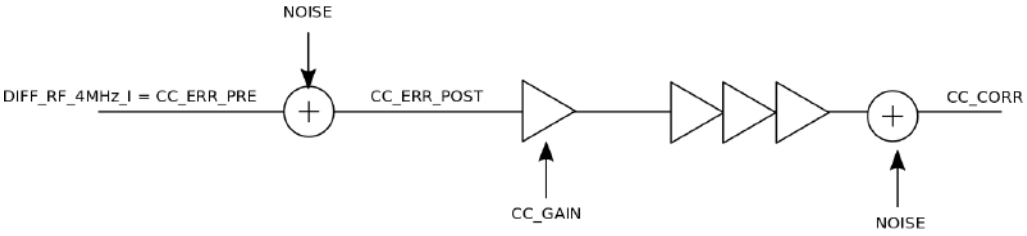


Figure 6.4: Fast coherent control loop scheme.

Figure 6.5: Piezo holder for fast CC loop. It is symmetrical and hosts two mirrors and two piezos. The idea is to push simultaneously the mount from both the side in order to mechanically dump the resonances.

function. Then, we have the gain, to open/close the CC loop, the control filters, so we have the correction to send to the piezo (shown in Fig. 6.5).

The scheme of the coarse CC loop is shown in Fig. 6.6. First of all, a "switch" allows you to choose between two different error signals: one is the same error signal of the fast CC loop (DIFF_RF_4MHz_I), and the other is the correction of the fast loop signal (CC_CORR).
Following the scheme, we have the possibility to add setpoints, then we have the gain and we can open and close the loop with an enable, then the possibility to add noise in order to measure transfer function of the system, the filters and some triggers for automatic relay loop or for reset it (for example if the correction signal of the fast CC is bigger than his dynamical

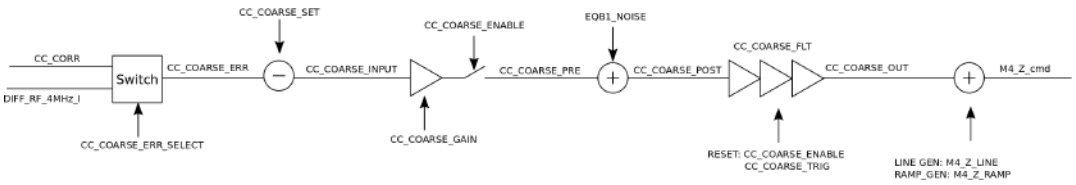


Figure 6.6: Coarse coherent control loop scheme.

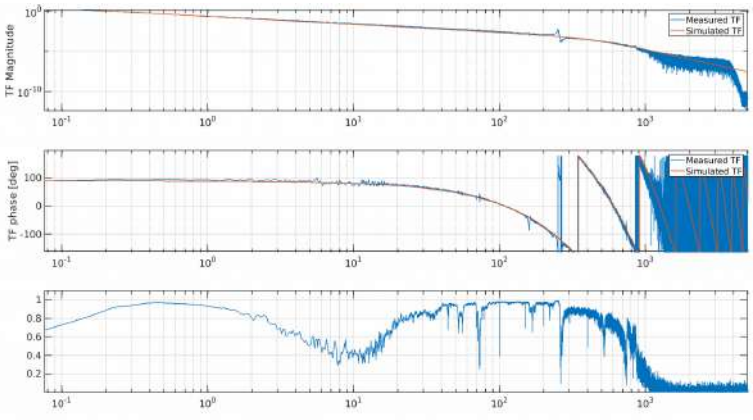


Figure 6.7: Fast and Coarse CC loops characterization. This figure shows the coarse CC open loop gain transfer function with fast CC as error signal (the red curve is the simulated and the blue curve is the measured transfer function). The top plot is the magnitude transfer function, in the center the phase transfer function and in the bottom the coherence.

range, the loop will open).

### 6.2.3 Characterization of CC loop on EQB1 bench

In this section, the results of UGF and residual phase noise obtained by closing the coarse CC loop using the fast CC loop as correction signal, only on EQB1 bench, are shown.

In order to characterize the CC loop, we measured the open loop gain transfer function (OLGTF) to have accurate simulations of the system and optimize the control filter.
Fig. 6.7 shows the coarse CC open loop gain transfer function, in which we modelled his plant with only one pole at 300 Hz with Q=0 and one delay of about 1msec. Then, we designed new filter, adding a boost at low frequencies, for both coarse and fast CC loops and in Fig. 6.9 are shown the results:

- starting from the upper plot, with new filter (the black curve) we have phase noise about 6.5 mrad, compared to the phase noise without boost of about 17.3 mrad (the blue curve);

- in the bottom plot the blue curve is the open loop and its phase noise is about 140mrad;

- the red curve in the bottom plot is the sensing noise, measuring shuttering the squeezing beam, and its residual phase noise is about 0.9 mrad;

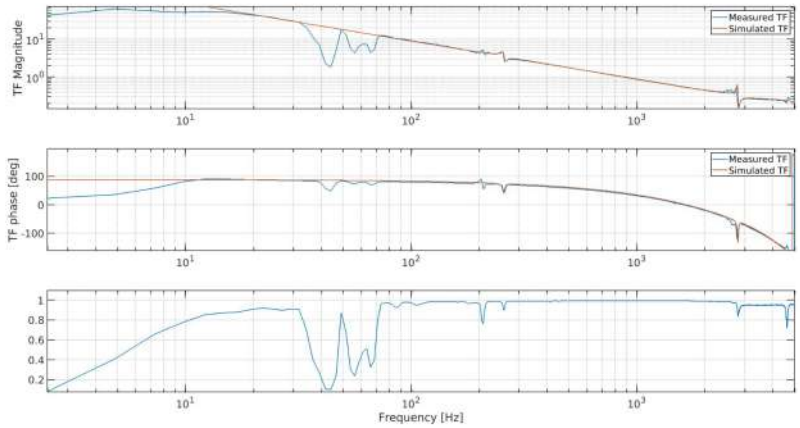


Figure 6.8: Fast and coarse CC loops characterization: we achieved an UGF about 1 kHz.

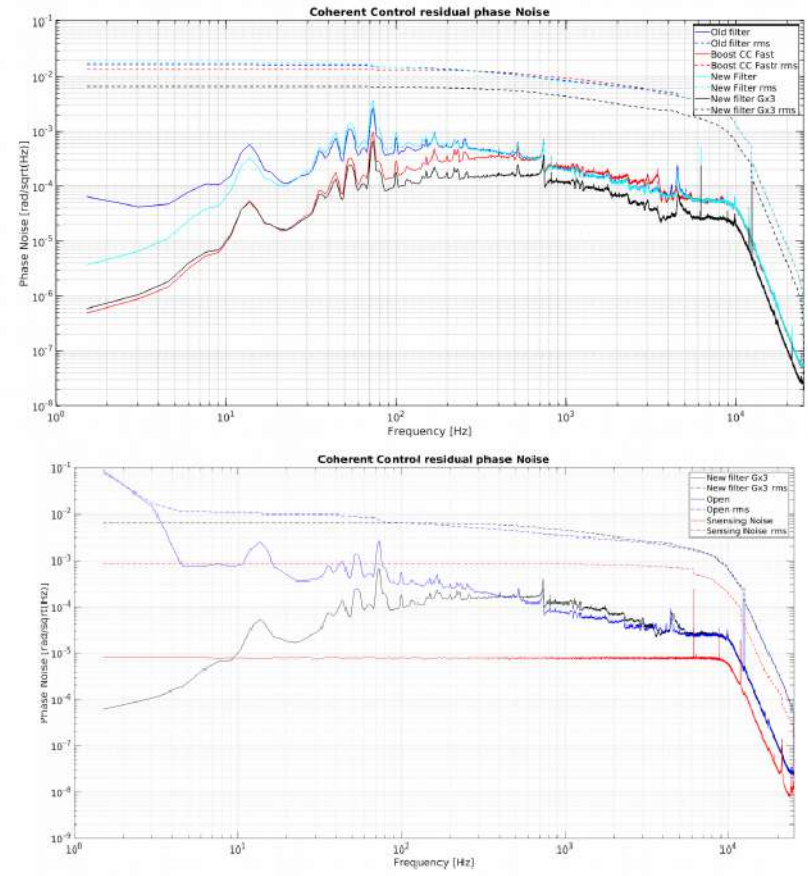


Figure 6.9: The residual phase noise results between LO and CC beams of the CC loop comparing different filters.

- the open loop residual phase noise between 1-5 kHz is about 5 mrad, so in order to decrease phase noise we need to increase the UGF (as shown in Fig. 6.8 about $\sim$ 1kHz), although it is enough for the squeezing measurements;

- in order to improve the UGF of the CC loop, we modelled the resonance around 200 Hz (see Fig. 6.7 and 6.8) and we managed to compensate it adding in the control filter a zero at 205 Hz with order Q=40 and a pole at 209 Hz with Q = 40. In this way we achieved an UGF of about 1.6 kHz. Moreover, we achieved long term stability.

### 6.2.4 FDS system: CC loop

The CC loop described in the previous section was used to measure squeezing in different configurations. We noticed that when we went to the low frequency suspended benches, a bump (Fig. 6.10) has been created due to the scattered light of the LO from the BRDF (Bidirectional Reflectance Distribution Function) of the homodyne photodiodes. The scattered light was modulated by the optical path variation between the homodyne (EQB1 bench) and the suspended element reflecting squeezing (FCIM or retroreflector). Moreover, for AdV+, the squeezing ellipse must be rotated around 20-30 Hz and in order to diagnostically measure FDS at $<$ 300Hz on EQB1 bench, we have to compensate the stray light bump on the EQB1 homodyne channel used to measure squeezing.
Thus, to fully characterize the squeezing before injecting it in the interferometer, a stray light loop (SLL) has been developed acting on the squeezing optical path to stabilize the optical path length, especially after the light has been scattered by the photodiodes, so the right actuator would be LO_M2 used for CC Coarse until then.
I won't cover the stray light loop in detail (see [50]), but it is of interest to us to define the changes to the CC loops.
With the stray light loop, the coarse CC loop is closed on Filter Cavity Input Mirror (FCIM MIR Z, as shown in Fig. 6.11), while fast CC loop is always closed on the phase-shifter LO_M1. First of all, we designed a filter for the coarse CC loop on FCIM in accord with the measured transfer function of the filter cavity (see Fig. 6.12). However, we noticed that CC coarse on FCIM only works with low seismic noise otherwise it adds noise in the filter cavity control, spoiling a lot all the cavity longitudinal and angular parameters. In fact, this problem comes from the motion of the input mirror that is misaligning the system since FCIM MIR Z is coupled with the other DoFs. The idea is to remove the actuation of the coarse CC loop from the FCIM not to re-inject noise in the system or spoil the lock of the cavity.
Therefore, some changes have been made to the configurations to make the CC loop and Stray Light Loop coexist:

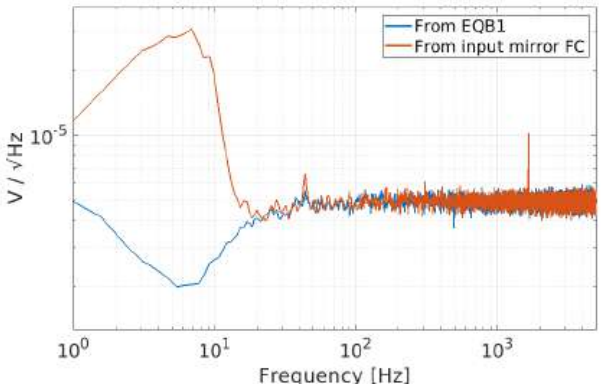


Figure 6.10: The differential channel of the homodyne detector: the blue measurement is performed only on EQB1 bench; the red measurement is performed in the entire AdV+ squeezing system. As shown in red, a noise at low frequencies appears due to scattered light generated by the LO beam diffused by the homodyne photodiodes.

- we increased the fast CC loop bandwidth by moving it to the phase shifter inside AEI Squeezer Box (as shown in Fig. 6.3). Although we already satisfied the requirement, we made this change to be able to use LO_M1 for CC coarse in order to have a little more range;
- we have added a new LO_M2 actuator (see Fig. 6.13) to increase the bandwidth of the coarse CC loop. The coarse CC loop was therefore done with LO_M1 and LO_M2, while the stray light loop is closed on M4;
- this configuration is sub-optimal because it works only when the seismic noise is very low. So, in the future LO_M1 and LO_M2 will be replaced by a closed loop actuator with the same range of M4 which will be placed in the path of LO and therefore M4 will be used for the stray light loop and LO_M1 again for the CC Coarse.

So, the last CC loop configuration composed by three actuators on EQB1 bench is shown in the following table.

| EQB1 mirrors | CC loop configuration |
|---|---|
| Phase shifter inside AEI Squeezer Box | Fast CC loop |
| LO_M1 (the actuator of the previous fast CC loop) | Coarse CC loop |
| LO_M2 (new phase shifter in front of the HD) | Coarse CC loop |

### 6.2.5 Results and conclusions

In this sections, the results obtained with the current CC loop configuration will be shown.

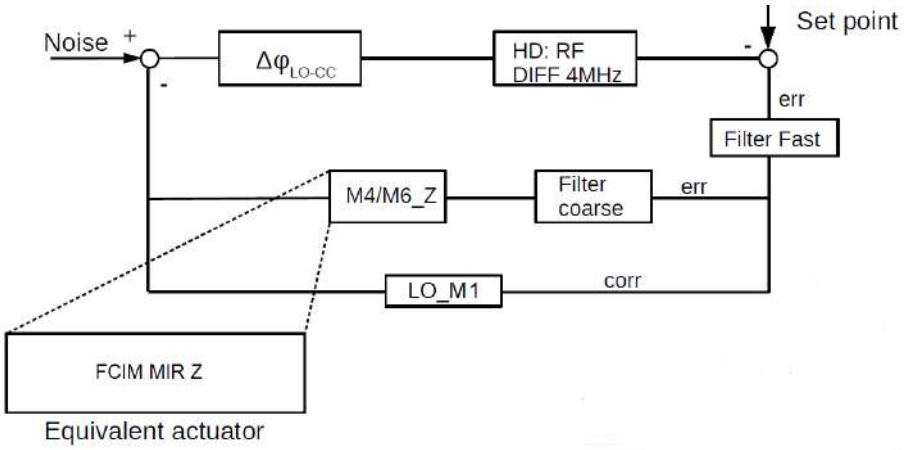


Figure 6.11: CC loops scheme with coarse CC loop closed on the Filter Cavity Input Mirror (FCIM), and fast CC loop closed on LO_M1.

Exploiting the presence of the delay line, we optimized the fast CC loop OLGTF (Fig. 6.14) improving the filter, adding also a boost filter.
In this way we improved the phase noise between 1 Hz and 5 kHz. Moreover, the peak at 55 Hz visible in Fig. 6.14 was due to a resonance of the mount mirror of the IR telescope on EQB1 bench, which was later suppressed by a clamp installation.
To have more range when the squeezing beam is sent towards the filter cavity, we can use for the coarse CC loop the actuator used for the Stray Light Loop, M4_z, choosing not to close the SLL.
Finally, the CC loop is stable and the actuation calibration range of the current CC loop configuration is shown in following the table.

| EQB1 mirrors | Actuation range [um/V] |
|---|---|
| LO_M2 (coarse CC loop) | 1.08 |
| LO_M1 (coarse CC loop) | 0.55 |
| M4_z (coarse CC loop) | 8.60 |
| AEI actuator (fast CC loop) | 0.86 |

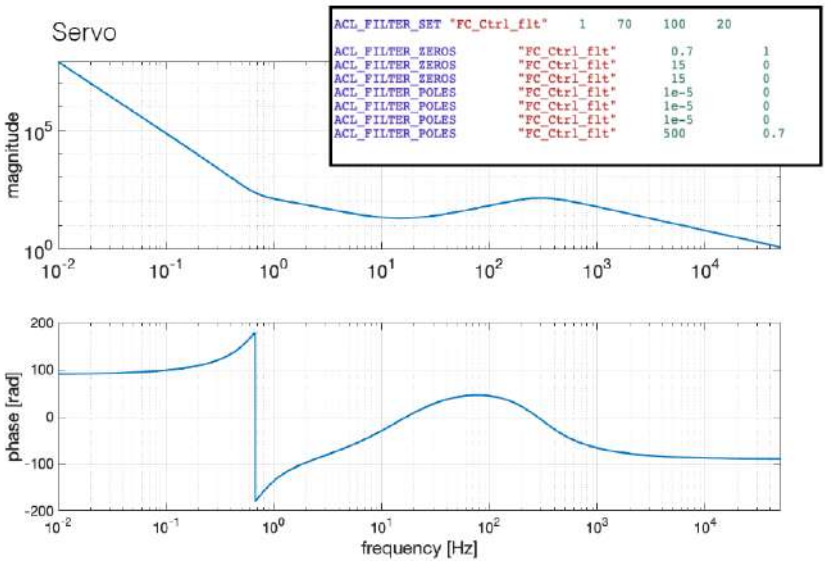


Figure 6.12: The measured transfer function of the filter cavity, with on the top the filter cavity controller in ACL code.

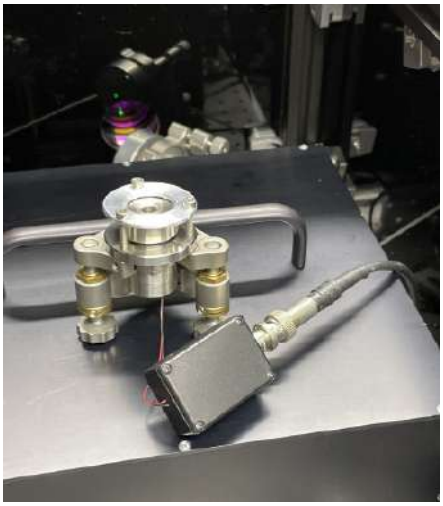

Figure 6.13: The new slow long range phase shifter for coarse CC loop (LO_M2).

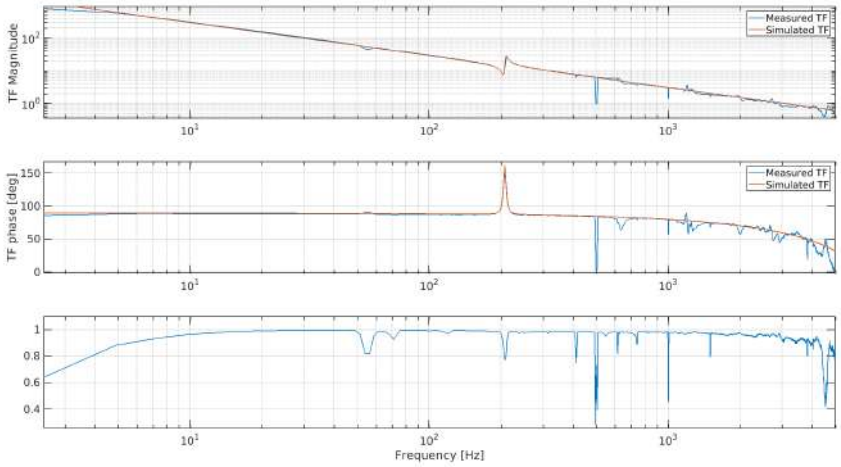


Figure 6.14: The OLG transfer function of the new fast actuator inside the AEI Squeezer Box, with delay line in order to avoid to close coarse CC loop. After filter improvements, we achieved UGF around 3 kHz.

# Chapter 7

# Automatic-alignment loops for AdV+

In this chapter, an Automatic-Alignment (AA) loop technique using dither line developed for AdV+ squeezing system will be described, in particular two preliminary AA loops fundamental before the injection of squeezing light into the interferometer will be treated.
In fact, automatic-alignment loops are needed as the observable squeezing level is reduced by misalignments, as shown in Fig.7.1. So, a system to

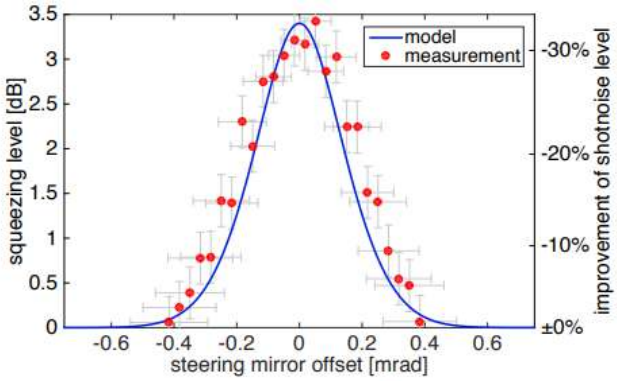


Figure 7.1: The effect of misalignment on the observed squeezing level. The squeezed beam is misaligned by rotating one of the mirrors in the input path and with 0.4 mrad of misalignment, all squeezing is lost. Misalignments are compared to a numerical model [51].

align many optical cavities automatically is needed in order to avoid the degradation of squeezing level.

## 7.1 Automatic alignment of optical cavities

First, let us look at how to align an optical cavity. Align a cavity with respect to an input laser beam or viceversa means to maximize coupling to the fundamental spatial mode, minimizing the higher-order spatial modes [52]. Moreover, the coupling can be inphase, i.e. due to the transverse displacement and mismatch of the waist size input with respect to the cavity axis and waist size, or a quadrature coupling, i.e. due to angular misalignment (tilt) and waist translation. The two types of coupling are shown in Fig. 7.2.
Let's derive the inphase and quadrature couplings starting from the orthog-

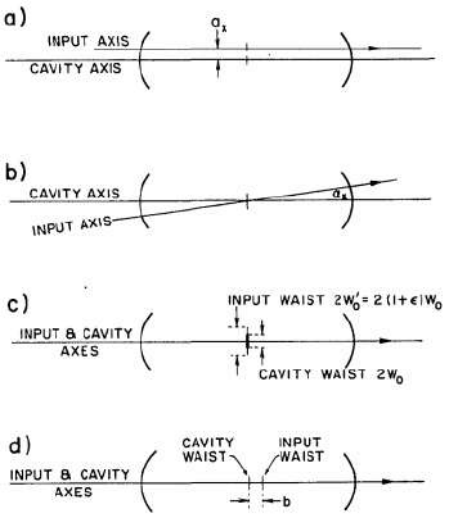


Figure 7.2: The misalignments between the input beam and the cavity axis and waist, in particular (a) and (c) are inphase coupling, transverse displacement and waist size mismatch respectively, (b) and (d) are quadrature coupling, tilt and axial waist displacement, respectively [53].

onal set of modes of propagation in a Cartesian coordinate system used to expand an electric-field distribution:

$$U_n(x,z) = N_n H_n(\sqrt{2}\frac{x}{\omega})\frac{\omega_0}{\omega} exp\{-i(kz-\phi_n) - x^2(\frac{1}{\omega^2}+\frac{ik}{2R})\} \qquad (7.1)$$

where x is the distance from the z-axis (the propagation beam axis), $H_n$ is the Hermite polynomial of order n, $N_n$ is a normalizing factor, $k = \frac{2\pi}{\lambda}$, z=0 is the position of the waist in which the beam half-width is $\omega_0$ and $\phi_n$ is the phase difference between the Gaussian beam and an ideal plane-wave approximation given by

$$\phi_n = (n+1)arctan(\frac{\lambda z}{\pi\omega_0^2}). \qquad (7.2)$$

The beam radius of curvature R is given by

$$R = z[1 + (\frac{\pi\omega_o^2}{\lambda z})^2] \tag{7.3}$$

and the beam half-width $\omega$ is given by the relation (5.1). The normalizing factor is given by

$$N_n = \frac{\Gamma(\frac{n}{2}+1)}{\Gamma(n+1)} \tag{7.4}$$

so, for n even we have $U_n(0,0) = \pm 1$ and for n odd we have $U_n(0,0) = 0$. Thus, we can write the fundamental and first two higher-order mode as follows:

$$U_0(x) = exp\{\frac{-x^2}{\omega_0^2}\} \tag{7.5}$$

$$U_1(x) = 2\pi^{\frac{1}{2}}\frac{x}{\omega_0}exp\{\frac{-x^2}{\omega_0^2}\} \tag{7.6}$$

$$U_2(x) = (\frac{4x^2}{\omega_0^2} - 1)exp\{\frac{-x^2}{\omega_0^2}\}. \tag{7.7}$$

Now, we can write the expression of a beam E=A$U_0$, with A amplitude, tilted at a small angle $\alpha$ with respect to the cavity axis (the point b in the Fig.7.2):

$$E \simeq A[U_0 + i\frac{k\omega_0}{\sqrt{2\pi}}\alpha U_1]. \tag{7.8}$$

Thus, tilting a beam that is in the fundamental mode causes a coupling into the first-order mode which is $\pi/2$ out of phase with the fundamental.
Using the same notation, we can write the expression of the input beam for the other cases show in the Fig.7.2. A beam displacements by a small amount a (the point a in the Fig.7.2) can be written by

$$E \simeq A[U_0 + i\sqrt{\frac{2}{\pi}}\frac{a}{\omega_0}U_1] \tag{7.9}$$

hence a small transverse displacement couples into the first off-axis mode as does tilting but with a $\pi/2$ phase shift.
In the case of waist-size mismatch (the point c in the Fig.7.2), i.e. if the beam and cavity waist size are mismatched by a small amount $\Delta\omega$, we can write

$$E \simeq A[U_0 + i\frac{\Delta\omega}{2\omega_0}U_2] \tag{7.10}$$

so, it can be described as an in-phase addition of a second-order mode term. Finally, in the case of axial waist displacement (the point d in the Fig.7.2),

i.e. if the waist position of the beam is displaced by a small amount b along the cavity axis, we can write the electric field of the input beam as follows

$$E \simeq A[U_0 + i\frac{b}{2k\omega_0^2}(U_2 + U_0)] \tag{7.11}$$

thus, a curvature mismatch is represented by a coupling into the second-order mode that is $\pi/2$ out of phase with the fundamental.

## 7.2 Homodyne automatic-alignment loop using dither line technique

In ADV+ squeezing system, a homodyne detector (HD) is present on the in-air External sQueezing Bench (EQB1) for diagnostic measurements (Fig. 7.3).
As the beams travel from EQB1 bench on the suspended benches to reach the filter cavity, back and forth, there could be long-term drift, so an alignment system to keep constant level of SQZ is needed.
In this section the homodyne automatic-alignment loop will be describe.
In order to sense the interference between a local oscillator (LO) taken from the squeezer and the squeezed beam (section 3.1.1), the two beams must obviously be superposed, maximizing a physical observable and to do that we developed an AA loop.
Let's describe the logic of the loop [54].

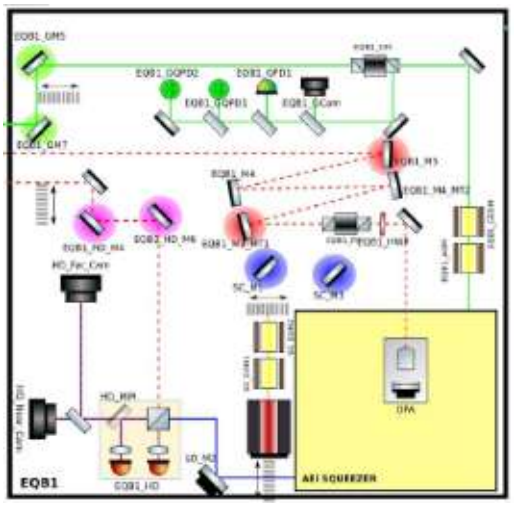


Figure 7.3: External in-air squeezing bench in Advanced Virgo Plus. Colored mirrors are motorized. The AEI squeezer is inside the yellow box [32].

The AA loop uses dither lines to find a global maximum for each DoF of the actuators used. Dither lines are small sinusoidal modulations at well

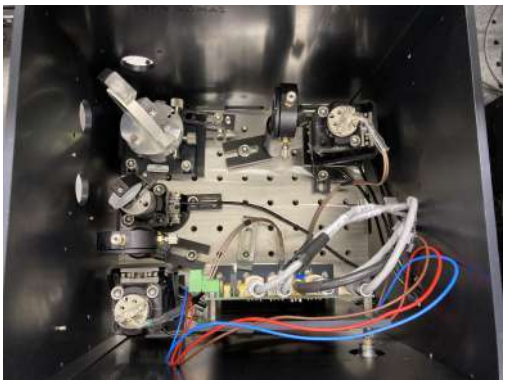

Figure 7.4: A picture of the interior homodyne detector installed in the external in-air squeezing bench for Advanced Virgo Plus squeezing system.

separated frequencies. The optimal alignment occurs when the effect of the angular modulation is minimal. Moreover, the error signal of the loop is extracted by demodulating dither lines applied to each DoFs of the actuators. A diagonal driving matrix provides the corrections to be given to the actuators starting from sensing (error signals).
Concerning the driving, the AA loop uses piezo-intertia actuators (the pink-mirrors $M_4$ and $M_6$ represent in Fig.7.3) and are in front of the homodyne detector.
The sensing of the loop is represented by the amplitude of the beatnote at 4 MHz between LO and CC beams measured by the difference between the photocurrents of the two photodiodes inside the HD (see Fig.7.4). This beatnote is first demodulated at 4MHz and then separately demodulated four more times at the frequency of the four dither lines.
In order to close the AA loop, it is necessary to pre-align the system and to do that we have installed two cameras to image the Near-Field and Far-Field, as shown in Fig.7.3. The Near-Field camera is positioned on the waist of the beam, where we have flat waves and it is sensitive to tilts. Instead, the Far-Field camera is sensitive to shifts, having spherical waves.

### 7.2.1 Pre-alignment procedure

As we cannot see the squeezing beam on the cameras, we overlap the sub-carrier beam, which is collinear with the coherent control beam and the squeezing beam in the OPA inside the AEI squeezer box, with the Local Oscillator (LO).
As shown in Fig. 7.3, the combined beams on the homodyne beam splitter are deflected with a motorized mirror (HD_MIR) towards the two cameras, in order to optimize their relative alignment and mode matching.
First of all, mode-matching has been optimized with a motorized telescope

Figure 7.5: A picture of the pre-alignment procedure with the sub-carrier and the local oscillator beams on the Near-Field camera.

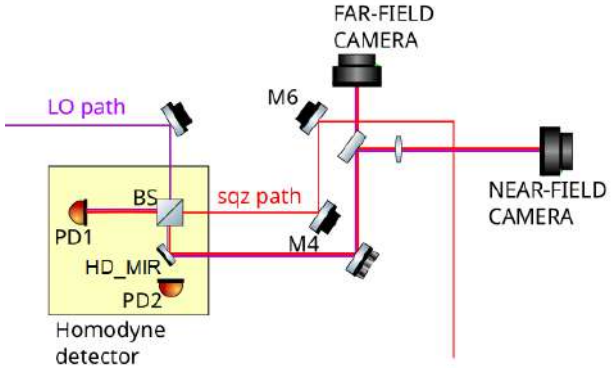


Figure 7.6: Optical setup of the EQB1 bench with particular attention to the optical paths of the LO and the sqz beams inside the homodyne towards the Far-Field camera and the Near-Field camera, using a removable mirror (HD_MIR).

lenses on LO path so as not to be touched again. Then, by alternatively closing the shutters on LO and SQZ paths, the position and size of laser spots on the cameras are recorded (see Fig.7.5), then the actuators on the LO path are tuned to overlap sub-carrier on LO. Thus, the sub-carrier beam is shuttered, the combined beams (SQZ+CC and LO) are sent to the homodyne photodiodes and no longer to the cameras (by moving the motorized mirror) and the interference fringes between the superimposed beams are observed. The optical setup of the SQZ and LO paths is shown in Fig. 7.6.
At this point the AA loop comes into play.

### 7.2.2 Scheme of homodyne automatic-alignment loop

The goal of the AA loop is to maximize the magnitude of the beatnote at 4MHz between coherent control beam and a reference beam (local oscillator beam) on the homodyne detector demodulated at the dither line frequencies. In this way, we are superimposing the LO with the squeezing beam, since the coherent control beam is transmitted by the OPO, hence it is collinear with the squeezing beam.

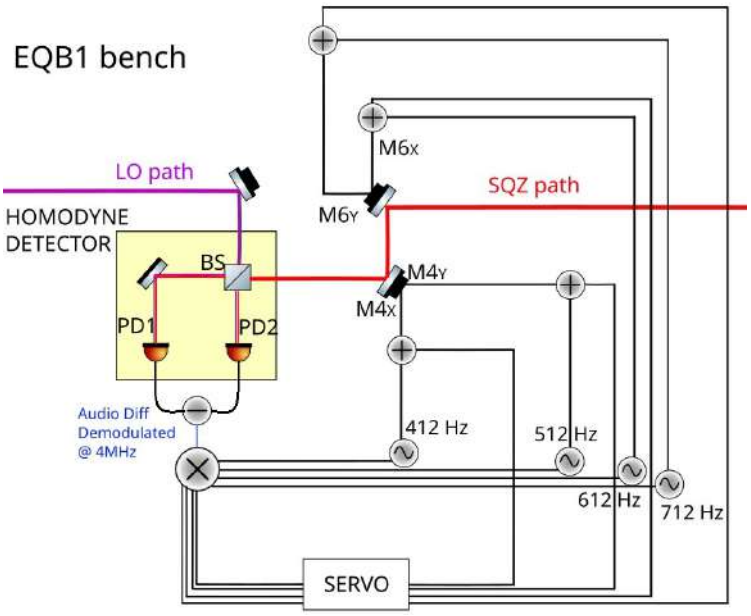


Figure 7.7: Scheme of homodyne automatic-alignment loop, in particular the extraction of error signals with dither lines technique is shown.

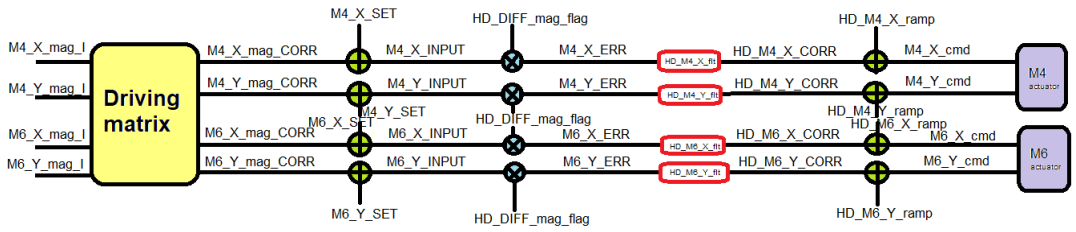


Figure 7.8: Control scheme of the homodyne automatic-alignment loop using dither line technique. Once the error signals have been extracted, from the driving matrix (on the left) we get the corrections to be provided to the mirrors (on the right).

Let's analyze in detail the AA loop written in ACL code, whose schemes are shown in Fig. 7.7 and in Fig.7.8.
We sent one dither line for each degree of freedom of the two actuators $M_4$ and $M_6$, with frequencies in the bandwidth with less noise and well separated: 412 Hz, 512 Hz, 612 Hz, 712 Hz. Dither lines create disturbances on a degree of freedom used to align the HD magnitude (mag in the Fig. 7.8) on the frequency of the line. In order to extract an error signal, the magnitude is demodulated at the frequency of the dither line. We have defined the phase of the error signals, i.e. of the I and Q quadratures and we tuned this phase in order to see all the signal on the I quadrature.
Therefore, the frequencies of the dither lines are used both for demodulation, in fact to create the I and Q signals the magnitude is taken and demodulated at the dither line frequency, and for the control filters, in fact to be sure to remove disturbances in the error signal at the line frequency, we also add a notch (a band-stop filter) at the line frequency in the demodulation filter.
Then, we got the sensing matrix, that is the inverted driving matrix (shown below in ACl code), which gives us the corrections to be given to the actuators as shown with the command ACL_MATRIX_BEGIN.
Therefore, the error signal is the correction from the driving matrix added

```
ACL_MATRIX_BEGIN "HD_MAG_MAT"   1       HD_M4_X_mag_I   HD_M4_Y_mag_I   HD_M6_X_mag_I   HD_M6_Y_mag_I
ACL_MATRIX_CH    "HD_M4_X_mag_CORR"  ""      1.          0.          0.          0.
ACL_MATRIX_CH    "HD_M4_Y_mag_CORR"  ""      0.          1.          0.          0.
ACL_MATRIX_CH    "HD_M6_X_mag_CORR"  ""      0.          0.          1.          0.
ACL_MATRIX_CH    "HD_M6_Y_mag_CORR"  ""      0.          0.          0.          1.
ACL_MATRIX_END   "HD_MAG_MAT"
```

to the setpoints of the mirrors $M_4$ and $M_6$.
On the scheme in Fig. 7.8 is also present a flag (HD_DIFF_mag_flag) that is a check that the beam is arriving on the homodyne's photodiodes.

### 7.2.3 Results and discussion

Since squeezing must have a long term operation and since there are slow drifts between suspended objects and objects on the ground, to demonstrate this long term operation with the diagnostic mode we have implemented the AA loops.

Fig. 7.9 shows the signals of interest when the automatic-alignment loop is closed. So, the loop works in fact the magnitude is maximized and the error signals go to 0. However, the actuators diverge due to the fact that they are too close together, they have too little Gouy phase and therefore both cannot be used at the same time. In the definitive version of the HD AA loop, we use only M6 actuator and the HD AA loop is stable.

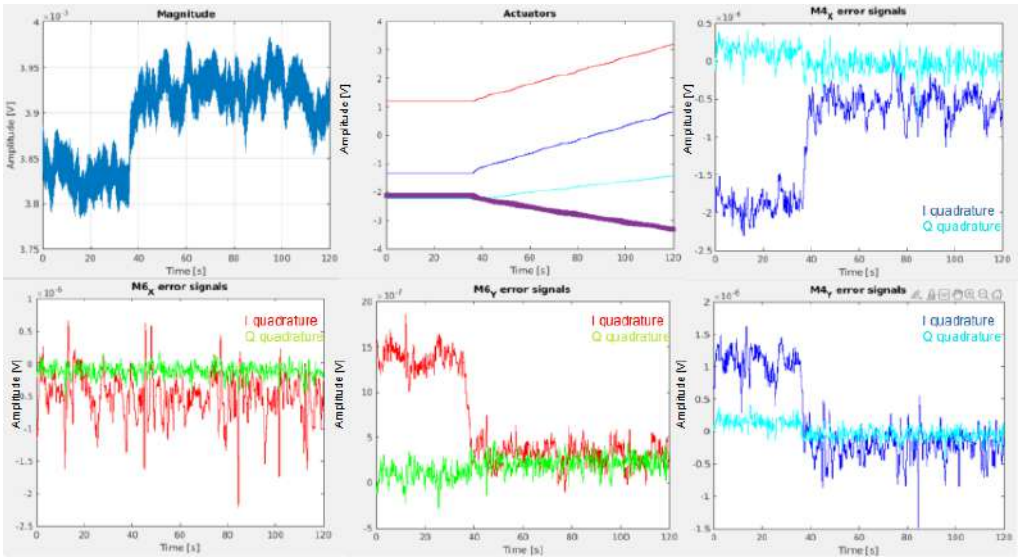


Figure 7.9: Signals of interest for the homodyne automatic-alignment loop. Starting from the top left plots, we have the magnitude of the beatnote at 4MHz between the coherent control beam and the local oscillator beam, in the top center the setpoints of the DoF of the two actuators, the other show the I and Q error signals for each DoF. At about 38 sec, we closed the HD AA loop and the error signals went to 0, maximizing the magnitude [54].

## 7.3 Sub-carrier automatic-alignment loop using dither line technique

In AdV+ squeezing system we developed another AA loop on EQB1 bench using dither line technique: sub-carrier AA loop.
The IR sub-carrier field laser is phase locked to main laser frequency of the AEI squeezer with a frequency offset of 1.26 GHz, such as to be anti-resonant in the OPA of the squeezer source, in the interferometer output mode cleaner and signal recycling cavities (section 3.1).
Passing through an EOM for the PDH sidebands, the sub-carrier field is sent to and reflected from the low-losses single in-air Faraday isolator on the squeezed vacuum path back towards the OPA to be mode-matched. It is then reflected by the OPA, so co-propagating with the squeezed field towards the filter cavity. The sub-carrier beam path is shown in Fig. 7.10.

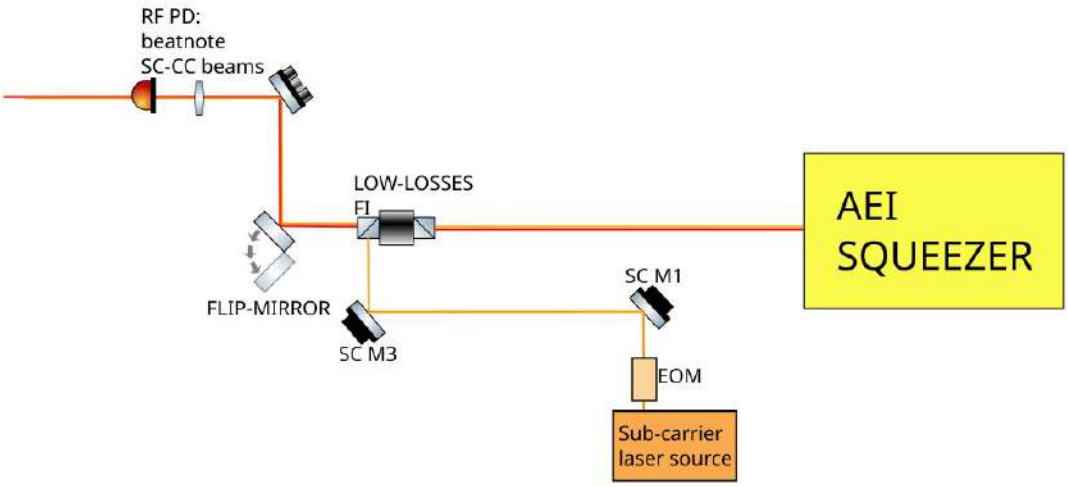


Figure 7.10: Sub-carrier beam path. In this scheme are shown only the main part of the beam path, in particular from the SC laser source, the beam goes through the EOM in order to generate the sidebands for the PDH, then using the two actuators M1 and M3 it goes through the single low-losses FI in order to go towards the AEI squeezer inside the OPA. Then it is reflected from the OPA and goes again through the single FI and with a flip-mirror we can measure the beatnote on a RF photodiode between the SC beam and the CC beam.

### 7.3.1 The logic of the SC AA loop and results

The goal of SC AA loop is to measure and to maximize the amplitude of the sub-carrier and the coherent control beams beatnote at 1.26 GHz with a RF power detector.
The logic of the loop is the same that the homodyne AA loop, but in this case the driving is composed by two other tip-tilt piezo-inertia actuators (M1 and M3 in Fig. 7.10) before the single Faraday Isolator on EQB1 bench (the blue mirrors in Fig. 7.3).
In order to measure the beatnote, we aligned a fast photodiode in reflection

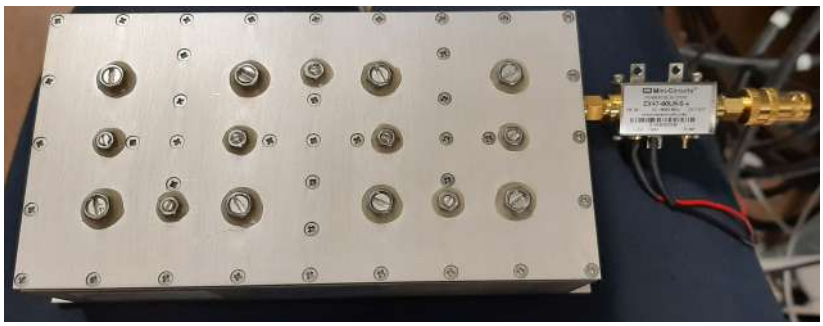

Figure 7.11: A chain at sub-carrier photodiode output made of a RF cavity filter (BP1260-12.6-8CS, YUN Micro Electronics), centered aroud 1.26 GHz, and a RF power detector (ZX47-60LN-S+, Minicircuit).

from a flip-mirror controlled via remote after the EQB1 Faraday isolator: in this way, one can either observe the output signal from the FI on the fast photodiode (by pulling up the flip-mirror), or send the SC beam towards the homodyne (by pulling down the flip-mirror).
Then, we applied a chain at the fast photodiode output made of a RF cavity filter, centered aroud 1.26 GHz, and a RF power detector (see Fig. 7.11).
Fig. 7.12 shows the RF cavity filter characterization: the output of the RF power detector decreases when RF beatnote power increases. The output of the power detector is acquired on a DAQ channel using a line driver.
So, we demodulated this channel at the angular dither lines frequencies to get the error signals for the SC AA loop (Fig. 7.14). The dither lines frequencies of the SC AA loop are the same used for the HD AA loop (412 Hz, 512 Hz, 612 Hz, 712 Hz), but in this case applied on each DoF of the two actuators on the SC path before the Faraday isolator.
Once the beatnote is maximized on the fast photodiode, the SC AA loop has to be open and the beam is sent towards the homodyne on a photodiode in front of the HD. In this way, we can check the mode-matching of the SC on OPA, scanning the OPA inside the AEI squeezer by remote, and observe the DC signal on the photodiode.
Fig. 7.15 shows the 99 % mode-matching achieved of sub-carrier beam on

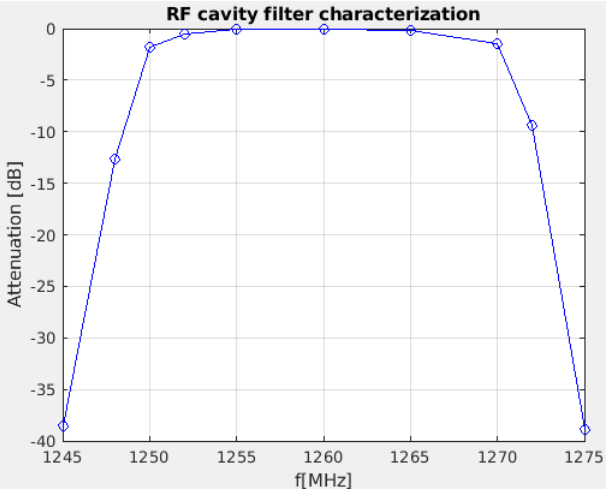


Figure 7.12: The RF cavity filter characterization.

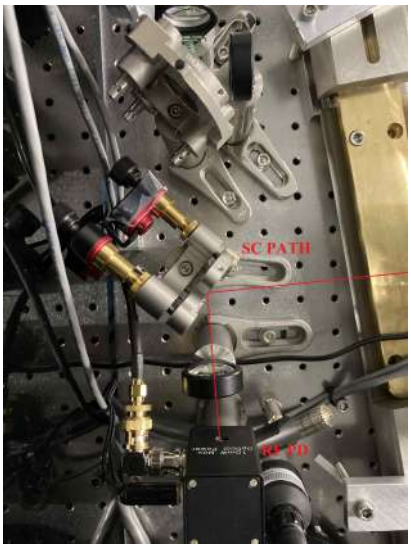


Figure 7.13: RF photodiode for the SC and CC beatnote.

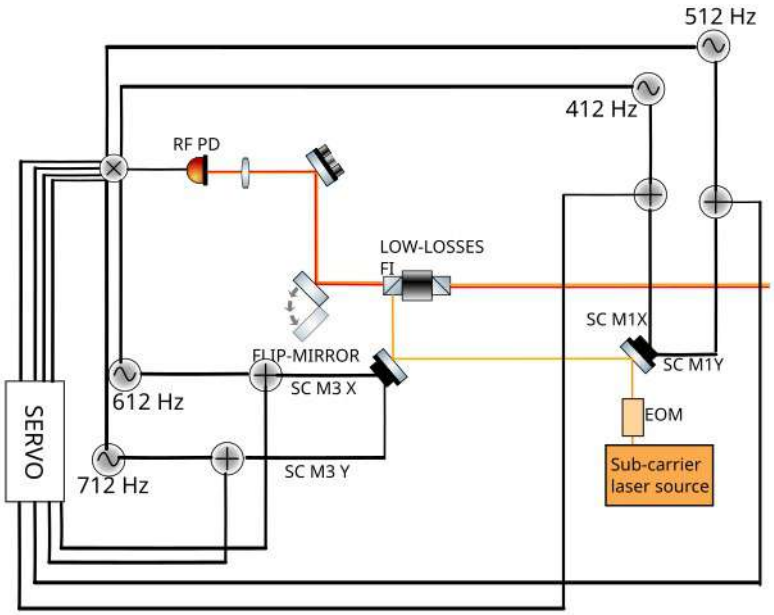


Figure 7.14: The extraction of error signals in the SC AA loop with dither lines technique.

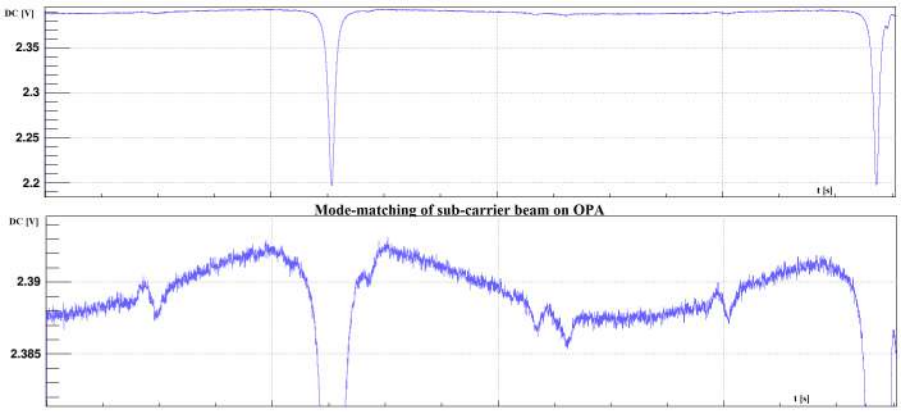


Figure 7.15: Mode-matching of sub-carrier beam on OPA: 99%. The figure below shows the higher-order peaks zoomed in.

OPA, where the dips are due to the resonant coupling of SC beam into the OPA and in this measurement we were in squeezing mode. In the case of BAB mode, in the mode-matching measurement we would have seen the transmission peaks of the BAB above the bias due to the off-resonant reflection of the SC beam.

# Chapter 8

# The development of the EPR experiment

A different technique to achieve a broadband quantum noise reduction below the standard quantum limit has been proposed in 2017 by Ma et al. [38]. This proposal uses a pair of squeezed EPR entangled beams to produce frequency-dependent squeezing by a non-degenerate OPO consinsting of KTP (Potassium Titanyl Phosphate) crystal inside optical cavity and does not require additional filter cavity (see section 3.2). Eliminating the need for external cavity, this method is less expensive, has more compact setup and it avoids the 1ppm/m round trip losses for the filter cavity, but on the other side two squeezed beams imply double losses and the need for two homodyne detectors to reveal them.
This method was already demonstrated and tested in a single cavity by the German and Australian groups, but it has never been demonstrated and tested in an interferometer [55].
In this chapter, the design and characterization of the EPR experiment in the R&D laboratory at EGO-Virgo site are described [56].

## 8.1 Optical design of the EPR experiment

The EPR R&D project has been installed at EGO-Virgo site.
Prior to the EPR setup, a FIS R&D bench was installed and new control techniques with finite state machine Virgo-compatible were developed (see [57]).

Fig. 8.1 and Fig. 8.2 show the conceptual design of a table-top EPR experiment and the optical setup that we developed at EGO-Virgo site, respectively.
Starting from the conceptual design, we have three lasers:

- the first is for the Second-Harmonic Generation (SHG) that goes into the Optical Parametric Oscillation (OPO) and then produces two

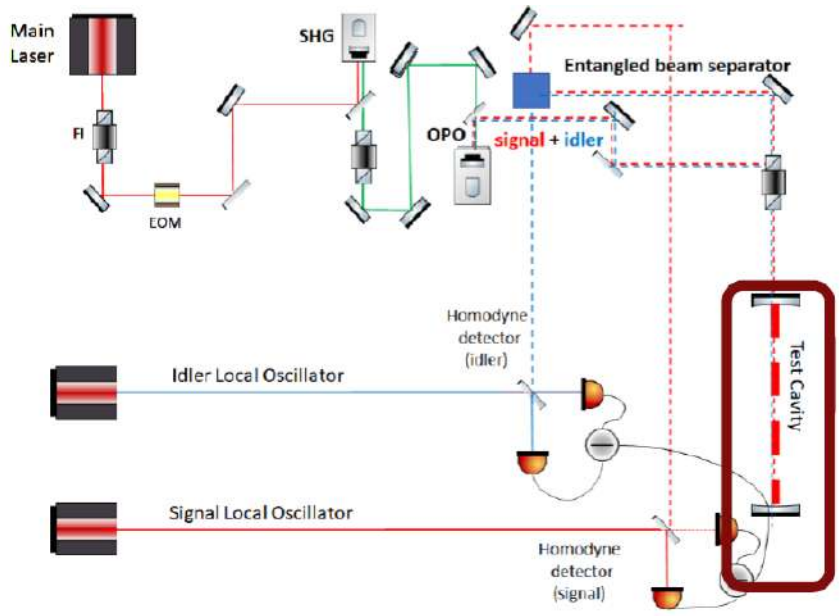


Figure 8.1: The conceptual design of a table-top EPR-experiment, in which a test-cavity is used instead of the interferometer.

beams (signal and idler) that will go into the test cavity, which acts as an interferometer and must be detunate for the idler;

- the second provides the local oscillator for the idler;
- the third provides the local oscillator for the signal.

The two lasers that provide the local oscillator beams have the frequency of the idler and the signal beams, and their frequency shift with respect to the main lasers are obtained by two fast OPLLs (Optical Phase Locked Loops) [58]. The local oscillator beam is a reference beam that has the desired squeezing frequency to be revealed and selects the beam by the beatnote. Moreover, only one beam is produced from the OPO, in fact signal and idler are generated together, so we have to separate them since they have different frequencies and we detect them using two homodyne detectors. The homodyne measurement of a fixed quadrature of the out-going idler field conditionally squeezes the input signal field in a frequency-dependent way, and in this way broadband reduction of quantum noise is achieved.

In our optical setup (Fig. 8.2) we have only two lasers, in fact we installed four acousto-optical-modulators (see chapter 5 for details on how they work) in order to provide the beams for the coherent control of idler and signal, so we don't need the two OPLLs. Moreover, the AOMs are also used to lock the OPO and the test cavity.

Thus, we proposed, for the first time, an optical setup to inject EPR-

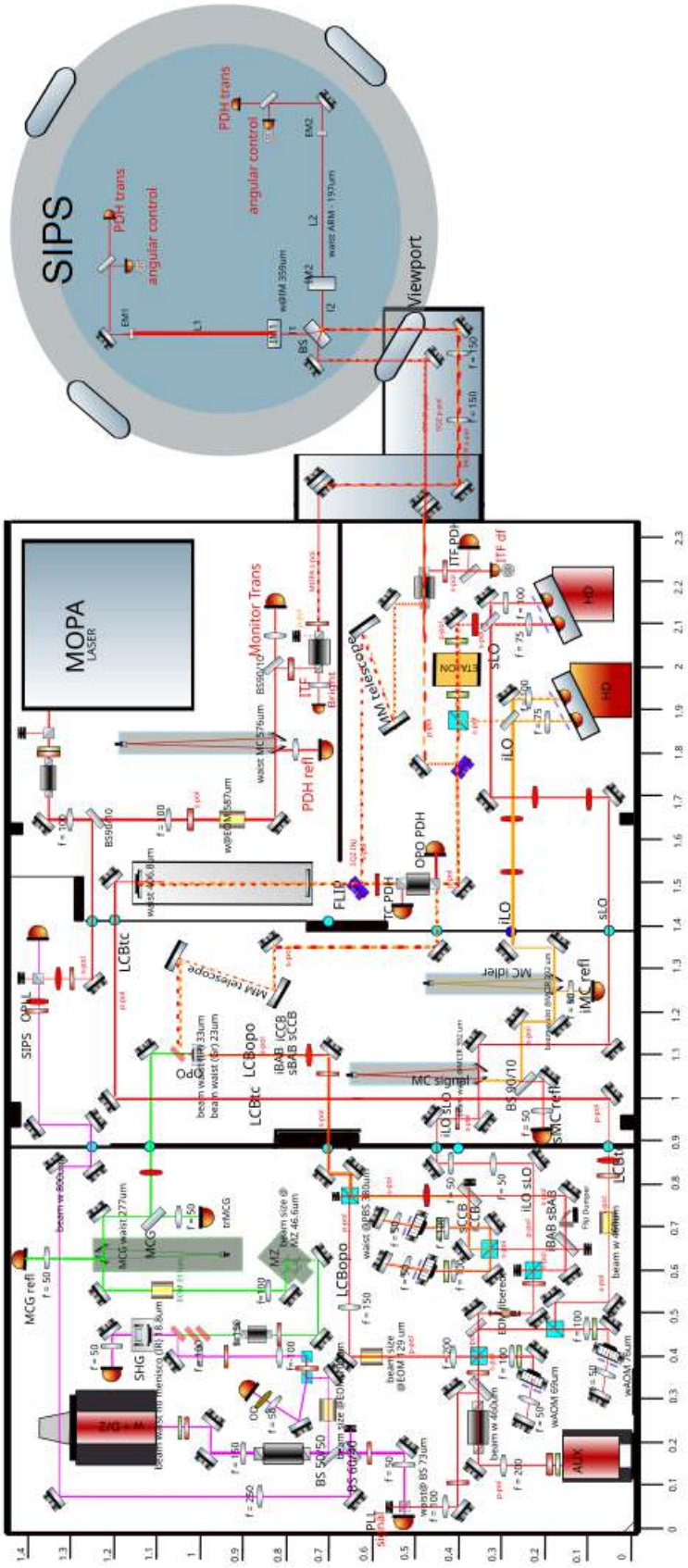


Figure 8.2: Optical setup for EPR table-top experiment in the R&D laboratory at EGO-Virgo site (inkscape drawing).

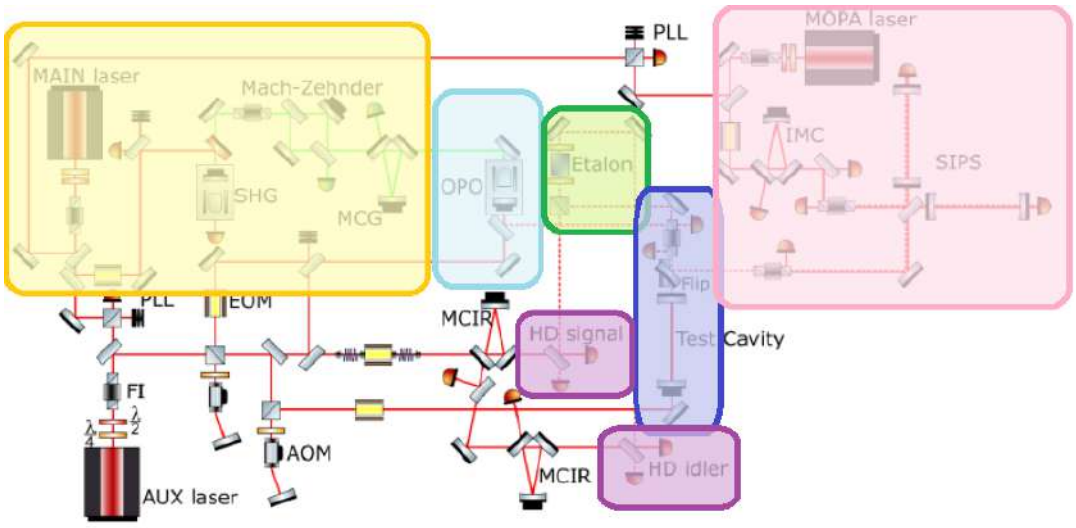


Figure 8.3: Simplified optical setup for EPR table-top experiment in the R&D laboratory at EGO-Virgo site. Notice that only two of the four AOMs are shown in this optical setup.

squeezed fields into SIPS (Suspended Interferometer for Ponderomotive Squeezing), i.e. into a small-scale suspendended interferometer in the same frequency band of gravitational wave detector, which is sensitive either to radiation-pressure-noise and shot-noise, depending on the observation frequency [**?**]. SIPS is a suitable demonstrator of EPR principle before possible integration in GW detector (for example in Einstein Telescope [59]) and in this way a frequency-dependent reduction of quantum noise will be achieved. SIPS project was developed by Roma group [60].

In order to understand the function of each part of our optical setup, in Fig. 8.3 is shown a simplified optical bench:

- in pink we have the optical setup for the injection in a small suspended inerferometer similar to Virgo detector;

- in yellow we have the optical setup for the pump beam generation: the produced beam will be used as pump beam for the OPO (see Fig. 8.4);

- in light-blue is shown the entangled beams production by a non-degenerate OPO;

- in green is shown the etalon cavity for the separation of the two entangled beams (see Fig. 8.5);

- in blue is shown the optical setup for the injection into the test cavity;

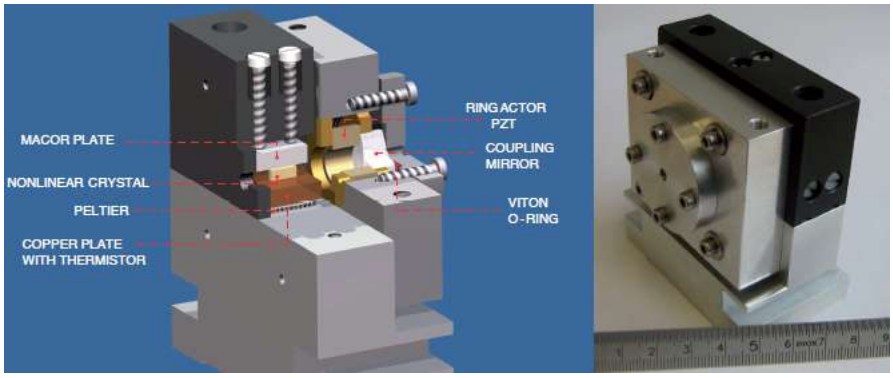


Figure 8.4: A picture of the SHG (Second-Harmonic-Generation) cavity, which generates the squeezing pump beam at 532 nm. SHG is an hemilithic cavity, consisting of a PPKTP (Periodically Poled Potassium Titanyl Phosphate) non linear crystal and a coupling mirror [9].

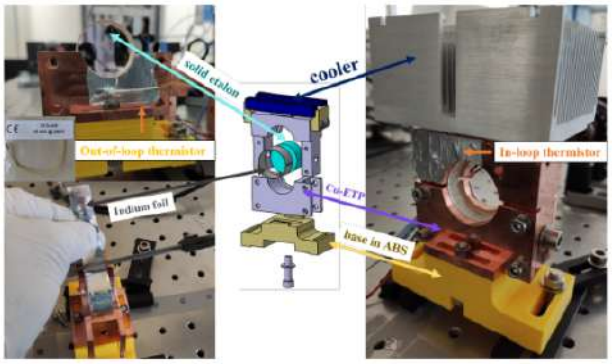


Figure 8.5: The mechanical design of the etalon holder: on the top, a Peltier element and a cooler; an indium foil covers the ethalon lateral side to have a good thermal contact between the etalon and the holder; on the bottom a polymer ABS to ensure no thermal cut-off between the optical table and the holder [61].

- in purple the homodyne detectors to reveal the two entangled beams are shown. In fact, each squeezed beam, separated by etalon cavity, interferes with a local oscillator beam at a 50:50 beam splitter. In this way, the two identical beams exit the output ports of the beam splitter and arrive at two photodiodes whose photo-currents will be subtracted so that classical noise will be cancelled and only quantum noise of the reference beam will survive, which will be reduced by the squeezed beam.

So, in our EPR experiment, the idler that is detuned with respect to the test cavity, experiences a frequency-dependent reduction of quantum noise. The entanglement of signal and idler assures that also the signal will be squeezed in a frequency-dependent manner.
The final goal of our EPR experiment is to inject for the first time, these beams in a system sensitive to quantum noise in the whole detection bandwidth at the same frequencies of GW detectors.

## 8.2 Optical setup of the EPR experiment

The optical design for the EPR experiment is completed. We calculated focal lenses with Gaussian Beam software, which is a Gaussian optics simulator with a graphical interface and an optical data editor. Through Gaussian beam we simulated the optical paths of all the beams present in the optical design, in particular taking into account the double-pass of the AOMs: as well described in the chapter 5, it is necessary to simulate the incident beam in the AOM (single-pass) and then the retroreflection (double-pass). An example of this type of simulation is shown in Fig. 8.6, in which we simulated the optical path from the AUX laser to the first AOM, shown in our optical design (see path shown in Fig. 8.2).
The optical setup is in progress, in particular we have to complete the optics installation and their alignment before the two homodyne detector used to measure the two entangled beams.
In the next sections, three activities related to the cavity test for EPR optical setup are shown.

### 8.2.1 SHG cavity alignment

The test of the SHG alignment was perfomed in Genoa laboratory and the optical setup is shown in Fig. 8.9. Before to align the SHG cavity, we checked the status of the crystal inside the cavity and of the coupling mirror with a microscope (see Fig. 8.7 and 8.8).
The optical setup for the SHG alignment is shown in Fig. 8.9.
Fig. 8.10 shows the simulation of the optical path of the beam towards the SHG cavity, adding two lenses in order to obtain the right size of the waist

| Optics | Position (mm) | Relative position (mm) | Properties | Waist (µm) | Waist position (mm) | Rayleigh range (mm) | Divergence (mrad) | Sensitivity (%/mm²) | Name |
|---|---|---|---|---|---|---|---|---|---|
| Input beam | -90 | | n = 1, M² = 1 | 132 | -90 | 51.4465 | 2.56576 | 0.00944556 | w0 |
| Lens | 140 | 230 | f = 200 mm | 443.291 | 678.338 | 580.211 | 0.764017 | 0.0103448 | L2 |
| Flat mirror | 365 | 225 | | 443.291 | 678.338 | 580.211 | 0.764017 | 0 | BS after FI |
| Flat mirror | 440 | 75 | | 443.291 | 678.338 | 580.211 | 0.764017 | 0 | PBS |
| Lens | 515 | 75 | f = 100 mm | 69.5713 | 608.514 | 14.2912 | 4.86809 | 0.12645 | L3 |
| Flat mirror | 608.444 | 93.444 | | 69.5713 | 608.514 | 14.2912 | 4.86809 | 0 | AOM1 |
| Lens | 658.444 | 50 | f = 50 mm | 243.403 | 707.591 | 174.929 | 1.39144 | 0.143223 | L4 |
| Flat mirror | 708.444 | 50 | | 243.403 | 707.591 | 174.929 | 1.39144 | 0 | M4 |
| Lens | 758.444 | 50 | f = 50 mm | 69.5713 | 808.514 | 14.2912 | 4.86809 | 0.143223 | L5 |
| Flat mirror | 808.444 | 50 | | 69.5713 | 808.514 | 14.2912 | 4.86809 | 0 | AOMreturn |

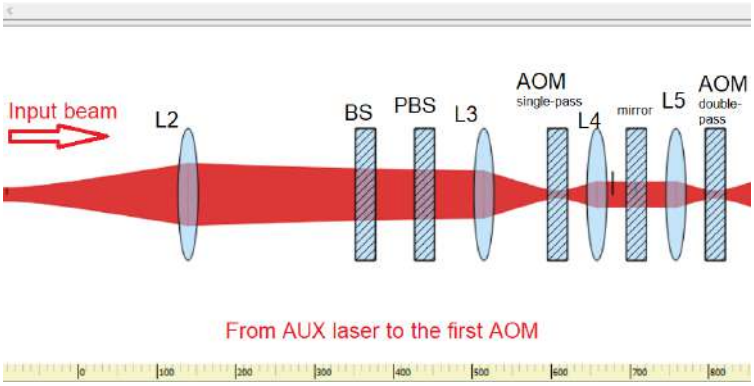


Figure 8.6: Data editor and graphical interface from Gaussian Beam software of the simulation of the optical path from the AUX laser to the first AOM.

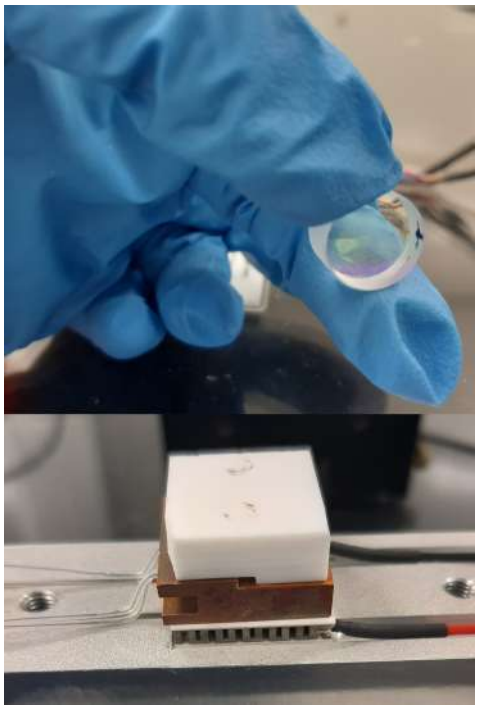

Figure 8.7: On the top, the coupling mirror of the SHG is shown. On the bottom, the crystal inside the SHG cavity is shown.

inside the SHG (about 30 $\mu$m at 1064 nm).
To correct align the SHG cavity, we followed this procedure:

- we mounted the SHG cavity by inserting the peltier cell and thermometers in the correct position (fixing the wires for the Thermoelectric Cooler (TEC) control in the cavity with conductive paste);

- we removed the coupling mirror;

- we aligned the cavity by observing the beam in transmission with a beam profiler;

- we moved the steering mirrors (M1 and M2 in Fig. 8.9) so that the beam reflected from the SHG and the incident beam coincide;

- we positioned the coupling mirror so that the incident and the reflection coincide.

This alignment has to be optimized in order to achieved about 91% of fundamental mode content for the transmitted power.

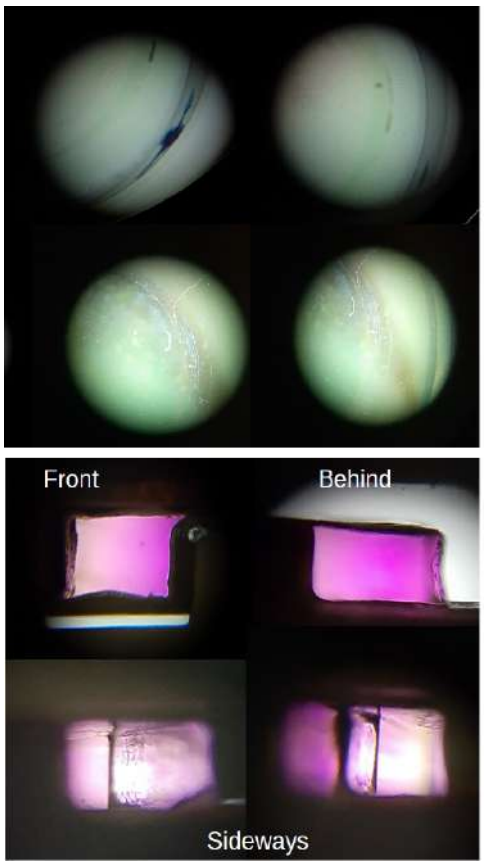


Figure 8.8: Check of the SHG cavity status. On the top, the coupling mirror seen with the microscope. On the bottom, the crystal inside the SHG cavity seen with the microscope. For both, no evidence of fractures, only presence of dusts.

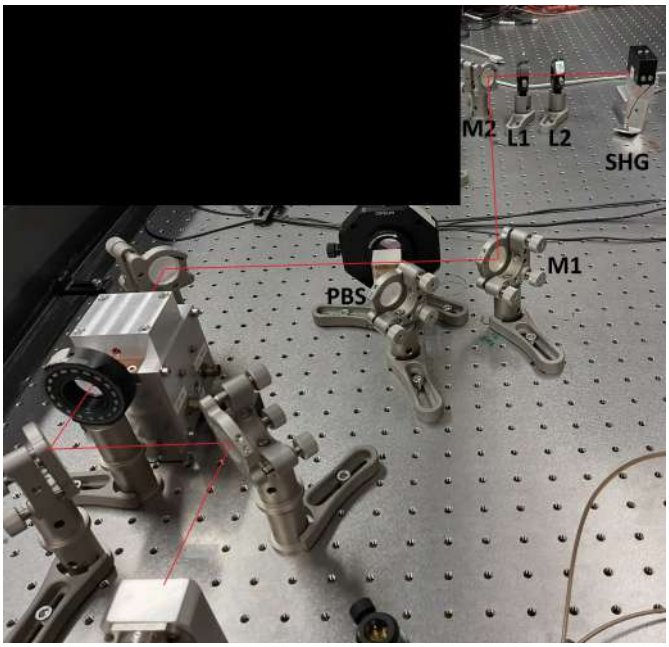


Figure 8.9: Optical setup for SHG alignment performed in Genoa laboratory.

| Optics | Position (mm) | Relative position (mm) | Properties | Waist (µm) | Waist position (mm) | Rayleigh range (mm) | Divergence (mrad) | Sensitivity (%/mm²) | Name |
|---|---|---|---|---|---|---|---|---|---|
| Input beam | 10 | | n = 1, $M^2$ = 1 | 600 | 10 | 1062.94 | 0.564469 | 2.21323e-05 | w0 |
| Flat mirror | 40 | 30 | | 600 | 10 | 1062.94 | 0.564469 | 0 | M1 |
| Flat mirror | 160 | 120 | | 600 | 10 | 1062.94 | 0.564469 | 0 | M2 |
| Lens | 240 | 80 | f = 300 mm | 168.975 | 534.448 | 84.3048 | 2.00433 | 0.00409279 | L1 |
| Lens | 283 | 43 | f = 50 mm | 26.9915 | 325.308 | 2.15111 | 12.5471 | 5.17056 | L2 |
| Flat mirror | 325 | 42 | | 26.9915 | 325.308 | 2.15111 | 12.5471 | 0 | SHG |

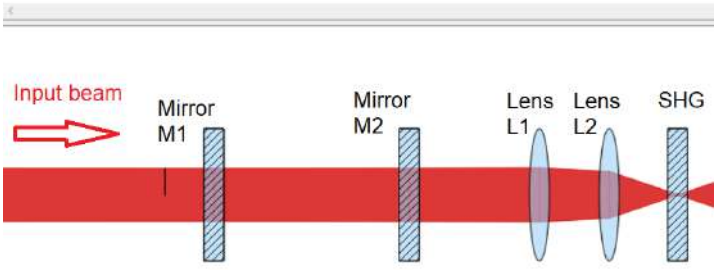


Figure 8.10: Data editor and graphical interface from Gaussian Beam software of the simulation of the optical path for SHG alignment.

### 8.2.2 Etalon alignment

The test of the etalon alignment was performed at EGO-Virgo site in the R&D laboratory. In this section, the Etalon alignment procedure for the EPR experiment will be explained.
A solid etalon is a monolithic Fabry-Perot cavity necessary for the separation and detection of two entangled beams in the EPR experiment (for more details on the etalon development, see [61]).
This system is able to separate the two entagled beams, in particular signal beam trasmitted at 97.4% and idler beam reflected at 97.8% (see Fig. 8.11). Each of them will be detected by two separate homodyne detectors.

The optical design and setup for the etalon alignment are shown in Fig.

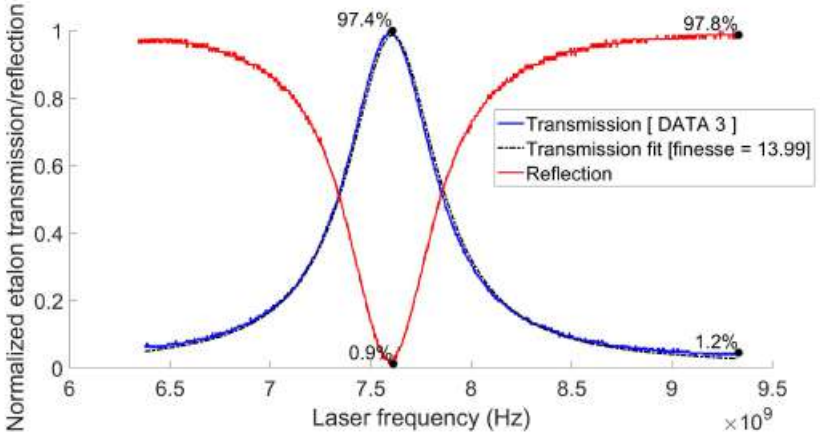


Figure 8.11: Etalon transmission (blue curve) and reflection (red curve) vs. laser frequency [57].

8.12 and 8.13: to align the etalon, we installed a PBS in order to have only P-polarization inside the etalon and a QWP to have circular polarization. Infact, if the beam is reflected back by the etalon, it will go a second time through the QWP, becoming S-polarized.
Then, we have added two steering mirrors (red circle in Fig. 8.13) for the

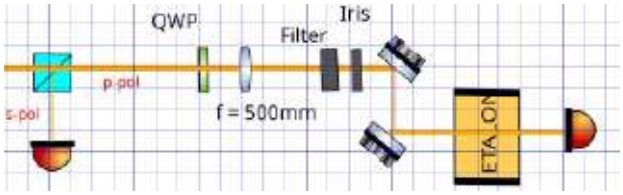


Figure 8.12: Optical design for etalon alignment performed in the R&D laboratory at EGO-Virgo site [62].

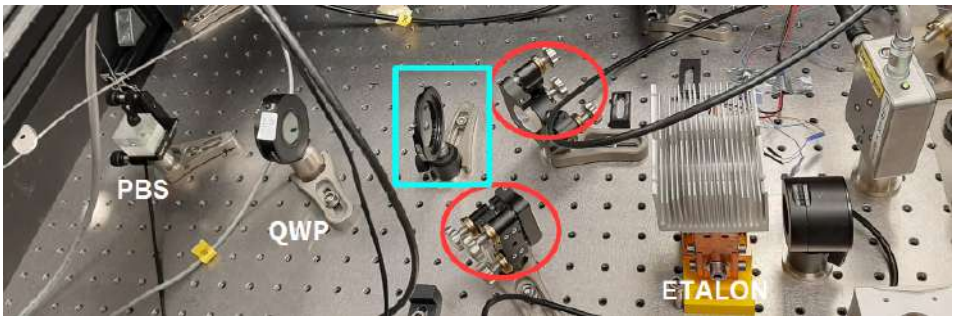


Figure 8.13: Optical setup for etalon alignment performed in the R&D laboratory at EGO-Virgo site [62].

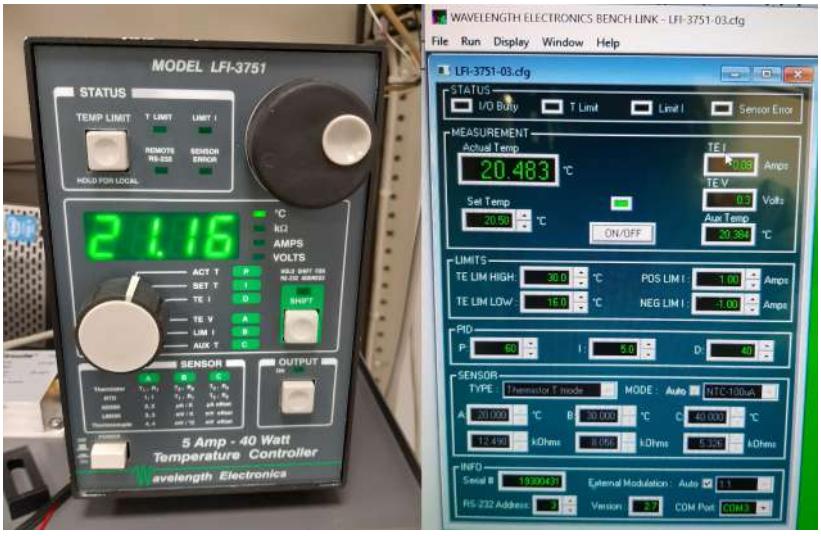


Figure 8.14: Etalon cavity is a system thermally controlled using a temperature controller (on the left) piloted by labview software (on the right) [57]. In the labview interface are shown the temperature setpoint and the PID (Proportional Integrative Derivative), i.e. the parameters for the control loop. Time is required to stabilize the temperature.

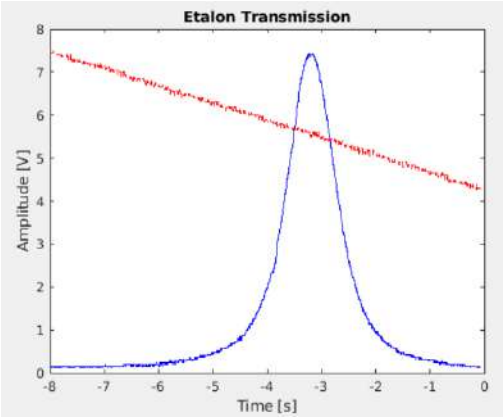


Figure 8.15: Fundamental mode content (blue curve) for the transmitted power of the etalon.

alignment of the beam inside the cavity, a focal lens (f=500 mm) due to the 3 mm aperture of the etalon coating, an iris diaphragm (blue square in Fig. 8.13) to better align, and a filter in order to not saturate PDs.
During the etalon alignment, we also used an IR viewer in order to look at the reflected beam on the iris diaphragm in order to superpose it to the incident beam.
In order to be exactly on the transmission peak, we need to scan the temperature (Peltier installed) and to modulate the AUX laser (a Mephisto laser with temperature laser crystal of 1K/V). Fig. 8.14 shows the box controller of the temperature by labview software.
Finally to check the alignment, we also measured the power before and after the etalon cavity with a power meter and, as shown in Fig. 8.15, we achieved more than 96% of fundamental mode content for the transmitted power (to be a little optimized).

### 8.2.3 MCIR cavity alignment

In this section, the MCIR cavity alignment on the $TEM_{00}$ mode will be presented, performed in Genoa laboratory. This MCIR will be used for the signal or idler beam, as shown in Fig. 8.2.

#### Low-noise current driver

In order to align the MCIR cavity, we mounted a new driver for the fiber optic laser diode DBR1064P (the same laser used in the chapter 5 but with a different driver).
Koheron CTL 101-1 (0-220mA, model b-200) is a low-noise current driver with modulation combined with a temperature controller for laser diodes in butterfly package (see Fig. 8.16). Once we connected well it to the diode

laser, we set the current 80 mA, which corresponds to 7 mW of power laser (from the characteristic P/I curve of our laser [43]).


Figure 8.16: The low-noise driver laser at Genoa laboratory (Koheron CTL 101).

Finally, to align the laser with respect to the MCIR cavity, we need 3 mA to modulate the laser, so we sent a ramp with 300 mV peak to peak. This values is due to the laser specific of the wavelength variation as a function of current $\frac{\Delta\lambda}{\Delta I} = 0.002nm/mA$, knowing the free spectral range of the MCIR (550 MHz) and remembering the resonance condition $2L = n\lambda$, with $L$ the length of the cavity.
The alternative method is to scan the MCIR applying a low-frequency ramp signal to the piezo-actuated mirror of the cavity.

### Actuators for MCIR alignment and results

A picture of the triangular MCIR cavity is shown in Fig. 8.17. The optical design for the MCIR alignment is shown in Fig. 8.18 and its beam path simulation in Fig. 8.19 from Gaussian Beam software.
In Fig. 8.20 a picture of the optical setup perfomed in Genoa laboratory is shown: we have a collimator in the laser output, the EOM to phase-modulate the laser in order to lock the MCIR cavity (Pound-Drever-Hall technique), a telescope to have the right waist inside the MCIR cavity and four mirrors for the beam alignment into the cavity.
In particular, we installed two actuators (M1 and M3 in Fig. 8.18) driven by KIM101 controllers (Thorlabs K-Cube Piezo Inertia Motor Controller) for remote alignment using a python script, and two other actuators (M2 and M4 in Fig. 8.18) driven by KPZ101 controllers (Thorlabs K-Cube Piezo Controller) for automatic-alignment loop with dither line technique.

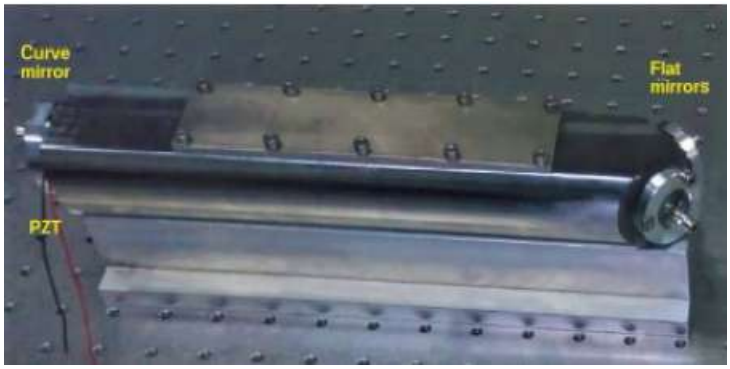


Figure 8.17: MCIR cavity at Genoa laboratory for the EPR experiment [43].

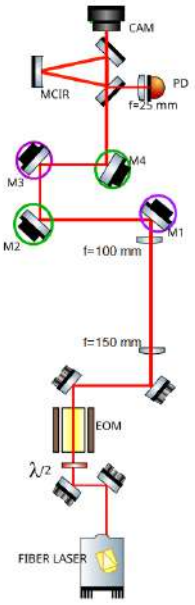


Figure 8.18: Optical design for MCIR AA alignment in Genoa laboratory.

| Optics | Position (mm) | Relative position (mm) | Properties | Waist (µm) | Waist position (mm) | Rayleigh range (mm) | Divergence (mrad) | Sensitivity (%/mm²) | Name | Lock |
|---|---|---|---|---|---|---|---|---|---|---|
| Input beam | 10 | | n = 1, M² = 1 | 600 | 10 | 1062.94 | 0.564469 | 2.21323e-05 | w0 | absolute |
| Lens | 110 | 100 | f = 150 mm | 84.5769 | 259.006 | 21.1209 | 4.0044 | 0.0582818 | L1 | none |
| Lens | 380 | 270 | f = 100 mm | 284.011 | 716.728 | 238.165 | 1.1925 | 0.0565432 | L2 | none |
| Flat mirror | 402.5 | 22.5 | | 284.011 | 716.728 | 238.165 | 1.1925 | 0 | M1 | none |
| Flat mirror | 430 | 27.5 | | 284.011 | 716.728 | 238.165 | 1.1925 | 0 | M2 | none |
| Flat mirror | 457.5 | 27.5 | | 284.011 | 716.728 | 238.165 | 1.1925 | 0 | M3 | none |
| Flat mirror | 480 | 22.5 | | 284.011 | 716.728 | 238.165 | 1.1925 | 0 | M4 | none |
| Flat mirror | 505 | 25 | | 284.011 | 716.728 | 238.165 | 1.1925 | 0 | MCIR | none |


Figure 8.19: Data editor and graphical interface from Gaussian Beam software of the simulation of the optical path for MCIR alignment (from the telescope to the MCIR cavity).

Fig. 8.21 shows the mirrors for the MCIR alignment.

Remembering that mode-matching (M.M.) is calculated as the percentage ratio between the amplitude of the first-order mode resonance ($V_{00}$) and the sum of the amplitude of all the higher-order modes, within a FSR, as follows:

$$M.M. = \frac{V_{00}}{\sum_{ij} V_{ij}} * 100 \tag{8.1}$$

we achieved M.M.TEM00$\sim$ 90% using python script by M1 and M3 actuators, as shown in Fig. 8.22.

We have to optimize this alignment with an automatic-alignment loop with dither line technique (the development is in progress). In fact, the two actuators driven by KPZ101 do not suffer from hysteresis, unlike actuators driven by KIM101, therefore it is possible to develop an AA loop analogous to those described in chapter 7.

The frequency response test of the AA actuators is shown in Fig. 8.23.

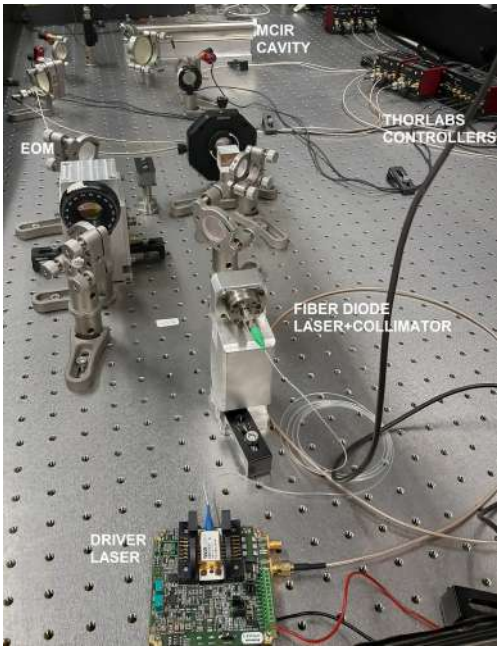


Figure 8.20: Optical setup for MCIR AA alignment in Genoa laboratory.

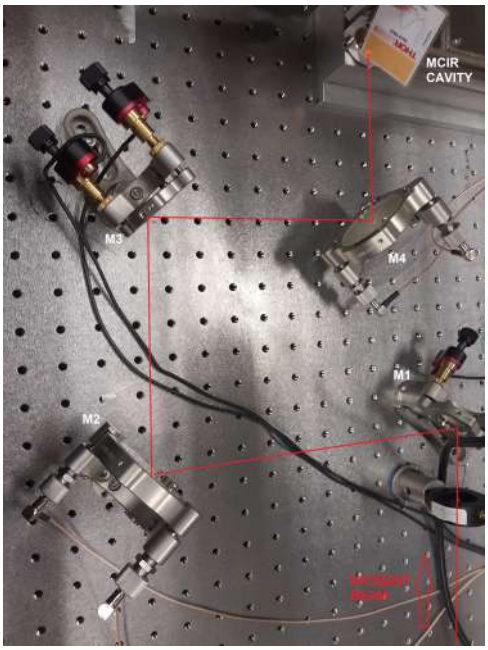


Figure 8.21: Mirrors for MCIR AA alignment.

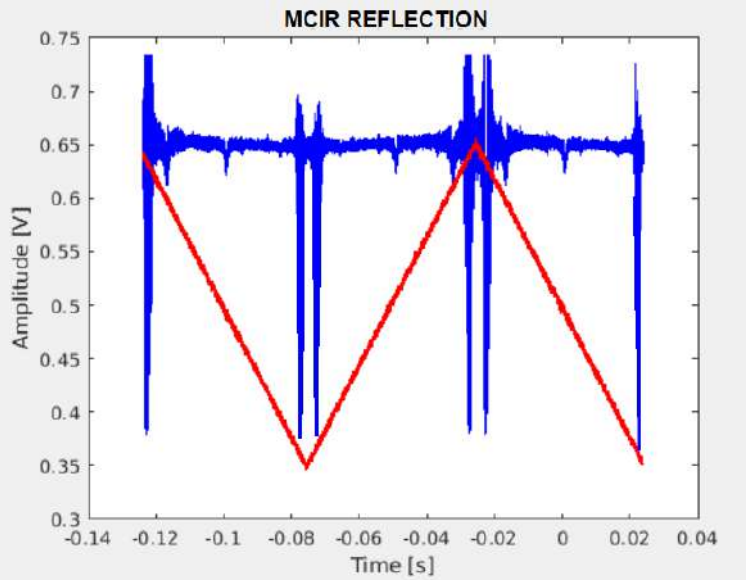


Figure 8.22: Mode-matching improvement with actuators driven by KIM101 using python script: we achieved about 90 %. The blue curve is the MCIR reflection, the red is the ramp sent to modulate the laser.

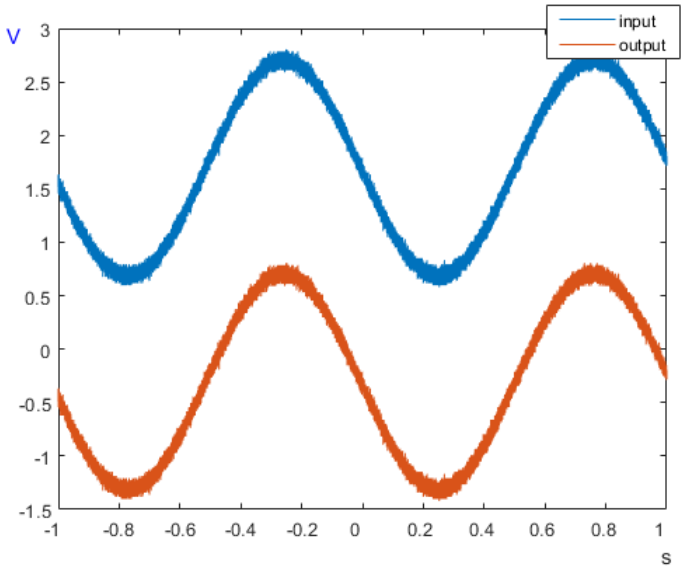


Figure 8.23: Frequency response of AA actuators driven by KPZ101. Blue curve is the sine sent to AA driver, red curve is the output of the KPZ101 controller.

# Chapter 9

# Results: squeezing measurements in AdV+

In this chapter, the results obtained thanks also to the activities illustrated in the chapters 4-5-6-7 are presented.
In particular, FIS and FDS measurements on the external homodyne detec-

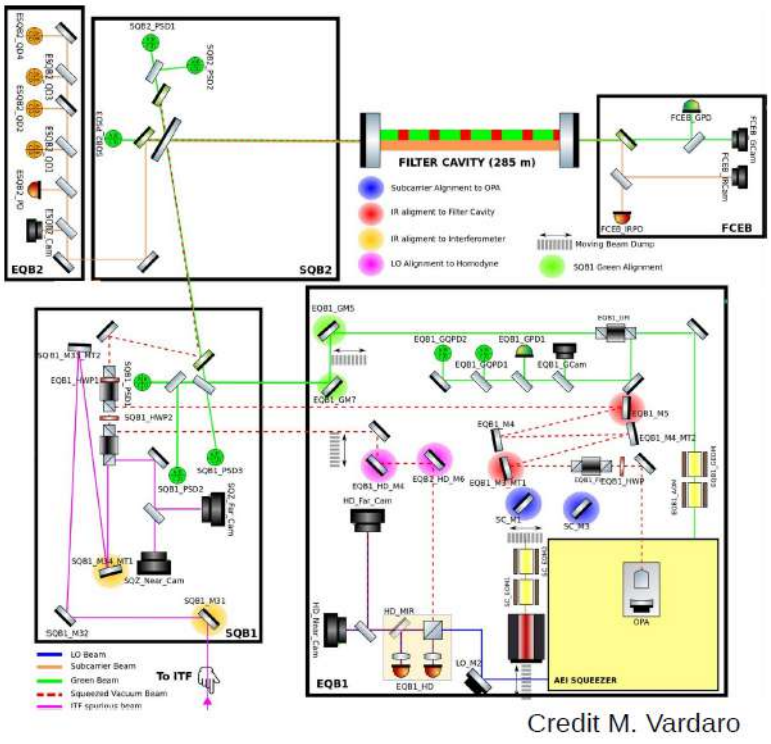


Figure 9.1: Conceptual design of Advanced Virgo Plus squeezing system [32].

tor with the optimized losses and phase noise will be explained, in order to

understand the contribution due to each part of the AdV+ squeezing system (Fig. 9.1) [63].

## 9.1 FIS measurement on EQB1 bench

We characterized the frequency-independent squeezing only on EQB1 bench, so with the beam folded by the delay line. In this way, we followed the procedure below to estimate the losses and the phase noise only on EQB1 bench:

- we measured the sensing noise of the CC loop, comparing the spectrum of signal without (only LO on homodyne detector) and with (LO, CC+SQZ beams on homodyne detector) the CC loop closed and we observed that above 50 Hz the CC loop is not limited by the sensing noise;
- we measured a homodyne Common Mode Rejection Ratio (CMRR) $>$ 60 dB, which did not limit our measurement. This measurement is important in order to understand how balanced our detector is;
- then, we scanned the green pump power (Mach-Zehnder offset), we took a shot-noise spectrum and the results are shown in the Fig. 9.2. In particular, we measured 7.5 dB of SQZ and 10.9 dB of ASQZ with 11.5 dB of generated SQZ;

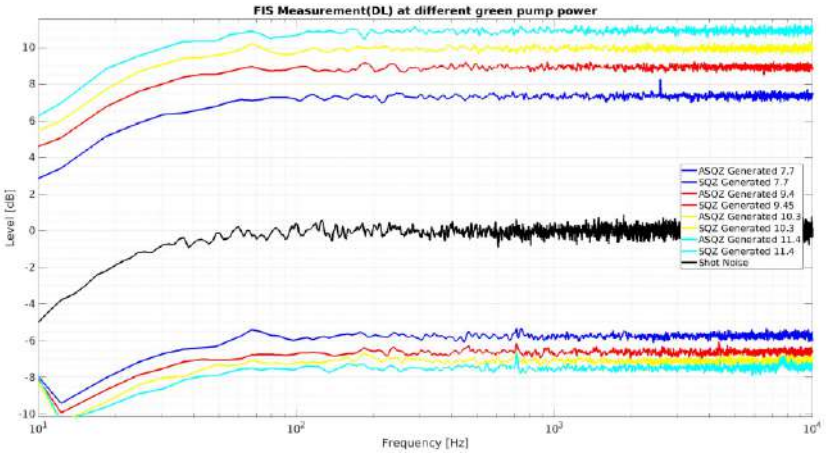


Figure 9.2: Frequency-independent squeezing measurement with delay line (only on EQB1 bench) at different green pump power. Results: 7.5 dB of squeezing measured, 10.9 dB of anti-squeezing, with 11.5 dB of generated squeezing (light-blue curve); the black curve is the shot-noise [64].

- moreover, we fitted the data obtaining 11.0 $\pm$ 0.4 % of losses with 14.8 $\pm$ 12.1 mrad of phase noise (see Fig. 9.3). Note that the spectra of the

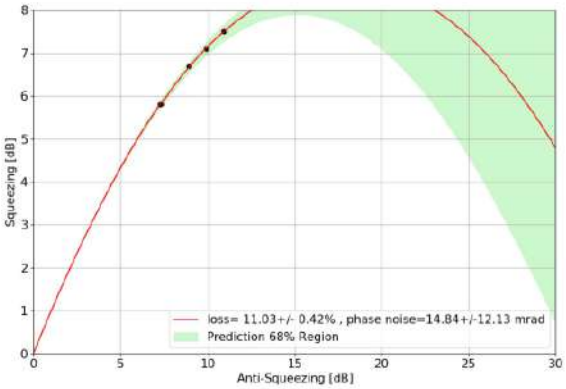


Figure 9.3: Pump power scan: estimate losses and phase noise from squeezing and anti-squeezing level with delay line (only on EQB1 bench). Results: 11.0 ± 0.4% of losses and 14.8 ± 12.1 mrad of phase noise [64].

measurement are flat, in fact we managed to insulate better the OPA from scattered light, rotating the HWP to improve the isolation factor of the EQB1 single in-air low losses Faraday Isolator.

## 9.2 FIS measurement up to SQB1 bench

We characterized the frequency-independent squeezing rising the SQB1 retroreflector. Before to show the losses and phase noise results, is important to briefly explain the procedure to check the Infrared (IR) alignment from EQB1 to SQB1 benches towards the homodyne detector, as follows:

- we checked the SC alignment into the OPA, closing the Sub-carrier (SC) AA loop;
- we aligned the filter cavity with the SC and then we compared the maximum of the Homodyne Detector (HD) magnitude between Delay Line (DL) and Filter Cavity Input Mirror (FCIM), estimating about 3% of propagation losses after DL;
- system well aligned. Note that we used an automatic-alignment loop to align the infrared beam on the filter cavity, shown in section 3.1.1.

So, we raised the SQB1 retroreflector and we aligned it with SC looking at the homodyne cameras (Near-Field and Far-Field cameras) and then maximizing the HD magnitude (switching off the SC): in order to do this, we moved the HWP of the double in-vacuum low losses Faraday Isolator to maximize the FI isolation factor. After that, we scanned the green pump power: in Fig. 9.4 are shown the spectra of the measurements, which are flat above 30 Hz,

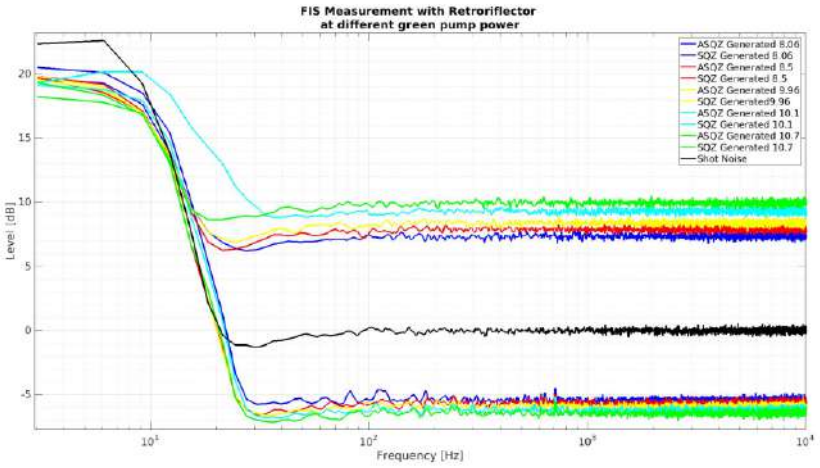


Figure 9.4: Frequency-independent-squeezing measurement with retroreflector (up to SQB1 bench) at different green pump power: the spectra of the measurements are flat above 30 Hz; the black curve is the shot-noise. Results: 6.5 dB of Squeezing (SQZ) and 10.0 dB of Anti-Squeezing (ASQZ) with 10.7 dB of generated SQZ [64].

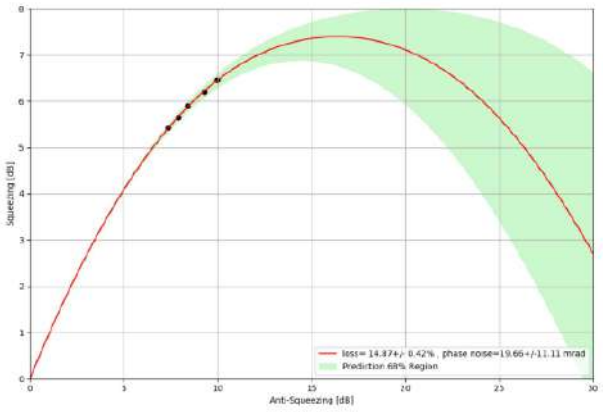


Figure 9.5: Pump power scan: estimate losses and phase noise from squeezing and anti-squeezing levels with retroreflector (up to SQB1 bench). Results: 14.9 $\pm$ 0.4% of losses, 20 $\pm$ 11 mrad of phase noise [64].

and we measured 6.5 dB of SQZ and 10.0 dB of ASQZ with 10.7 dB of generated SQZ. Fig. 9.5 shows the result of the fit of the SQZ and ASQZ levels: thus, we measured 14.9 $\pm$ 0.4 % of losses and 20 $\pm$ 11 mrad of phase noise.
The level of phase noise is compatible with the one measured with the DL line, whereas for the losses we measured 4% more. This level of propagation losses measured on HD is compatible with the power losses measured on the PD in front of the HD. These are two methods to measure propagation losses, but the HD magnitude is not a good way to measure them because it depends also from visibility and from polarization.

## 9.3 FDS measurement at 30Hz of filter cavity detuning

Frequency-dependent squeezing characterization at low frequency (25-30 Hz of filter cavity detuning) is shown. The frequency band in which the squeezing ellipse must be rotated is approximately centered around the point where the shot-noise and radiation-pressure noise power density are equal and for Advanced Virgo Plus (AdV+) this happens in the 20-30 Hz range.
After all the optimization performed in the previous sections, we scanned the green pump power with FDS configuration (see Fig. 9.6) and then we fitted the data (see Fig. 9.7) in order to measure the level of phase noise and losses. The fit did not work for the phase noise, but we obtained reasonable values as follows: 16.7 $\pm$ 1.5 % of losses and 30.1 $\pm$ 21.2 mrad of phase noise. In the spectra shows in Fig. 9.6, from ASQZ we never go below shot-noise, so something in the filter cavity alignment went wrong, but the measurement at high frequency is trustable.
Finally, we measured 6.5 dB of SQZ and 11.2 dB of ASQZ with 11.8 dB of generated SQZ.

Moreover, we characterized the FDS system at 30 Hz of filter cavity detuning with different homodyne relative angles, as shown in Fig. 9.8.
In conclusion, squeezing losses and phase noise were characterized in all the configurations, and we achieved the first long run with FDS configuration (about 40 hours). Note that these measurements were performed on the external homodyne detector on EQB1 bench. The next step will be the injection into the ITF, starting from the SC alignment into the Output-Mode-Cleaner (OMC), which is in progress.

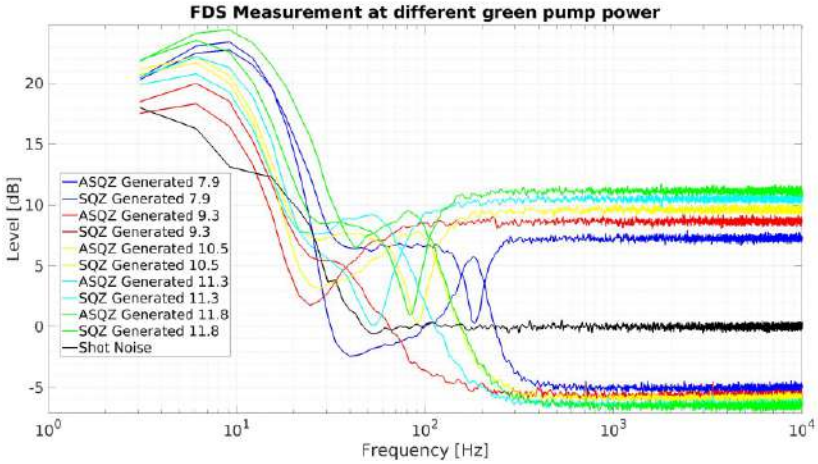


Figure 9.6: Frequency-dependent-squeezing measurement at different green pump power. Note that filter cavity was misaligned, so we never go below shot-noise from ASQZ. Results: 6.5 dB of SQZ and 11.2 dB of ASQZ with 11.8 dB of generated SQZ [64].

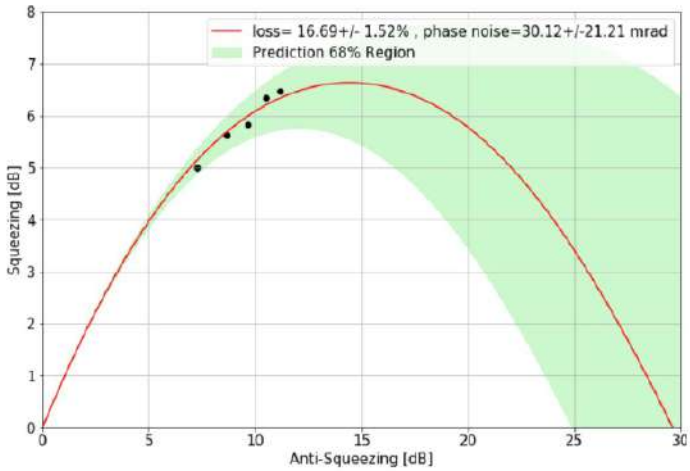


Figure 9.7: Pump power scan with FDS: estimate losses and phase noise from squeezing and anti-squeezing level. Results: $16.7 \pm 1.5$ % of losses and $30.1 \pm 21.2$ mrad of phase noise [64].

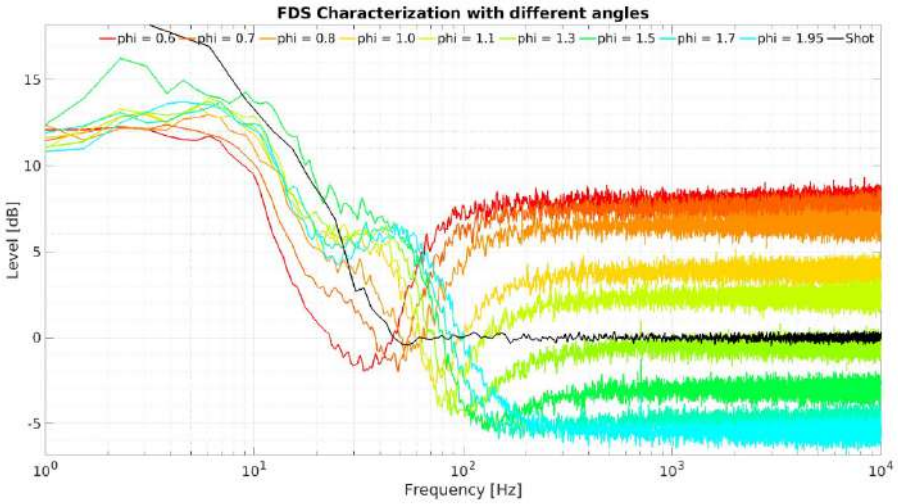


Figure 9.8: Frequency-dependent-squeezing measurement at 30 Hz of filter cavity detuning and characterization from homodyne angle from 0.6 rad to 1.95 rad [64].

# Chapter 10

# Conclusions

LIGO, VIRGO and KAGRA interferometers planned to start the next observative run (O4) in May 2023. The projected sensitivity of the Gravitational Wave (GW) detectors is shown in Fig. 10.1. In particular for O4 run, LIGO projects a sensitivity goal of 160-190 Mpc for Binary Neutron Stars (BNS), Virgo a target of 80-115 Mpc and KAGRA should be running with greater than 1 Mpc sensitivity at the beginning of O4, and will work to improve the sensitivity towards the end of O4 run.

For now, Virgo has achieved a stable operation of the interferometer and about the squeezing system, it has produced a maximum of 12 dB of squeezing, assuring 4 dB of quantum noise reduction in the GW interferometer (see Fig. 10.3 for the simulation of quantum noise curve with and without FDS injection). The next step is to inject FDS in the ITF. In Fig. 10.2 is shown the simulation of AdV+ Phase I sensitivity improved in all the interferometer frequency-band by injection of 7 dB of frequency-dependent Squeezing. In fact, Advanced Virgo Plus has two phases for its realization:

Phase I the main goal is to reduce the interferometer sensing noise, which lim-

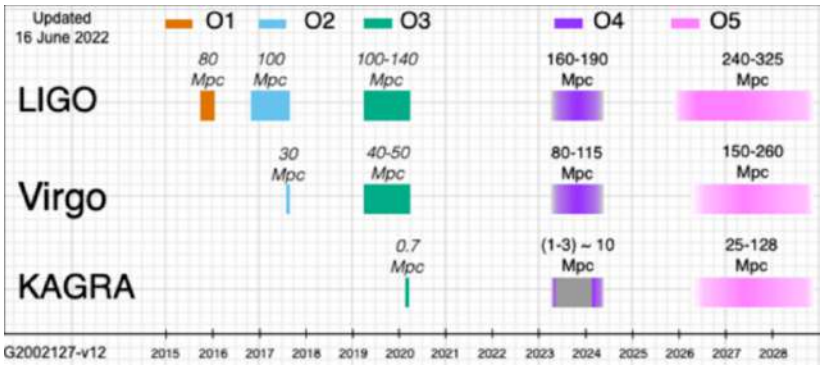


Figure 10.1: Projected timeline of observing runs and expected binary neutron star (BNS) detection range for LIGO, Virgo, and KAGRA detectors.

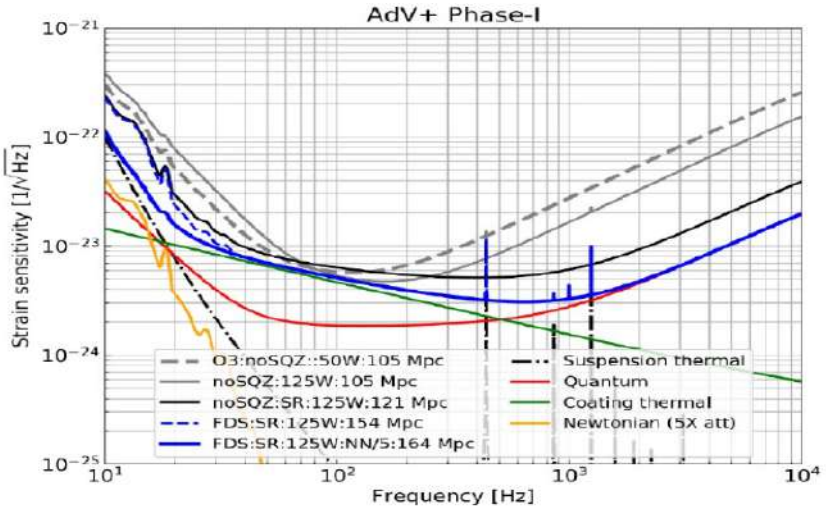


Figure 10.2: The improvement of the sensitivity curve of AdV+ Phase I by injection of 7 dB of Frequency-Dependent-Squeezing.

itation coming from quantum noise, by implementing the signal recycling technique, increasing the laser power injected into the interferometer by a factor of two and by injection of FDS achieved by a 300m long detuned cavity (between O3 and O4 runs);

Phase II the main goal is the reduction of the mirror thermal noise, by enlarging the beam on the end mirrors. The change in the beam will require larger mirrors for the end mirrors, to change also the two cavity input mirrors, the power recycling mirror and the signal recycling mirror (between O4 and O5 runs).

With the combination of the two phases improvements, the BNS range of AdV+ will be above 200 Mpc.

Also LIGO's two detectors in Washington State and Louisiana installed a filter cavity to perform a FDS injection. KAGRA should start with Virgo and LIGO, then move away for commissioning and return to observation with increased sensitivity towards the end of the O4 run.

Concerning the alternative technique based on EPR entangled beams, our experiment is in progress and the final goal is to inject, for the first time, these beams in a system sensitive to quantum noise in the whole detection bandwidth at the same frequencies of GW detectors. In the future, it could be implemented for the next generation of gravitational wave interferometers.

In conclusion, my PhD is mainly based on experimental activities for the development of advanced quantum optics techniques, both for the squeezing system working in AdV+ and for the EPR experiment.

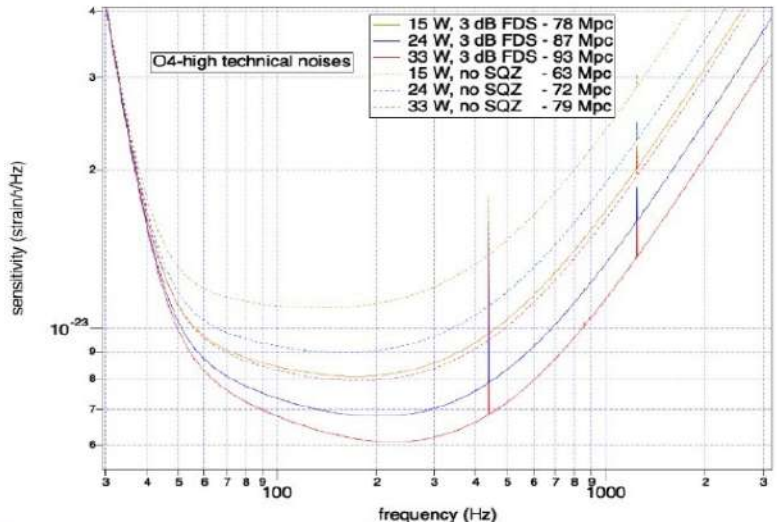


Figure 10.3: Simulation of Quantum noise curves of Advanced Virgo Plus with and without FDS injection (Credits: G.Gemme).

In particular, I actively contributed to the quantum noise reduction team during the commissioning for the next Virgo O4 observing run, dealing both with the optical part of the squeezing system and with the development of angular controls.
For the EPR experiment, my contribution was mainly on the development of the optical design, later on the optical setup, testing of acousto-optic modulators and optical cavities.
Moreover, my activities related to the two quantum noise reduction experiments allowed me to publish papers in conference journals.

# List of Figures

# Ringraziamenti

A conclusione della mia Tesi di Dottorato, desidero ringraziare coloro che hanno contribuito alla sua realizzazione e che mi hanno accompagnata in questi tre anni.
Innanzitutto, un grazie speciale al mio gruppo di ricerca di Genova capitanato dai professori Gianluca Gemme, Andrea Chincarini e Fiodor Sorrentino che mi hanno da subito accolta come in una famiglia e mi hanno ascoltata permettendomi di specializzarmi in ciò che più mi piace, e un grazie ai ragazzi della mitica L307 per tutti i consigli e i ricordi che custodirò. Non potevo desiderare gruppo di lavoro migliore. Nello specifico, vorrei ringraziare il mio relatore Fiodor Sorrentino per la grande fiducia riposta in me, per avermi sempre spronata a lavorare in gruppi interdisciplinari, per avermi dato la possibilità di arricchire il mio bagaglio di esperienze che mi hanno permesso di crescere, sia a livello lavorativo sia a livello personale. Mi sento molto grata di tutto ciò che mi ha permesso di imparare.
Ci tengo a ringraziare tutti i colleghi di Virgo coi quali ho collaborato e dai quali ho potuto assorbire immensa conoscenza. Non posso citarvi tutti, ma desidero ringraziare in modo particolare Marco per la pazienza, gli insegnamenti e il grande supporto datomi, Martina, una persona eccezionale sia dal punto di vista scientifico sia personale, Sibilla, per la sua disponibilità e comprensione, Jean-Pierre, il boss dello Squeezing e la mia carissima Valeria, colei che mi ha introdotta nei meandri dell'Ottica, oltre essere una preziosa amica. Grazie a tutto il gruppo di Squeezing di Virgo, e non solo, per avermi accolta e avermi dato la possibilità di collaborare con voi: per me è stato un vero onore.
Un grazie anche alle amiche che mi hanno sostenuta e incoraggiata.
Infine, il più grande ringraziamento va alla mia famiglia, ai miei genitori e a mia sorella che hanno sempre creduto in me, supportandomi e permettendomi di alimentare la mia curiosità e perseguire le mie passioni. Non sarei arrivata fin qui se non fosse stato per voi. Un grazie speciale anche a Matteo, per esserci sempre stato.
Grazie infinite a tutti voi.

# List of acronyms

**A**

**AdV+** Advanced Virgo Plus

**AOM** Acousto-Optic-Modulator

**AA** Automatic-Alignment

**ASQZ** Anti-Squeezing

**B**

**BAB** Bright Alignment Beam

**BBH** Binary Black Holes

**BNS** Binary Neutron Stars

**BS** Beam Splitter

**C**

**CMRR** Common-Mode Rejection Ratio

**D**

**DL** Delay Line

**DoF** Degree of Freedom

**E**

**EOM** Electro-Optic Modulator

**EPR** Einstein-Podolsky-Rosen

**ET** Einstein Telescope

**F**

**FCIM** Filter Cavity Input Mirror

**FDS** Frequency-Dependent-Squeezing

**FI** Faraday Isolator

**FIS** Frequency-Independent-Squeezing

**FSR** Free Spectral Range

**G**

**GR** General Relativity

**GW** Gravitational Wave

**H**

**HD** Homodyne Detector

**HWP** Half-Wave-Plate

**I**

**IR** Infrared

**ITF** Interferometer

**L**

**LO** Local Oscillator

**M**

**MC** Mode Cleaner

**MCG** Mode Cleaner Green

**MCIR** Mode Cleaner Infrared

**MZ** Mach-Zehnder

**O**

**OMC** Output-Mode-Cleaner

**OPO** Optical Parametric Oscillation

**OPA** Optical Parametric Amplification

**OPLL** Optical Phase-Locked Loop

**P**

**PBS** Polarizing Beam Splitter

**PD** Photodiode

**PDH** Pound-Drever Hall

**PID** Proportional Integrative Derivative

**PLL** Phase-Locked-Loop

**PRM** Power Recycling Mirror

**PSD** Power Spectral Density

**PZT** Piezoelectric

**Q**

**QN** Quantum Noise

**QPS** Quadrant photodetector

**QWP** Quarter-Wave Plate

**R**

**RoC** Radius of Curvature

**RPN** Radiation Pressure Noise

**RTL** Round-Trip Losses

**S**

**SQZ** Squeezing

**SHG** Second-Harmonic Generation

**SC** Sub-carrier

**SIPS** Suspended Interferometer for Pondemorotive Squeezing

**SN** Shot-Noise

**SQL** Standard Quantum Limit

**SRC** Signal Recycling Cavity

**SRM** Signal Recycling Mirror

**T**

**TEC** Thermoelectric Cooler

**TM** Test Mass

# Bibliography


[1] The LIGO Scientific Collaboration and the Virgo Collaboration. GW150914: First results from the search for binary black hole coalescence with Advanced LIGO. 10.1103/PhysRevD.93.122003. 2016.

[2] B. P. Abbott et al. (LIGO Scientific Collaboration and Virgo Collaboration). Gw170817: Observation of gravitational waves from a binary neutron star inspiral. *Physical Review Letters 10.1103/PhysRevLett.119.161101*, 2017.

[3] The LIGO Scientific Collaboration and the Virgo Scientific Collaboration. Multi-messenger observations of a binary neutron star merger. 10.3847/2041-8213/aa91c9, 2017.

[4] F. Acernese et al. Advanced Virgo: a second-generation interferometric gravitational wave detector. Classical and Quantum Gravity 10.1088/0264-9381/32/2/024001, 2014.

[5] F. Acernese et al. Increasing the Astrophysical Reach of the Advanced Virgo Detector via the Application of Squeezed Vacuum States of Light. Physical Review Letters 123.23, 2019.

[6] B. P. Abbott et al. (LIGO Scientific Collaboration and Virgo Collaboration). Observation of gravitational waves from two neutron star–black hole coalescences. *The Astrophysical Journal Letters 10.1103/PhysRevLett.119.161101*, 2021.

[7] M. Maggiore. Gravitational waves: Volume 1: Theory and experiments. *Oxford University Press*, 2007.

[8] F. Bergamin. Stabilization of the squeezed vacuum source for the virgo interferometer. master thesis, 2017/2018.

[9] V. Sequino. Development of a squeezed lightsource for the gravitational wavedetector advanced virgo. *PhD thesis*, 2015/2016.

[10] R. A. Hulse and J. H. Taylor. Discovery of a pulsar in a binary system. 10.1086/181708, 1975.

[11] The LIGO Scientific Collaboration. A gravitational wave observatory operating beyond the quantum shot-noise limit. 10.1038/nphys2083, 2011.

[12] The LIGO Scientific Collaboration. Advanced ligo. 10.1088/0264-9381/32/7/074001, 2015.

[13] K. Somiya. Detector configuration of kagra - the japanese cryogenic gravitational-wave detector. 10.1088/0264-9381/29/12/124007. 2011.

[14] A. Perot and C. Fabry. On the application of interference phenomena to the solution of various problems of spectroscopy and metrology, 1899.

[15] F. Acernese et al. Quantum Backaction on kg-Scale Mirrors: Observation of Radiation Pressure Noise in the Advanced Virgo Detector. Physical Review Letters 10.1103/PhysRevLett.125.131101, 2020.

[16] Gregory M. Harry et al. Thermal noise from optical coatings in gravitational wave detectors. 10.1364/ao.45.001569, 2006.

[17] M. Granata et al. Progress in the measurement and reduction of thermal noise in optical coatings for gravitational-wave detectors. 10.1364/oic.2019.fa.1, 2019.

[18] M. Fox. Quantum optics: An introduction. *Physics Today 10.1063/1.2784691*, 2006.

[19] C.M. Caves. Quantum-mechanical noise in an interferometer. *Physical Review D 10.1103/PhysRevD.23.1693*, 1981.

[20] C.C. Gerry and P.L. Knight. Introductory Quantum Optics. Cambridge University Press 10.1017/CBO9780511791239, 2005.

[21] R. Schnabel. Squeezed states of light and their applications in laser interferometers. 10.1016/j.physrep.2017.04.001. 2016.

[22] Carlton M. Caves, Bonny L. Schumaker. New formalism for two photon quantum optics. I. Quadrature phases, and squeezed states. Physical Review 10.1103/PhysRevA.31.3068, 1985.

[23] Hans-A. Bachor and Timothy C. Ralph. A guide to experiments in quantum optics, 2004.

[24] R.W. Boyd. Nonlinear optics, third edition. *Academic Press 978-0-12-369470-6*, 2008.

[25] Tobias Westphal Joran Bauchrowitz and Roman Schnabel. A graphical description of optical parametric generation of squeezed states of light. 10.1119/1.4819195, 2013.

[26] Yue-Meng Chi et al. A balanced homodyne detector for high-rate gaussian modulated coherent-state quantum key distribution. 10.1088/1367-2630/13/1/013003, 2011.

[27] MS Stefszky et al. Balanced homodyne detection of optical quantum states at audio-band frequencies and below, 2012.

[28] P. Kwee et al. Decoherence and degradation of squeezed states in quantum filter cavities. 10.1103/ physrevd.90.062006, 2014.

[29] M Mehmet and H Vahlbruch. High-efficiency squeezed light generation for gravitational wave detectors. 10.1088/1361-6382/aaf448, 2018.

[30] J. Gniesmer. Advanced Techniques for Squeezed-Light-Enhanced Gravitational-Wave Detection. PhD thesis 978-0-12-369470-6, 2019.

[31] L. McCuller et al. Frequency-Dependent Squeezing for Advanced LIGO. Phys. Rev. Lett. 10.1103/PhysRevLett. 124.171102, 2020.

[32] F. Sorrentino. FDS Global control status. Presentation VIR-0376A-20 M. Vardaro, 2020.

[33] The Virgo Collaboration. Advanced Virgo Plus Phase I Design Report. Technical Design Report VIR-0596A-19, 2019.

[34] E. D. Black. An introduction to pound–drever–hall laser frequency stabilization. *American Journal of Physics 10.1119/1.1286663*, 2001.

[35] E. Capocasa on behalf of Virgo QNR team. Frequency dependent squeezing for AdVirgo+. Presentation VIR-0436A-22, 2022.

[36] Daniel D. Brown et al. Broadband sensitivity enhancement of detuned dual-recycled michelson interferometers with epr entanglement. 10.1103/physrevd.96.062003, 2017.

[37] J.P. Zendri at al. Study M. Bawaj, B. Garaventa and experiment on the alternative technique of frequency-dependent squeezing generation with EPR entanglement for Virgo. Journal of Physics: Conference Series 10.1088/1742-6596/1468/1/012215, 2020.

[38] Y. Ma et al. Proposal for gravitational-wave detection beyond the standard quantum limit through epr entanglement. *Nature Physics 10.1038/NPHYS4118*, 2017.

[39] B. Garaventa and Virgo Collaboration. Quantum noise reduction in gravitational wave interferometers. publication submitted, 2023.

[40] N. Rosen A. Einstein, B. Podolsky. Can quantum-mechanical description of physical reality be considered complete? *Physical Review 10.1103/PhysRev.48.696*, 1935.

[41] Alain Aspect and Michel Brune. Quantum optics 2 - two photons and more.

[42] Gooch and Housego. Introduction to acousto-optic modulators and detectors. optoscience.

[43] B. Garaventa. Towards an Einstein-Podolsky-Rosen experiment for Quantum Noise reduction in Gravitational Wave detectors. Master's Thesis, 2019.

[44] D. J. Mccarron. A guide to acousto-optic modulators, 2007.

[45] E. A. Donley et al. Double-pass acousto-optic modulator system. *Review of Scientific Instruments 10.1063/1.1930095*, 2005.

[46] H. Vahlbruch et al. Coherent control of vacuum squeezing in the gravitational-wave detection band. 10.1103/physrevlett.97.011101. 2018.

[47] D. Bersanetti. Readout Sensing and Control. ISC Training Session VIR-0103A-18, 2018.

[48] AdV+ squeezing team. CC demodulation. Internal Virgo report, 2021.

[49] S. Chelkowski. Squeezed Light and Laser Interferometric Gravitational Wave Detectors. PhD Thesis, 2007.

[50] E. Polini. Broadband quantum noise reduction in AdV+ : From frequency-dependent squeezing implementation to detection losses and scattered light mitigation. PhD thesis VIR-1201A-22, 2022.

[51] E. Schreiber et al. Alignment sensing and control for squeezed vacuum states of light. 10.1364/oe.24.000146. 2016.

[52] E. Morrison et al. Automatic alignment of optical interferometers. *Optical science of America 10.1364/AO.33.005041*, 1994.

[53] D. Anderson. Alignment of resonant optical cavities. 10.1364/ao.23.002944, 1984.

[54] B. Garaventa. Automatic alignment technique for the squeezing system in Advanced Virgo Plus. ICNFP 2022 presentation VIR-0847A-22, 2022.

[55] Jan Südbeck et al. Demonstration of interferometer enhancement through einstein–podolsky–rosen entanglement. 10.1038/s41566-019-0583-3, 2020.

[56] B. Garaventa et al. Frequency-dependent squeezing generation with epr entanglement. Institute of Physics Publishing 10.1088/1742-6596/1548/1/012013, 2020.

[57] et al. B. Garaventa, C. Nguyen. Automated source of squeezed vacuum states driven by finite state machine based software. *Review of Scientific Instruments 10.1063/5.0046317*, 2021.

[58] M. Vardaro. Toward a fully automated and digitally controlled squeezed vacuum source for gravitational wave detectors. PhD Thesis, 2018.

[59] M. Maggiore et al. Science case for the einstein telescope. 10.1088/1475-7516/2020/03/050, 2020.

[60] M. De Laurentis S. Di Pace, L. Naticchioni and F. Travasso. Thermal noise study of a radiation pressure noise limited optical cavity with fused silica mirror suspensions. *European Physical Journal D 10.1140/epjd/e2020-10183-7*, 2020.

[61] C. Nguyen. Development of squeezing techniques for quantum noise reduction in gravitational-wave detectors. PhD Thesis VIR-0254A-22, 2021.

[62] C. Nguyen B. Garaventa and E. Bréelle. Etalon alignment procedure for the EPR experiment at 1500W laboratory. Internal presentation for the EPR weekly meeting VIR-0836A-22, 2022.

[63] M. Mehmet H. Lück The Virgo Collaboration, H. Vahlbruch and K. Danzmann. Frequency dependent squeezed vacuum source for the advanced virgo gravitational wave detector vir-1208c-22, 2023.

[64] M. Vardaro on behalf of Virgo QNR team. Update on QNR system. Presentation VIR-0975A-22, 2022.